SPECS 2022

University of Hertfordshire UH

PROCEEDINGS OF ABSTRACTS

SCHOOL OF PHYSICS, ENGINEERING AND COMPUTER SCIENCE RESEARCH CONFERENCE 2022

Tuesday 12th April 2022 - Online

University of Hertfordshire, Hatfield, UK

Editor: Loïc Coudron

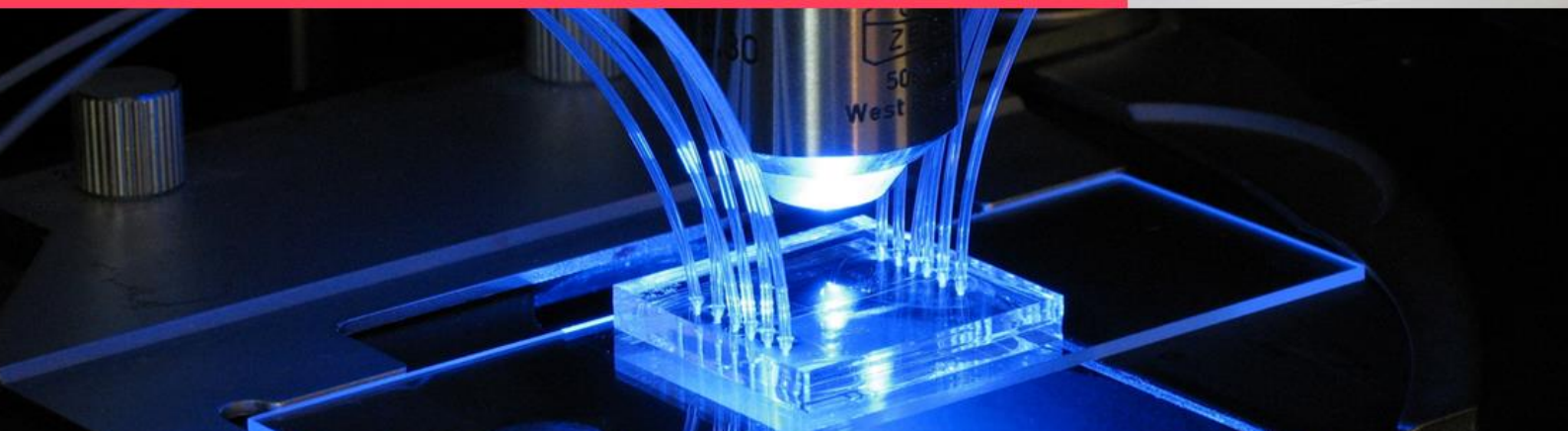

Proceedings of Abstracts Physics, Engineering and Computer Science Research Conference, 12th April 2022, University of Hertfordshire, Online

Editor Loïc Coudron

Published online: UH Research Archive, 4th November 2022

Published by
University of Hertfordshire
College Lane
Hatfield
AL10 9AB
United Kingdom

DOI: 10.18745/pb.25867

URL: https://doi.org/10.18745/pb.25867

Contact

Dr Loic Coudron
Centre for Biodetection Technologies,
Centre for Engineering Research,
Microfluidics and Microengineering Research Group
School of Physics, Engineering and Computer Science
University of Hertfordshire
College Lane, Hatfield, Herts, AL10 9AB, UK
Email: l.coudron@herts.ac.uk
Tel: +44 (0)1707 286174

Copyright and Open Access

University of Hertfordshire UH

Preface

Dear Readers of these proceedings,

Here is the record of abstracts submitted and accepted for presentation at SPECS 2022, the second edition of the School of Physics, Engineering and Computer Science Research Conference that took place online, the 12th April 2022

After an event cancelled in 2020 and another gap year in 2021, SPECS 2022 followed up on the success of the Inaugural ECS Research Conference in 2019. As a local event organised by the School of Physics, Engineering and Computer Science the conference brought together the three departments of the School to showcase the broad multidisciplinary range of topical research taking place. To represent this cross-disciplinarity, three cross-disciplinary sessions were presented: Engineering a Sustainable Future; Understand and Expand our boundaries; and Security, Protection, Care.

The conference was a great celebration of the University's SPECS research excellence and a formidable opportunity for the students, staff and eminent external guests to share expertise, present new scientific knowledge and discuss innovative ideas. It was also the first time that the research community across the three departments met in a joint research event, and it was delightful to notice the great appetite among colleagues for a strong, common and cohesive research culture.

It is expected that the third SPECS research conference will be taking place the in June 2023 to continue acknowledging, at the University of Hertfordshire, the research diversity, innovation and excellence in SPECS.

Organising and Scientific Committee

Emil Dmitruk	Mahmoud Eltaweel	Vahid Hosseini
Kumar S. Prasad	Prof. Phil Lucas	Dr Gabriel Barros dos Santos
Dr Peter Thomas	Prof. Pandelis Kourtessis	Dr Sikiru Ismail
Dr Opus David-West	Dr Gbanaibolou Jombo	Dr Christabel Tan
Dr Shabnam Kadir	Dr Amin Paykani	Dr Nada Youssif
Dr Myasar Tabany	Dr Loic Coudron	

University of Hertfordshire UH

Awards

Many congratulations to:

- **Our Best Oral Presentation Award** winner Simon McCool for this presentation *'Mitigating motorcycle accidents at yield junctions using computer vision and deep learning: a preliminary study'*
- **Our First Prize Best Poster Award** winner Marc Norgate for his poster *'Climate Extremes in Coupled Climate Models'*
- **Our Second Prize Best Poster Award** winner Samadhi Samararatne for his poster *'CFD Investigation of Aerofoil Design Effects on Dynamic Stall Characteristics'*
- **Our Third Prize Best Poster Award** winner Jaime Vargas-González for his poster *'Protostellar radio variability: A window to high-energy processes in young stars through the eyes of ALMA, VLA, and VLBA'*

Congratulations to all our delegates for their excellent contributions.

Acknowledgements

The members of the organising committee would like to thanks the eminent guests who accepted the invitation to share their insight and experience with our delegates:

Professor Jonathan Reid from the University of Bristol, School of Chemistry, Director of the EPSRC Centre for Doctoral Training in Aerosol Science, for his talk *'Aerosol Science: Revealing Complexity and Exploring Multi-Disciplinarity'*

Professor Timothy Foat from the Defence Science and Technology Laboratory, Principal Engineer, Biological and Radiological Division, who share valuable insight on *'Indoor dispersion at Dstl and its recent application to COVID-19 transmission'*

We wish to acknowledge, for their valuable support during the organisation of the event and their contribution to the programme:

Professor Quintin McKellar, Vice-Chancellor

Professor John Senior, Pro Vice-Chancellor Research and Enterprise

Professor Pandelis Kourtessis, Associate Dean Research and Enterprise, SPECS

We would like to thank all delegates for their excellent contributions to the conference. Special thanks to, Professor Kobayashi, Professor Chen and Dr Kadir for accepting the invitation and for the outstanding presentation highlighting the very topical research in SPECS. Special thanks also to Professor Lucas, Professor Kourtessis and Doctor Barros dos Santos for chairing the sessions and made the day flow seamlessly. Finally, we are grateful to the judging panel for attributing the conference award.

University of Hertfordshire UH

Table of Contents

University of Hertfordshire UH

Programme

Welcoming participants

9:00 – 9:10 **Dr Loic Coudron**, Organising Committee – *Introduction and online house keeping*

9:10 – 9:20 **Prof. Quintin McKellar**, Vice-Chancellor – *Welcoming speech*

Session 1. Security, Protection, Care – chaired by Dr Loic Coudron

9:20 – 9:35 **Dr Adrian Ghita, PAM,** *Non-invasive label-free detection of water molecular markers in large biological samples using Transmission Raman Spectroscopy*

9:35 – 9:50 **Simon McCool, CS,** *Mitigating motorcycle accidents at yield junctions using computer vision and deep learning: a preliminary study*

9:50 – 10:05 **Dr Gbanaibolou Jombo, Eng.,** *Evaluation of 2D Acoustic Signal Representations for Acoustic-Based Machine Condition Monitoring*

Session 2. Engineering a Sustainable Future – chaired by Dr Gabriel Barros dos Santos

10:05– 10:25 **Prof. Yong Chen (invited speaker), Eng.,** *The Prospects of Nano materials in energy storage systems*

10:25 – 10:40 **Elizabeth Mathen, PAM,** *Modelling and Analysis of ice crystals based on in-situ light scattering patterns*

10:40 – 10:55 **Colin Mallett, Trusted Renewables,** *Can 'Innovation Integration' and 'Digital Twins' Help Solve Energy Supply Problems?*

Lunch and Poster session

See list of posters next page – Download here

11:00 – 12:00 **Odd numbers** (P1, P3, P5, …, P27)

12:00 – 13:00 **Even numbers** (P2, P4, P6, …, P28)

Plenary Session - chaired by Prof. Pandelis Kourtessis

13:00 – 13:45 **Professor Jonathan Reid,** University of Bristol, School of Chemistry, Director of the EPSRC Centre for Doctoral Training in Aerosol Science. *Aerosol Science: Revealing Complexity and Exploring Multi-Disciplinarity*

13:45 – 14:30 **Professor Timothy Foat,** Defence Science and Technology Laboratory, Principal Engineer, Biological and Radiological Division**,** *Indoor dispersion at Dstl at its recent application to COVID-19 transmission*

Session 3. Understand and Expand our Boundaries – chaired by Prof. Philip Lucas

14:30– 14:50 **Prof. Chiaki Kobayashi (invited speaker)**, **PAM,** *The origin of elements and the evolution of galaxies*

14:50– 15:05 **Tracy Garatt, PAM,** *SCUBA-2 Large eXtragalactic Survey: Constraining the bright-end of the 850 μm number counts*

15:05– 15:20 **Muhammad Yaqoob, CS,** *Analysing Spiking Neural Networks Evolved for Temporal Pattern Recognition*

15:20 – 15:40 **Dr Shabnam Kadir (invited speaker), CS,** *Topology - a new lens into the brain*

Closing Remarks and Prizes

16:00 **Closing remarks and prizes – Prof Pandelis Kourtessis**

Open Forum from 15:40 onward

List of Posters

Download here

Booth 1 - P1	**Etelka Chung,** *Antimicrobial Evaluations of Metallic Nanoparticles*
Booth 1 – P2	**Minghua Zheng,** *Bacterial colony counting could be rapid, adaptive and automated*
Booth 2 – P3	**Samadhi Samararatne,** *CFD Investigation of Aerofoil Design Effects on Dynamic Stall Characteristics*
Booth 2 – P4	**Laurel Asimiea,** *Development of a Bespoke Hybrid Regression-based Technique for Diesel Engine Optimisation*
Booth 3 – P5	**David Haydock,** *Identifying Analogous State Types Across Simultaneously Recorded EEG-fMRI*
Booth 3 – P6	**Himayasri Lekkala,** *Developing microfluidic devices and techniques for isolation and detection of Extracellular Vesicles (EVs)*
Booth 4 – P7	**Josefine Gårn,** *Carbon-to-oxygen ratio as a clue to the formation of Ross 458c*
Booth 4 – P8	**Harpreet Singh,** *Using LSA to reduce Textual-based neural models' complexity*
Booth 5 – P9	**Sajid Fadlelseed,** *A Short-term Scheduler with Criticality Arithmetic*
Booth 5 – P10	**Paul Moggridge,** *Investigating Instance Weighted Spectral Clustering using Genetic Algorithms*
Booth 6 – P11	**Marc Norgate,** *Climate Extremes in Coupled Climate Models*
Booth 6 – P12	**Marina Arnaudova,** *Probing the radio-loud/radio-quiet dichotomy of SDSS quasars*
Booth 7 – P13	**Daerefa-a Amafabia,** *Analysis of Modal Parameters' Variations due to Increased Impact Energy Damage in CFRP Laminates*
Booth 7 – P14	**Adrian Felix,** *Identifying the optimum fuel cell current density range for a SOFC-GT hybrid power system*
Booth 8 – P15	**Qi Luo,** *Metal-only Planar Lens for Wireless Communications*
Booth 8 – P16	**Surya Maruthupandian,** *Systematic Evaluation of Mineral Wastes for Use in Cementitious Binders*
Booth 9 – P17	**Aklil Kiflay,** *A Machine Learning Pattern for CNNs with Mixed-Feature Modes*
Booth 9 – P18	**Patrick Irigo,** *Ultraviolet Irradiation Enhanced Nanoparticles to Fight Against Coronavirus Transmission*
Booth 10 – P19	**Kumar S. Prasad,** *Effects of Sensor Spacing and Material Thickness of Al 6082-T6 using Acousto-Ultrasonics Technique*
Booth 10 – P20	**Jaime Vargas-González,** *Protostellar radio variability: A window to high-energy processes in young stars through the eyes of ALMA, VLA, and VLBA*

University of Hertfordshire UH

Booth 11 – P21	**Shaviga Rastogi,** *Detection of plant damage using an E-nose*
Booth 11 – P22	**Mahdi Mohseni,** *The use of BASHTI as an organic ACL fixation technique*
Booth 12 – P23	**Roopesh Sureddi,** *Thermodynamic Analysis of R32 Heat Pump System for Domestic Hot Water Generation*
Booth 12 – P24	**Samuel Sutton,** *Constrained-type Particle Swarm Optimisation for Asynchronous Irregular Behaviour in a Loosely Balanced Spiking Neural Network*
Booth 13 – P25	**Seyed Vahid Hosseini,** *Design of a hybrid concentrated solar – micro gas turbine CHP system*
Booth 13 – P26	**Chloe Bosomworth,** *A Multi-object Spectroscopic Survey of HII regions in M31*
Booth 14 – P27	**Emil Dmitruk,** *Topological insight into brain dynamics during task execution*
Booth 14 – P28	**Nik Dennler,** *Characterisation Experiments for a Multichannel Electronic Nose*

Open Forum Discussion

Download here

Mahmoud Eltaweel	*Flywheel Energy Storage System, is it the future for internal combustion engine vehicles?*
Adrian Felix	*Stress and deformation analysis of shaft-mounted permanent magnet rotor of high-speed CHP micro-turbine*
Jean-Baptiste Hervé	*Comparing PCG metrics with Human Evaluation in Minecraft*
Fiona Jepleting	*Study of the Effect of Stacking Sequence on the Bending Resistance of Composites using Finite Element Analysis*
Bridget Kogo	*Design a Boundary Condition for Deformation Detection in a Stainless-Steel Grade 316 and Mild Steel X65 Weld*
James McGarry	*The spatially resolved radio continuum – star formation rate relation in a sample of nearby spiral galaxies*
Najeeb Moraby	*Computer Simulation of a Poly Nanofiber Patch Under a Mechanical Loading*
Vishwa Patel	*Network Design and Simulation for the Internet and IoT*
Zaid K. Raqqad	*Environmentally Sustainable Construction*
Ali Rouhbakhsh	*Ceramic 3d printed high-speed shaft design for micro gas turbine*
Amir Sajedi	*Design a bionic tendon clip for triple graft suspensory fixation*
Yasser Sorouraddin	*Moving from fossil energy to renewable energy; a business perspective*
Atena Susanabadi	*Reinforcement of Soil Support Cells using Super laminate technique*

Plenary Session

chaired by Professor Pandelis Kourtessis

University of Hertfordshire UH

Aerosol Science: Revealing Complexity and Exploring Multi-Disciplinarity

Jonathan P. Reid[1], Kerry J. Knox[2], Adam Boies[3], Rachael E.H. Miles[1], Darragh Murnane[4]

[1]School of Chemistry, University of Bristol, Bristol, BS8 1TS; [2]Department of Education, University of York, York, YO10 5DD; [3]Department of Engineering, University of Cambridge, Maxwell Centre, Cavendish Laboratory, JJ Thomson Avenue, Cambridge, CB3 0HE; [4]Centre for Topical Drug Delivery and Toxicology, School of Life and Medical Sciences, University of Hertfordshire, Hatfield, Herts AL10 9AB

Keywords: aerosols, environment, inhalation, disease transmission, materials, doctoral training, Team-Based Learning

Aerosol Science : Common Challenges

Aerosol science addresses any scientific or technological problem involving the dispersion of particles (as solids or liquids) in air. Particles can span from the nano to the milli-metre scale and can be at concentrations spanning from 1 per Litre of gas (e.g. in exhaled droplets) to 10,000-100,000 per cm^3 (e.g. in polluted urban environments or in drug delivery systems) or to even higher concentrations (e.g. in dense sprays). Aerosol science is core to a broad range of disciplines extending from drug delivery to the lungs, to disease transmission, aerosol routes to the manufacture of new materials, combustion, environmental science, and the delivery of consumer and agricultural products.

The research challenges that must be addressed in aerosol science are, perhaps unsurprisingly, very similar. As examples, the micro-architecture and phase of aerosol particles (e.g. solution, amorphous, crystalline) are crucial to: health impacts of aerosol (e.g. viability of bacteria, solubility of drugs on inhalation); the function of manufactured particles (e.g. light interactions with pigments, preservation of biologics in spray-drying); the impaction of particles on surfaces (e.g. volcanic ash in jet engines, distribution of agrochemical sprays); and air quality and climate change (e.g. particulate matter in urban environments, ice cloud formation).

Transforming Training in Aerosol Science

Training in aerosol science has mostly been fragmentary, occurring within the context of individual disciplines (e.g. inhaled drug delivery, formulation science, environmental aerosol). However, the aim of the EPSRC Centre for Doctoral Training (CDT) in Aerosol Science is to deliver a paradigm shift in the training of future scientists, lay the foundations for enhanced national research capacity, and redefine and strengthen the interdisciplinary community of aerosol science [1]. Using innovative training approaches (e.g. Team-Based Learning for postgraduate training) that draws on expertise from across a broad range of disciplines, postgraduate researchers receive training in the fundamental principles of aerosol science, develop an ability to apply their knowledge across disciplinary boundaries, and an agility to be at the vanguard of these rapidly evolving fields.

Catalysing Multi-Disciplinary Collaborations

With over 80 academics from 7 institutions now members of the CDT and approaching 70 industrial and public sector partners, the CDT provides unique opportunities to develop new collaborations across institutions, faculties and between disciplines that would not have otherwise occurred. Intentionally, these interactions are developed through establishing mentoring teams for each postgraduate researcher from academia and industry, supporting Thematic Broadening Sabbaticals and Industry placements for each student. Such multi-disciplinarity is key to addressing the important societal, technological and environmental challenges where aerosols play a critical role.

References

[1] Reid, J. P., Knox, K. J., Boies, A., Miles, R. E. H. & Murnane, D., Revolutionizing training in aerosol science (2022). International Environmental Technology, **32** 1 (January/February).

Indoor dispersion at Dstl and its recent application to COVID-19 transmission

Timothy Foat[1,2]

[1]*Dstl, Porton Down, Salisbury, Wiltshire, SP4 0JQ, UK*

[2]*School of Physics, Engineering and Computer Science, University of Hertfordshire, Hatfield, AL10 9AB, UK*

Keywords: indoor dispersion, computation fluid dynamics, eddy diffusion, COVID-19

Introduction

Dstl (Defence Science and Technology Laboratory) has been studying indoor dispersion for over 20 years, to assess the hazard from toxic airborne material and to improve the detection of explosives. They use both experimental and theoretical methods to study the transport of aerosol, gas and vapour in a range of different indoor environments. Indoor spaces are of particular interest from a defence and security perspective as they may contain large numbers of people and concentrations can remain relatively high for extended periods of time, due to the limited volume and supply of fresh air.

This presentation will describe some of the different mathematical modelling methods available for indoor dispersion, which span from the high-resolution computation fluid dynamics (Fig. 1, left) to single zone models. The presentation will cover the pros and cons of the different approaches in relation to the problem being addressed and will then focus on two specific applications: eddy diffusion modelling (Fig. 1, right) and COVID-19 transmission.

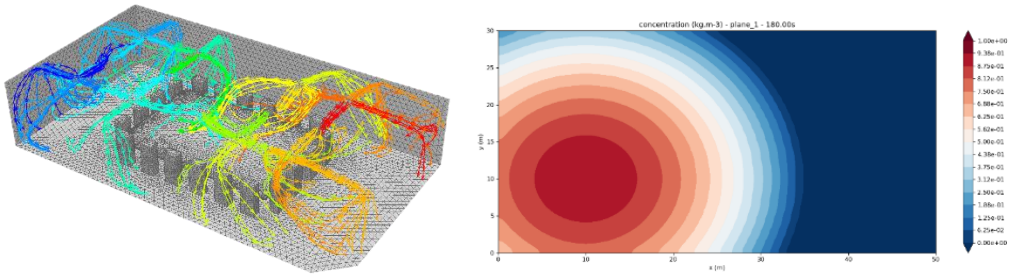

Fig. 1 – CFD predicted airflows from eight supply vents in a typical mechanically ventilated office space (left). Concentration contours from an eddy diffusion model (right).

Session 1. Security, Protection, Care

chaired by Dr Loic Coudron

University of Hertfordshire UH

Non-invasive label-free detection of water molecular markers in large biological samples using Transmission Raman spectroscopy

Adrian Ghita[1], Thomas A. Hubbard[2], Pavel Matousek[3], Nicholas Stone[4]

[1]School of Physics, Engineering & Computer Science, Department of Physics, Astronomy and Mathematics, University of Hertfordshire, Hatfield, AL10 9AB, UK

[2]Institute of Biomedical and Clinical Science, University of Exeter Medical School, Exeter EX1 2LU, /Royal Devon and Exeter Hospital, Exeter EX2 5DW, U.K.,

[3]Central Laser Facility, Research Complex at Harwell, STFC Rutherford Appleton Laboratory, Oxfordshire OX11 0QX, U.K.

[4]Biomedical Spectroscopy Lab, School of Physics and Astronomy, College of Engineering, Mathematics and Physical Sciences, University of Exeter, Exeter EX4 4QL, U.K.

Keywords: Raman spectroscopy, biological tissue, water, malignancy

Elevated water levels have been reported in various type of malignancies and has been associated with biochemical changes in pathology of the tissue [1]. Hence, the need for new analytical/imaging methods in biomedical research, to uncover the chemical makeup of these water containing biological formation, as well as to understand underlying biochemical processes. The recent progress in the field of bio-photonics have afforded Raman spectroscopy to advance as a suitable tool for molecular profiling of for various types of biological samples [2, 3]. Here we demonstrate conceptually a capability of monitoring these changes using deep Raman spectroscopy employing a 680nm laser in conjunction with customized dispersive wavelength analyser. Water was added by injection into an isolated region of biological sample representing a 20% increase in water content. The elevated water content was detected through 20 mm of tissue in its centre using Transmission Raman Spectroscopy (TRS) by monitoring the relative ration between CH (2940 cm^{-1}) and OH (3390 cm^{-1}) [4] Raman bands. The sample was raster scanned to yield a spatially map of the water concentration throughout the sample volume. The results presented here provide the first building block towards establishing a non-invasive tool for in-vivo detection of elevated water content as a marker for cancer lesion.

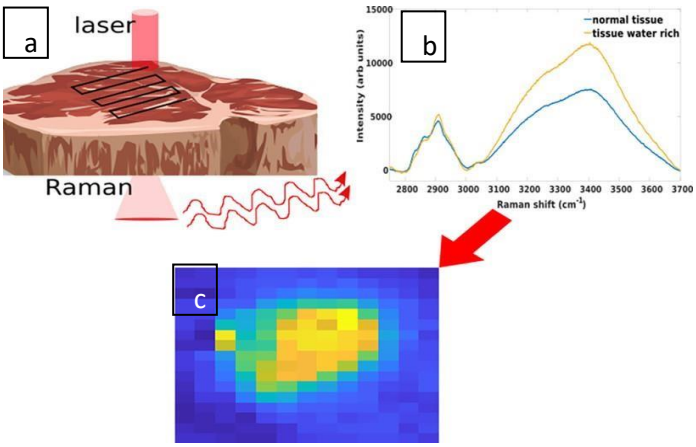

Fig. 1 –a) graphical schematics of the laser raster scanning of phantom tissue sample; b) Raman spectra of tissue samples in high wavenumber region; c) Raman mapping of water peak in tissue

References

[1] Quarto, G *et al* (2014) P. Biomed. Opt. Express, **5** (10), 3684.

[2] Ghita, A. . *et al* (2018) N. J. Biophotonics, **11** (1), No. e201600260

[3] Ghita, A. . et al (2012) Anal Chem., 84 (7), 3155-3162

[4] Unal, M. et al. (2015) Bone, 81, 315−326.

University of Hertfordshire UH

Mitigating motorcycle accidents at yield junctions using computer vision and deep learning: a preliminary study

Simon McCool, Volker Steuber, Wei Ji and Christoph Salge

School of Physics, Engineering and Computer Science, University of Hertfordshire, College Lane, Hatfield, AL10 9AB, s.mccool@herts.ac.uk

Abstract

Accidents involving motorcycles are significantly higher at un-signalised junctions. Recent accident prevention technology for motorcycles is limited to systems designed to scan the environment detecting possible hazards in navigation paths. An accurate prediction of future trajectories could further mitigate the severity of a collision. Therefore, using only monocular video and deep learning methods, we detect, track, and analyse vehicles approaching a junction to predict yield intent before the vehicle enters the motorcycle's navigation path where current rider aids would be triggered. We investigate two methods: real-time predictions based on data passed from deep learning live tracking metrics and perceptron classification prediction from a linear classifier trained on driver behaviour profiles.

Keywords— Motorcycle Junction Accident, Intent Prediction, Computer Vision, Deep Learning, YOLOv5

Introduction

Predicting another driver's intent is an inherent driver's skill and essential to the act of driving. Autonomous vehicles (AV) are also prone to unintended bias against vulnerable road users (VRU). Research by the Netherlands vehicle authority (RDW) highlighted that vehicles equipped with advanced driving aids needed human intervention to prevent a collision with a vulnerable road user (VRU). RDW warns that systems do not always see and react to small objects like motorcycles [1]. Vehicles controlled by humans, AV, or a mix of both, pose the most significant risk to a motorcyclist at yield junctions. This paper is preliminary work using simulated environmental conditions from a motorcyclist's perspective and explores how to predict a human driver's intent at an unsignaled junction on UK roads using deep computer vision (CV) and deep learning (DL). Deceleration profiles studies [2] identify a trend toward higher acceptable deceleration thresholds for intersection approaches and suggest drivers will decelerate progressively towards the junction rather than suddenly stop; this investigation builds on this work and will go towards research to shape our baseline for driver intent profiles. Our intent predictions can be amalgamated with appropriate accident mitigation technology to advance the motorcycle-based ADAS's safety windows and, by future experimentation, determine how additional safety margin affects the outcome of previously inevitable collisions.

Experimental

Predicting the intent of a vehicle at a junction requires analysis of the 2D input; feature data has to be extracted from each video frame to create optical flow data. We use YOLOv5s for object detection and DeepSORT for tracking in real-time. We use the frame by frame tracking data to generate dataset data and compare the current track to previous track data. Input is in 2D video imagery, which is passed to YOLOv5 for object detection and classification; bounding box reference data predictions are generated and drawn around the object. Bounding box inference data is passed to DeepSORT as a feature vector describing the object contained in the image. The DeepSORT NN analyses the feature vector to estimate a track using an assigned ID. Once an ID is assigned, a tracking vector is created for subsequent frame predictions. Our algorithm takes that vector data and analyses the differential values to predict if the vehicle will yield at the junction. Initial 2D depth estimation used data using handcrafted features from a 2D image [3]; this proved accurate but lethargic. A DNN was developed using a persistent random field for image patches to estimate total image depth [4]. The above methods require precise depth supervision, excluding them from any real-time application. In the absence of depth image as ground truth, it is possible to estimate the distance of an object in the image [5] [6] [7] [8] from the height of objects. In this manner, the distance can be calculated with the pixel height h and the real-world height h_w and f_y focal length of the object by; $d = h_w f_y / h$ (1). To estimate the velocity of the target vehicle, we employed some of the methods in [9] in which a minimal and straightforward monocular vision-based approach is proposed. Velocity is calculated using the distance metric described above and the flow of the bounding box transposed during the tracking stage. We define the location where a target vehicle stops at the

line demarking the junction exit and calibrate all distance variables from this point. To capture driver intent, the analysis of current and past data is required. This data combines bounding box top left-x coordinates and top left-y coordinates a width and a height value a class, id and a confidence score for several past time steps. Data capture is instigated by isolating elements of the array and measuring the relationship with the movement of target vehicles in simulation.

Results and discussion

Method 1: Real-time predictions

Predictions using real-time data from the tracking cascade were triggered approximately 30m from the junction line-markings and then compared to their later yield behaviour, see Tab.1. and Fig. 1.

Intent prediction												
Predicted	1	1	1	2	2	2	3	3	3	4	4	4
Observed	1	1	3	2	1	1	3	3	4	3	4	4
Precision	1 = 66.7%, 2 = 33.3%, 3 = 66.7%, 4 = 66.7%											

Table 1. Intent predictions from the target vehicle at 30 m compared to observed action at the junction. Key for table 2: stop and yield = 1, merge yield = 2, slow no stop = 3, no slow no yield = 4

Fig.1. Visual intent predictions using real-time data.

Realtime data capture allowed us to make an intent prediction 30 m from the junction and update every 1 s until the stop line. Fig. 1. left image target vehicle predicted to yield, and the right image shows the target predicted no yield.

Method 2: Linear classifier method

Intent profiles were generated from velocity and distance data captured during real-time intent predictions. We collapsed classes for the linear classification method as there was too much overlap, and we required a binary result of yield or no yield. This data formed a small dataset similar to [10] of intent profiles to train a linear classifier. Test data accuracy was 0.97. Using a confusion matrix as an alternate method for the performance of the whole model, we get an accuracy of 0.89, as seen in Tab. 2.

N=66	Predicted yield	Predicted no yield
Actual yield	37	3
Actual no yield	4	22

Table 2. Confusion matrix for the complete linear classifier

Conclusion

As the first step in a larger body of work, we investigated two methods to predict driver intent to determine how an additional ADAS safety margin created using CV and DL affects the outcome of previously inevitable motorcycle collisions. Firstly we use an unsupervised real-time method to overcome the lack of labelled data. We observed vehicles approaching a simulated yield junction environment and manually recorded the intent predictions produced by using a minimal and intuitive approach that captures the target vehicle tracking cascade data. This minimises the computational overhead as the distance from the junction line, and the target vehicle's velocity estimations can be generated from concurrent processes. We produced precision metrics from individual classes. Our second method input 66 hypothetical behaviour profiles based on *v* and *d* data in method one into our linear classifier and achieved an accuracy of 0.89. While our second method did not run in real-time, it did prove to be slightly more accurate. We can improve accuracy by incorporating the linear classifier into the tracking cascade in future work while maintaining high performance. Evaluation of the results indicates that although the intent predictions from both methods showed promise on simulated data, it proved the feasibility of the framework rather than evidence of a conclusive study as real-world dynamics increase

complexity. MAEB systems are prone to instability [11] [12] if initiated too quickly; having an increased trigger time would not only help to mitigate a collision with a target vehicle but reduce the severity of the automated braking action required. Our contribution emphasises the need for real-time processing and that a minimal approach is required to apply an effective and timely solution to driver intent at junctions. Our subsequent study will focus on determining the effect of an intent prediction on an imminent collision scenario on a moving platform from non-yielding vehicles contributing to and developing [13] [14].

Reference list

[1]FEMA, "RDW: 'Adaptive Cruise Control Does Not Always See Motorcyclists,'" 2021.
[2]M. A. Perez, Z. R. Doerzaph, and V. L. Neale, "Driver Deceleration and Response Time When Approaching an Intersection: Implications for Intersection Violation Warning," *Proceedings of the Human Factors and Ergonomics Society Annual Meeting*, vol. 48, no. 19, pp. 2242–2246, Sep. 2004, doi: 10.1177/1541931204480108.
[3]A. Saxena, "Convolutional Neural Networks (CNNs): An Illustrated Explanation," *XRDS*, Jun. 29, 2016. https://blog.xrds.acm.org/2016/06/convolutional-neural-networks-cnns-illustrated-explanation/.
[4]Q. Chu, W. Ouyang, B. Liu, F. Zhu, and N. Yu, "DASOT: A Unified Framework Integrating Data Association and Single Object Tracking for Online Multi-Object Tracking," *Proceedings of the AAAI Conference on Artificial Intelligence*, vol. 34, no. 07, pp. 10672–10679, Apr. 2020, doi: 10.1609/aaai.v34i07.6694.
[5]G. Savino, J. Mackenzie, T. Allen, M. Baldock, J. Brown, and M. Fitzharris, "A robust estimation of the effects of motorcycle autonomous emergency braking (MAEB) based on in-depth crashes in Australia," *Traffic Injury Prevention*, vol. 17, no. sup1, pp. 66–72, Sep. 2016, doi: 10.1080/15389588.2016.1193171.
[6]Y. Zhang *et al.*, "A regional distance regression network for monocular object distance estimation," *Journal of Visual Communication and Image Representation*, vol. 79, p. 103224, Aug. 2021, doi: 10.1016/j.jvcir.2021.103224.
[7]J. Zhu and Y. Fang, "Learning Object-Specific Distance From a Monocular Image," 2019. Accessed: Dec. 23, 2021.
[8]S. Workman, C. Greenwell, M. Zhai, R. Baltenberger, and N. Jacobs, "DEEPFOCAL: A method for direct focal length estimation," *2015 IEEE International Conference on Image Processing (ICIP)*, Sep. 2015, doi: 10.1109/icip.2015.7351024.
[9]R. A. Rill, "Intuitive Estimation of Speed using Motion and Monocular Depth Information," *Studia Universitatis Babeș-Bolyai Informatica*, vol. 65, no. 1, pp. 33–45, Jul. 2020, doi: 10.24193/subbi.2020.1.03.
[10]"Prediction of Black Sigatoka Disease in Banana Plants By Data Mining Classification Techniques using Scikit for Python," *International Journal of Innovative Technology and Exploring Engineering*, vol. 9, no. 3, pp. 1273–1278, Jan. 2020, doi: 10.35940/ijitee.c8714.019320.
[11]C. Lucci, N. Baldanzini, and G. Savino, "Field testing the applicability of motorcycle autonomous emergency braking (MAEB) during pre-crash avoidance manoeuvre," *Traffic Injury Prevention*, vol. 22, no. 3, pp. 246–251, Mar. 2021, doi: 10.1080/15389588.2021.1884235.
[12]M. Rizzi, J. Strandroth, and C. Tingvall, "The Effectiveness of Antilock Brake Systems on Motorcycles in Reducing Real-Life Crashes and Injuries," *Traffic Injury Prevention*, vol. 10, no. 5, pp. 479–487, Sep. 2009, doi: 10.1080/15389580903149292.
[13]D. Phillips, T. Wheeler, and M. Kochenderfer, "Generalisable Intention Prediction of Human Drivers at Intersections," 2017. Accessed: Dec. 07, 2021. [Online].
[14]P. Fekri, V. Abedi, J. Dargahi, and M. Zadeh, "A Forward Collision Warning System Using Deep Reinforcement Learning," *SAE Technical Paper Series*, Apr. 2020, doi: 10.4271/2020-01-0138.

University of Hertfordshire UH

Evaluation of 2D Acoustic Signal Representations for Acoustic-Based Machine Condition Monitoring

Gbanaibolou Jombo[1*], and Ajay Shriram[1]

[1]Centre for Engineering Research, School of Physics, Engineering, Computer Science, University of Hertfordshire, UK

*corresponding author: g.jombo@herts.ac.uk

Abstract

Acoustic-based machine condition monitoring (MCM) provides an improved alternative to conventional MCM approaches, including vibration analysis and lubrication monitoring, among others. Several challenges arise in anomalous machine operating sound classification, as it requires effective 2D acoustic signal representation. This paper explores this question. A baseline convolutional neural network (CNN) is implemented and trained with rolling element bearing acoustic fault data. Three representations are considered, such as log-spectrogram, short-time Fourier transform and log-Mel spectrogram. The results establish log-Mel spectrogram and log-spectrogram, as promising candidates for further exploration.

Keywords: Machine Condition Monitoring, Detection and Classification of Anomalous Machine Operating Sound, Industrial Sound Analysis, Machine Hearing.

Introduction

Machines are the backbone of industry; their fault-free operation is vital to lower operating cost. To ensure this, condition monitoring approaches such as vibration analysis and lubrication monitoring, among others have been adopted. In industrial settings, it is not uncommon for experienced maintenance engineers to develop an ear-based perception of the health of machines. Acoustic-based machine condition monitoring (MCM) is a means to formalise this observed inert behaviour in experienced maintenance engineers. The analysis of sound for speech, music and acoustic event recognition are well developed for creating smart and interactive technologies [1]. However, in the context of machine fault diagnostics, this presents an emerging research area for the detection and classification of anomalous machine operating sounds (DCAMS). Within the context of DCAMS and the application of deep learning to address anomalous sound detection and classification task, the format of 2D representation of acoustic signal is vital [2]. For speech and music acoustic event recognition, this representation has been addressed [1,3]. Within the domain of machine condition monitoring, this is still required. Therefore, this study mainly investigates the effectiveness of various 2D acoustic signal representation for training a baseline convolution neural network (CNN) to address the task of classification of anomalous machine sound.

Experimental

Experimentation is performed on a rolling-element bearing fault rig with setup consisting of 0.55 kW electric motor driving a lightly-spring-loaded (axial and radial) deep groove ball bearing (SKF 6207) through a drive shaft with a flexible coupling, as shown in Fig. 1.

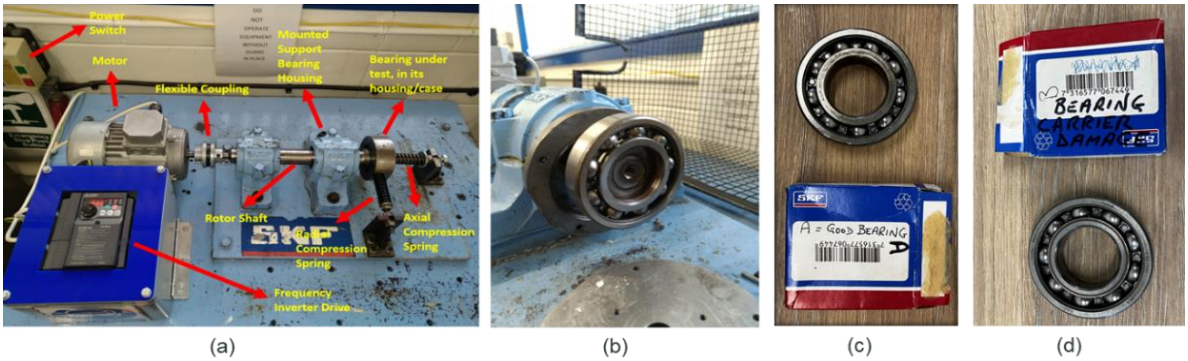

Figure 1. Experimental setup: (a) rolling-element bearing fault test rig, (b) test bearing housing, (c) healthy bearing, and (d) bearing with cage defect fault.

The test bearings in Fig. 1 consist of healthy ball bearing and ball bearing with cage defect. Test conditions include running at incremental speeds of 300, 600, 900, 1500 and 2400 rpm. Acoustic data for machine operating sound is acquired, using Ultramic USB ultrasound microphone sampling at 250 kHz and SeaWave software.

Results and discussion

CNN is adopted for the benchmarking task for the 2D acoustic signal representation, as it provides model classification accuracy above 98% [4]. CNN takes its inspiration from the operation of the mammalian visual cortex using a multi-staged process, as shown in Fig. 2. This includes feature extraction stage (convolution, pooling, normalisation, and activation layers) and classification stage (fully connected layer of multilayer perceptron). The convolution layer functions to extract feature set into a feature map, pooling layer reduces the dimensionality of the feature map, and the classification stage performs the classification task using the multilayer perceptron. Table 1 presents the parameters of the adopted baseline CNN architecture. Using the CNN model as a baseline, the effectiveness of the following 2D acoustic signal representations is evaluated: log-spectrogram, short-term Fourier transform (STFT) and log-Mel spectrogram. Benchmarking results are presented in Table 2.

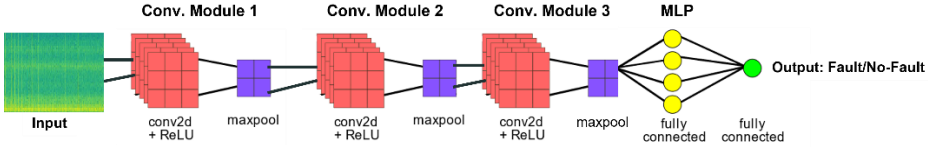

Figure 2. CNN architecture.

Table 1. CNN architecture parameters.

Input	**Conv. Module 1**	**Conv. Module 2**	**Conv. Module 3**	**MLP** (Multi-Layer Perceptron)
shape= 150x150 sound per class: ~45 (train ~35, val. 10)	shape= 16x16, activation = ReLU, max pooling = 2x2	shape= 32x32, activation = ReLU, max pooling = 2x2	shape= 64x64, activation = ReLU, max pooling = 2x2	Flatten, 512 hidden nodes/ ReLU 1 node/ Sigmoid

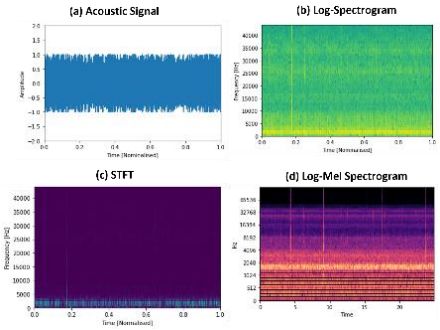

Figure 3. 2D acoustic signal representations.

Table 2. Method benchmarking.

Method + CNN (Not Optimised)	**Accuracy (training)**
Log-Spectrogram	0.5397
STFT	0.4603
Log-Mel Spectrogram	0.5873

Conclusion

The results establish Log-Mel Spectrogram and Log Spectrogram as promising candidates for further exploration. But, the performance of the CNN model has not been optimised, due to a very limited machine acoustic dataset. Therefore, continuous, or future study seeks to achieve the optimisation of the performance of the CNN model.

References

[1] R. V Sharan and T. J. Moir, "Acoustic event recognition using cochleagram image and convolutional neural networks," *Applied Acoustics*, vol. 148, pp. 62–66, 2019, doi: https://doi.org/10.1016/j.apacoust.2018.12.006.

[2] R. F. Lyon, "Machine Hearing: An Emerging Field [Exploratory DSP]," *IEEE Signal Processing Magazine*, vol. 27, no. 5, pp. 131–139, 2010, doi: 10.1109/MSP.2010.937498.

[3] R. V Sharan, H. Xiong, and S. Berkovsky, "Benchmarking Audio Signal Representation Techniques for Classification with Convolutional Neural Networks," *Sensors* , vol. 21, no. 10. 2021. doi: 10.3390/s21103434.

[4] N. F. Waziralilah, A. Abu, M. H. Lim, L. K. Quen, and A. Elfakharany, "A Review on Convolutional Neural Network in Bearing Fault Diagnosis," *MATEC Web Conf.*, vol. 255, 2019, doi: 10.1051/matecconf/201925506002.

Session 2. Engineering a Sustainable Future

chaired by Dr Gabriel Barros dos Santos

University of Hertfordshire UH

Invited Speaker: **The Prospects of Nano materials in energy storage systems**

Yong Chen

Centre for Engineering Research, School of Physics, Engineering, Computer Science, University of Hertfordshire, UK

Nano materials could play a pivotal role for Phase change materials (PCMs) in energy storage systems. Phase change materials (PCMs) are of the high energy storage capacity and extensively used in various applications for thermal energy storage purposes. However, the poor thermal conductivity of PCMs limits their potential in different applications. Nano materials have been introduced into PCMs in order to improve and optimise the potential of nano-PCMs. ENESD group has conducted comprehensive studies in effects of nanofillers on the thermophysical properties (latent heat and thermal conductivity) of the nano-PCMs. We aim to find optimised nano-PCM energy storage systems for buildings in different climates conditions, such as EU, Middle East or North Pole areas. It is hoped that nano-PCM could provide sustainable energy storage systems for those regions.

Modelling and Analysis of ice crystals based on in-situ light scattering patterns

E R Mathen[1*], A J Baran[1,2], E Hesse[1], R S Greenaway[1]

[1]University of Hertfordshire, AL10 9AB, UK.

[2]Met Office, Exeter, EX1 3PB, UK.

*em14abz@herts.ac.uk

Keywords: ice crystals, light scattering, deep learning network, particle classification

Introduction

Cirrus clouds are composed of ice crystals and several authors e.g. [1], [2] have pointed out that there is a lack of detailed information on their microphysical properties such as ice crystal geometry and surface roughness. This is due to challenges like limitations of imaging instruments and scarcity of in-situ measurements. As a result, there are uncertainties in their radiative properties and their effect on climate modelling predictions.

The primary objective of this research is to analyze the scattering patterns of ice crystals in the Tropical Tropopause Layer (TTL), a layer in the atmosphere between the troposphere and stratosphere, and find their characteristics like shape and size distributions, as these can greatly influence their radiative properties and therefore, the atmospheric temperature. As a high cloud, cirrus plays a crucial role in the Earth-atmosphere radiation balance and by knowing the scattering properties of ice crystals, their impact on the radiative balance can be estimated [3]. This research further helps to broaden the understanding of the general scattering properties of TTL ice crystals, to support climate modelling and contribute towards more accurate climate prediction, and the remote sensing of tropical cirrus.

Data

NASA conducted a scientific mission named the Airborne Tropical Tropopause Experiment (ATTREX) from 2011 to 2015 using an unmanned aerial vehicle, Global Hawk, to study the physical and chemical processes in the TTL. The ATTREX 2015 experiment was in collaboration with NERC and Co-ordinated Airborne Studies in the Tropics (CAST) known as the CAST-ATTREX campaign. The in-situ data investigated in this study was taken during one such flight, on 5th March 2015 during the CAST-ATTREX mission, at an altitude between 15-16km over the Eastern Pacific Ocean. The data is a collection of 2D light scattering patterns (greyscale images of 512x640 resolution) captured by the Aerosol Ice Interface Transition Spectrometer (AIITS) [4], which is capable of detecting particles of size range 1-100µm at the wavelength of 532nm. The scattering pattern covers 6° - 25° of the forward scattering hemisphere and there are 2426 images in total.

Method

The morphology of the crystals can be identified by analyzing the features in the 2D light scattering patterns as the features vary depending on the geometry of the ice crystal. However, manual analysis of scattering patterns is time-consuming and therefore, a pilot study using some Deep Learning (DL) algorithm has been undertaken to classify the scattering patterns and identify different ice crystal habits such as rough, pristine or rounded hexagonal prisms. To further speed up the process, a DL Network based on Transfer Learning using a pre-trained network called GoogLeNet with 144 layers, is under development. After the analysis phase, model crystals for the light scattering computations are generated. Rough crystal models are generated using the method described in [5]. The scattering data of the model crystals are then simulated using Beam Tracing Models (BTM) [6][7] based on physical optics (two examples are shown in Figure 1 (a) and (b)). By successive testing and further analysis, the crystal sizes are estimated.

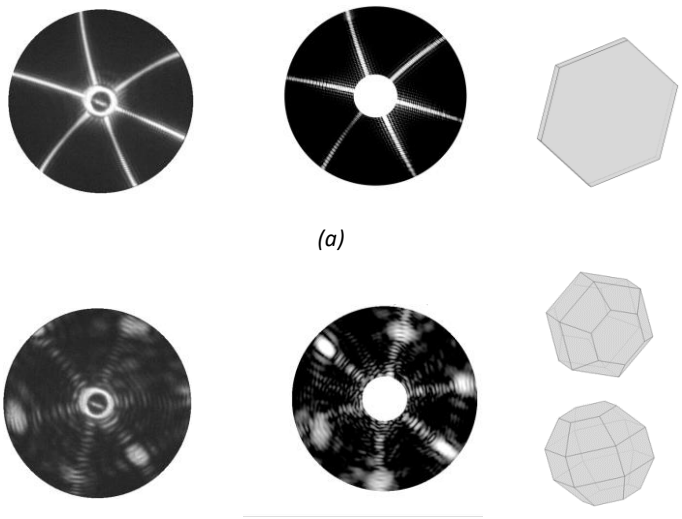

(a)

(b)

Figure 1. (a) An AIITS image with a beam-stop in the centre (left), simulated pattern using BTM [4][5] (middle) and the corresponding model crystal (plate) in specific orientation (right) used to generate the simulated pattern. (b) Another AIITS image with a beam-stop in the centre (left), simulated pattern using BTM [4][5] (middle) and the corresponding model crystal (droxtal) in specific orientation (top right) used to generate the simulated pattern and side view of the crystal (bottom right).

Results

Based on manual analysis, out of 2426 patterns, only a subset of 803 images (33.10%) can be used; the remaining ones were either blank or only the artefacts between 0° and 8° were visible, and hence discarded. The statistics are given in Table 1.

Crystal Categories	Number	Percentage
Rounded	426	53.05 %
Columns	152	18.93%
Plates	43	5.35%
Rough	161	20.05%
Rough and Rounded	21	2.62%
Total	**803**	**100%**

Table 1. Classification of AIITS scattering patterns (images) into different crystal types and textures.

From Table 1, the most common crystal type is 'Rounded' crystal (53.05%). The Rounded category consists of crystals with significantly rounded edges and was split into 4 different size groups, based on the number of rings in the scattering pattern. In small rounded crystals' scattering patterns, 1 to 6 rings were visible and there were 194 of these crystals. As the name indicates, this category includes small plates with rounded edges. However, droxtals and pristine crystals with radius ≤ 1µm are also likely to be in this group, as their scattering patterns show ring-like features and it is often difficult to distinguish them from the actual spheroidal crystals. As a result, it is impractical to accurately classify them as quasi-spherical, spheroids, droxtals, pristine hexagonal plates etc. The other 3 categories were 114 medium rounded crystals with 6 to 12 rings, 99 medium to large rounded crystals with 12 to 18 rings, and 19 large rounded crystals with 18 to 22 rings.

Crystals in the 'Columns' category were further divided and there were 2 extremely thin solid columns (also called needles), 123 small columns with length ≤ 10µm, 18 intermediate columns with length between 10-20µm and 9 large columns with length > 20µm making a total of 152. Out of 43 Plates, there were 3 scalene plates, 14 droxtals, 5 pristine plates, 18 plates with rounded edges and 3 others were rough. The 'Rough' category consists of 161 crystals with rough surface texture. Crystals of the least common type, 'Rough and Rounded' (2.62%), have rough texture and rounded edges.

A DL code for classifying the large dataset of scattering patterns captured by the AIITS is under development. So far, the network has been trained to classify four types of crystals (Blank, Plates, Rounded and Patterned) using

supervised learning. The DL Network examines the greyscale image and predicts the probability of crystal type in descending order. An example is shown in Figure 2, in which the program correctly categorizes the scattering pattern of a rounded crystal.

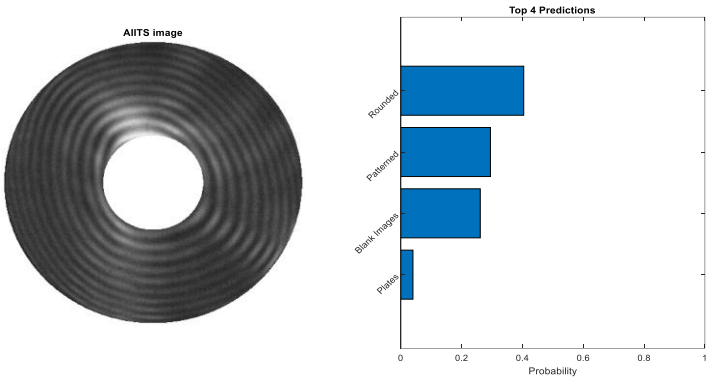

Figure 2. AIITS light scattering pattern image (left) and the probability of crystal type predicted by the Deep Learning Network (right).

Conclusion

Different types of crystals exhibit different features in their scattering pattern. By successive testing and closely studying these features, crystals are classified and the crystal sizes are estimated. Based on the current results, more than half of the crystal population possess rounded edges and most of them are small crystals. This agrees with the results from 2014 ATTREX sampling, over the TTL cirrus of the Western Pacific summarized in [8], *"Observed ice particles were predominantly small and quasi-spheroidal in shape."*

The DL Network can make the image processing and classification easier for future AIITS scattering pattern analysis. Although, this is at too early stage to comment on the accuracy of the network, in general, there is a good agreement between manual and the network's classification. More crystal categories will be included in the near future.

References

[1] Jensen, E. and Pfister, L., Transport and freeze-drying in the tropical tropopause layer. Journal of Geophysical Research, 109(D2) 2004.

[2] Kärcher, B., Formation and Radiative forcing of Contrail Cirrus. Nature Communications, 9(1) 2018.

[3] Baran, A. J., Journal of Quantitative Spectroscopy and Radiative Transfer **110**(14-16) 1239-1260, 2009.

[4] Hirst, E., Stopford, C., Kaye, P.H., Greenaway, R.S., Dorsey, J.D., The Aerosol Ice Interface Transition Spectrometer – A new particle phase, ATTREX Science Meeting, Boulder, USA, 2013.

[5] Collier, C.T., Experimental and Computational Investigation into Light Scattering by Atmospheric Ice Crystals, PhD thesis, University of Hertfordshire, 2014.

[6] Taylor, L.C., A Beam Tracing Model for Electromagnetic Scattering by Atmospheric Ice Crystals, PhD thesis, University of Hertfordshire, 2016.

[7] Hesse, E., Taylor, L., Collier, C.T., Penttilä, A., Nousiainen, T., Ulanowski, Z., Journal of Quantitative Spectroscopy and Radiative Transfer **218** 54-67, 2018.

[8] Woods, S., Lawson, R. P, Jensen, E, Bui, T.P., Thornberry, T., Rollins, A., Pfister, L., Avery, M., Microphysical Properties of Tropical Tropopause Layer Cirrus. Journal of Geophysical Research: Atmospheres, 10.1029/2017JD028068, 123, 11, 2018.

University of Hertfordshire UH

Can 'Innovation Integration' and 'Digital Twins' Help Solve Energy Supply Problems?

***Colin Mallett,[1,2] Soodamani Ramalingam[1]**

[1] University of Hertfordshire [2]CEO, Trusted Renewables Ltd;

*corresponding author: colin@trustedrenewables.com

Abstract

Making energy systems carbon-neutral faces question of affordability. Smarter energy ecosystems help with an edge-of-network distributed energy resource ecosystem consisting of emerging Internet of Things architectures. This includes local energy storage and smart energy optimisation and mediation platforms. Behind-the-meter architecture supports peer to peer energy trading using distributed ledger technology smart contracts and non-fungible tokens. A digital twin can be used for Industrial research to evaluate emerging commercial and technical architectures and de-risk large-scale deployments allows investigation of new use cases with appropriate commercial and technical architectures.

Keywords: Blockchains, smart contracts, IoT, smart energy, solar PV, digital twins, non-fungible tokens.

Introduction

The UK energy sector is in transition. To avoid societal problems, energy bills need to remain affordable whilst meeting net zero climate goals. This includes avoiding fuel poverty.

New smart flexible energy systems are emerging which can mitigate these problems. 'Behind the meter' energy ecosystems are emerging where users become 'prosumers'. This can transform the way energy is generated, along with how and when it is used and paid for. This includes local energy trading. The UK government is aware of this and has published a number of reports including the 'Smart Systems and Flexibility Plan' [1] and the 'Alternative Energy Markets Programme'. It has also been recognised that blockchains will have a major role to play [2], along with distributed ledger technology (DLT) [3] and Smart Contracts [4].

In accordance with our title, our specific focus is to understand how flexibility markets can manage supply problems. This takes two forms - *generation-side flexibility* and *demand-side flexibility*. On the generation side, gas-fired 'peaking' plants are used to satisfy intermittent demand, whilst 'plunge' tariffs [5] encourage investment in electricity storage to mitigate overgeneration from offshore wind on stormy nights. New consumer Time-of-Use (ToU) tariff structures encourage flexible demand, with customer load shifting during a 24-hour period. Mediation presents some particularly interesting opportunities with 'demand-side' flexibility.

Engineering doctorate (EngD) studies can be a portfolio of Industrial Research (IR) projects which address real-world challenges. Energy supply problems are certainly one of these and the full programme is entitled 'Trustworthy Energy Ecosystems Based on Emerging Blockchain and IoT Architectures'. Innovate UK (IUK) define IR as "planned research to gain new knowledge" and includes "creation of complex system component parts, laboratory prototypes or simulated interfaces to existing systems [6]." Many of the EngD use cases in this programme were funded by IUK and includes developing commercial and technical architectures along with seamless integration of hardware, software and ICT platforms. We call this 'innovation integration.' This paper reports results of some of our work which will be brought together in the final EngD thesis.

Experimental

One IUK project involved deployment of a UH development platform at the BRE innovation Park in Watford. This was part of the IUK 'Integrating Smart Homes with Smart Meters' programme. Since then, the idea of using a 'Digital Twin Prototype' (DTP) has emerged. This allows experimental validation of different use cases, architectures and solutions with a "real-time digital counterpart of a physical object or process" [7]. Such an entity often exists before the physical system and can significantly de-risk commercial development and testing of new system properties. The DTP is continually updated throughout the system life cycle and can be distributed across a number of physical locations, or for that matter continents. For this reason, they are usually taken to be wider in scope than simply a testbed or sandbox [8]. This is the true in our case where we have a number of experimental set-ups. One residential version contains a Liberty 100 smart meter (from Secure Meters Ltd), solar slates (from GB-Sol) and local energy storage (Moixa).

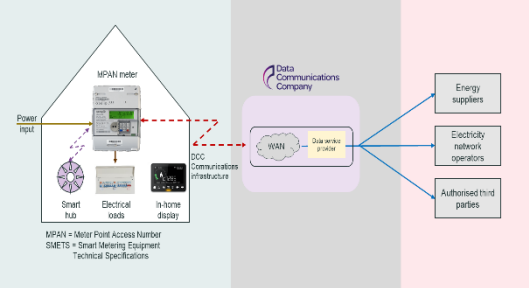

Figure 1 Smart metering

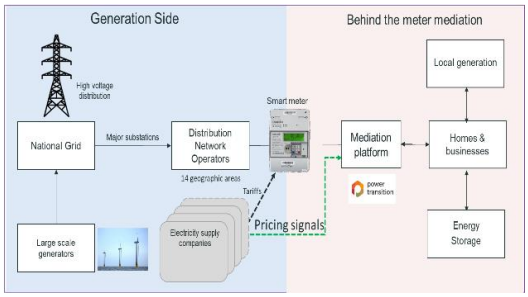

Figure 2 behind-the-meter-mediation.

Within an energy ecosystem, smart meters play a critical role. They send metering data to energy suppliers, energy network operators and importantly, 'authorised third parties' via the Data Communications Company (DCC). Figure 1 shows how these interact with energy suppliers, acting as a 'boundary meter' connected to the Distribution Network Operator (DNO) and identified by an MPAN (Meter Point Access Number).

Figure 2 shows how the mediation platform receives pricing signals from the energy suppliers. One example is the Digital Energy Platform (DEP) developed by Power Transition Ltd (PTL). This is based on DLT and uses Hedera Hashgraph [9] which is particularly well suited to mediation and energy trading.

Results and discussion

We examined a small manufacturing company as a use case in one of our IUK 'behind the meter' local energy systems and peer-to-peer (P2P) energy trading projects. This is shown in Figure 3. As shown previously, the boundary meter interfaces to the grid and the DCC, but rather than being connected directly to the enterprise, it now links individual sites via a smart energy ecosystem. Enterprises still use a smart meter although this now sends and receives data to and from the mediation platform instead of the DCC. Figure 3 also shows a smart energy management system which is also linked to it. Production machinery can be programmed to operate automatically and thus benefit from cheap ToU electricity tariffs when the premises are unattended.

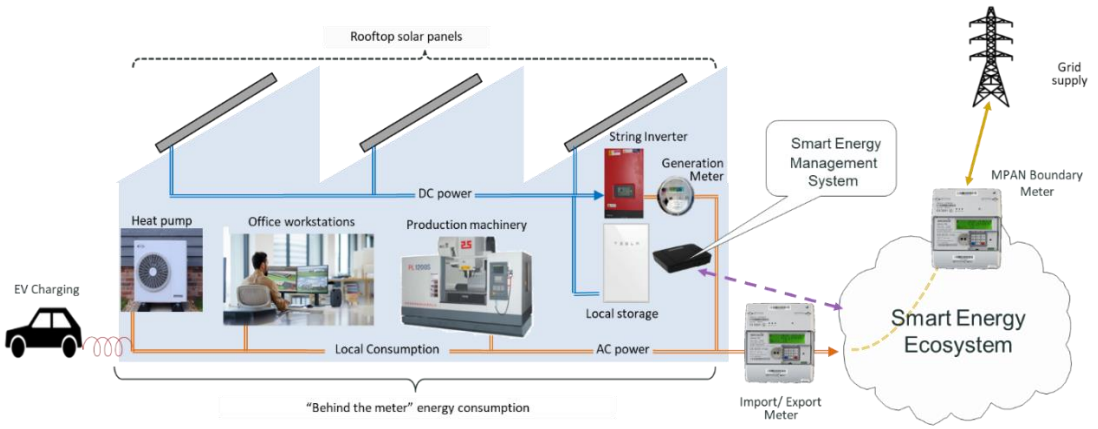

Figure 3 Enterprise Smart Energy Architecture

The enterprise can benefit from the Flexibility market. Sometimes it may be self-sufficient with locally generated electricity and other when the mediation platform receives pricing signals indicating that it is advantageous to purchase grid electricity. Energy storage can mitigate intermittency associated with local renewable energy generation and allow the company to ride out very high ToU tariffs.

The UK government encourages breaking down existing policy and regulatory barriers with new smart technologies and business models [10]. Localised energy systems (LES) based on 'behind the boundary meter' P2P smart energy trading is one of these. However, selling electricity to the general public (as opposed to a closed community) requires a public electricity supplier licence from Ofgem [11]. The commercial framework for participants to offset their own electricity consumption and feed surplus renewable energy back into the grid as part of a closed group is possibly simpler. Figure 4 shows a scheme appropriate to a science park or operations such as BRE with separate commercial operations on a campus site. As shown in Figure 3, each enterprise

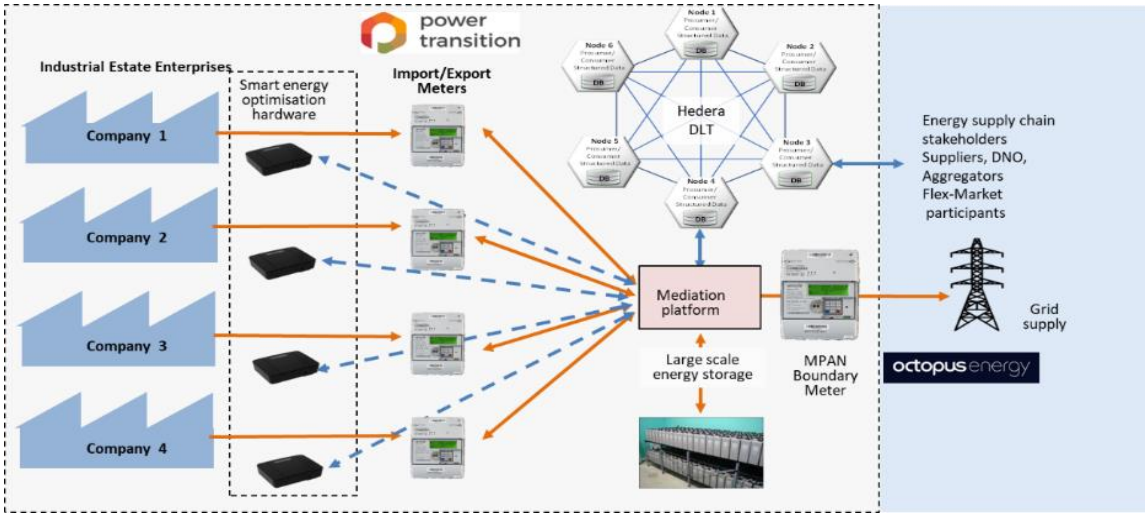

Figure 4 'behind the boundary meter' P2P smart energy trading

has its own operation which is linked to the mediation platform along centralised large scale battery storage. This is equally applicable a university, village or other community such as a school. Indeed, one of our IUK LES projects involved Bristol University which provided an excellent example to study.

Conclusion

The answer to the question posed in the title is "yes." In this paper we have outlined an architecture which has been developed from use cases examined in a number of IUK supported feasibility studies. A UH Digital Twin facility also provides strong opportunities for SPECS and the UH Enterprise Hub to address real-life challenges, working with incubator/accelerator companies and wider business networks as an 'ideas factory.' Digital Twins can mirror smart energy ecosystems developed elsewhere and can be used for experimental validation of different use cases, architectures and solutions. It is recommended that this uses 'air gapped' computing platforms as this provide a safe space to support 'research informed teaching' and problem-based learning.

Reference list

[1] BEIS, "Transitioning to a net zero energy system: Smart Systems and Flexibility Plan 2021.," July 2021. [Online]. https://assets.publishing.service.gov.uk/government/uploads/system/uploads/attachment_data/file/1003778/smart-systems-and-flexibility-plan-2021.pdf. [Accessed February 2022].
[2] Deloitte, "Blockchain: A true disruptor for the energy industry," 2018. [Online]. Available: https://www2.deloitte.com/content/dam/Deloitte/us/Documents/energy-resources/us-blockchain-disruptor-for-energy-industry.pdf. [Accessed 02 July 2019].
[3] W. M, " Distributed ledger technology: beyond blockchain.," December 2015. [Online]. Available: https://assets.publishing.service.gov.uk/government/uploads/system/uploads/attachment_data/file/492972/gs-16-1-distributed-ledger-technology.pdf. [Accessed 07 June 2019].
[4] S. Voshmgir, Token Economy: How Blockchains and Smart Contracts Revolutionize the Economy, Amazon, 2019.
[5] Octopus Energy, [Online]. Available: https://octopus.energy/. [Accessed 21 February 2022].
[6] Innovate UK, "Categories of research and development," 17 August 2021. [Online]. Available: https://www.ukri.org/councils/innovate-uk/guidance-for-applicants/general-guidance/categories-of-research-and-development/. [Accessed 02 February 2022].
[7] O. S. a. T. K. A. Rasheed, " "Digital Twin: Values, Challenges and Enablers From a Modeling Perspective"," *IEEE Access*, vol. 8, pp. 21980-22012, 2020.
[8] L. Rosencrance, "sandbox (software testing and security)," [Online]. Available: https://www.techtarget.com/searchsecurity/definition/sandbox. [Accessed 02 February 2022].
[9] TechCrunch, "Hashgraph wants to give you the benefits of blockchain without the limitations," 14 March 2018. [Online]. Available: https://techcrunch.com/2018/03/13/hashgraph-wants-to-give-you-the-benefits-of-blockchain-without-the-limitations/. [Accessed 2 November 2019].
[10] Ofgem, "Upgrading Our Energy System: Smart Systems and Flexibility Plan," July 2017. [Online]. Available: https://assets.publishing.service.gov.uk/government/uploads/system/uploads/attachment_data/file/633442/upgrading-our-energy-system-july-2017.pdf. [Accessed 14 May 2019].
[11] Department for Business, Energy & Industrial Strategy, "Community Energy," 25 March 2013. [Online]. Available: https://www.gov.uk/guidance/community-energy. [Accessed 14 May 2019].

Session 3. Understand and Expand our Boundaries

chaired by Professor Philip Lucas

University of Hertfordshire UH

Invited Speaker: **The origin of elements and the evolution of galaxies**

Chiaki Kobayashi

Centre for Astrophysics Research, School of Physics, Engineering and Computer Science, University of Hertfordshire, AL10 9AB, UK

When the universe started with the Big Bang 13.8 billion years ago, only light elements such as hydrogen and helium were created. Heavier elements that matter to human beings such as carbon, oxygen, iron, gold, and uranium were instead created inside stars. Computer simulations allow us to predict the complex history of the universe including the formation of stars, the production of elements, the evolution of galaxies, and the growth of super-massive black holes. These theoretical predictions are compared with the latest cutting-edge astronomical observations, such as those from the recently-launched James Webb Telescope.

SCUBA-2 Large eXtragalactic Survey: Constraining the bright-end of the 850um number counts

Tracy Garratt[1*], Kristen Coppin[1], James Geach[1] and Maximilien Franco[1]

[1] Centre for Astrophysics Research, University of Hertfordshire, UK
*corresponding author: t.garratt@herts.ac.uk

The SCUBA-2 Large eXtragalactic Survey of the XMM-LSS field maps an area of 7 deg^2 at a wavelength of 850μm, reaching sensitivities of 1σ~5mJy. The wide area of the S2LXS XMM-LSS survey allows us to probe the ultra-bright, yet elusive submillimetre population, observed only in small numbers (<4) in previous surveys. The S2LXS XMM-LSS observed 850μm number counts show an upturn in the number of sources at bright fluxes. This excess in the number of bright sources is expected to be motivated by local sources of 850μm emission, distant gravitationally lensed galaxies, and sources blended in the single dish beam.

Keywords: extragalactic; submillimetre; starburst; high redshift; number counts

Introduction

In the early 1990s the Far-InfraRed Absolute Spectrophotometer aboard the NASA space-based Cosmic Background Explorer measured the absolute energy spectrum of the Universe at far-infrared (FIR) and submillimetre wavelengths (>150μm). These measurements, taken together with prior observations of nearby galaxies made by the InfraRed Astronomical Satellite in the 1980s, showed that the Universe emits an energy density at FIR and submillimetre wavelengths comparable to that it emits in the ultraviolet and optical regime [1]. This finding indicated that there was likely to be a population of previously undiscovered galaxies, either obscured by dust or with dust enshrouded regions, in which around half of the star formation in the Universe takes place [2]. The FIR/submillimetre emission we observe from these galaxies (now commonly referred to as dusty star-forming galaxies) is produced when ultraviolet emission from young massive stars is absorbed by dust and re-emitted in the FIR. As this light travels through the Universe the wavelength is lengthened (due to the expansion of the Universe), and so for distant galaxies we observe this emission in the submillimetre.

In the two decades since the first discovery of these distant galaxies (known as Submillimetre galaxies) [3,4,5] there has been considerable progress in our understanding of their properties and role as a cosmologically important population in the context of galaxy evolution. Submillimetre galaxies (SMGs) have a number density that peaks at a look back time of 10 Gyr [6,7], are massive [8,9], gas rich [10,11], and form stars at a rate of ~100 – 1000 solar masses per year [12]. Despite the substantial progress in studying the nature of the bulk of the submillimetre population, the bright tail (i.e., galaxies with 850μm flux densities >20mJy) is still poorly understood. This is due to the intrinsic rarity of these ultra-bright SMGs with source abundances currently estimated to be ~0.5-5 galaxies per deg^2[13,14].

Number counts describe the number of galaxies per square degree per observed flux interval. The bright-end of the single dish observed 850μm number counts show an upturn at flux densities >20mJy. This abundance of ultra-bright sources is expected to be strongly influenced by gravitationally lensed galaxies (distant galaxies whose flux has been magnified due to the presence of a massive foreground galaxy or galaxy cluster along the line of sight), source blending (blends of multiple galaxies in the large beam of single-dish surveys), and local sources of submillimetre emission (i.e., planetary nebula) [15]. However, the contribution of each of these sub-populations to the bright-end of the single dish counts is unknown, partly due to biases inherent in targeted surveys (i.e., observations designed to search for lensed galaxies) [16] and partly due to the small number of sources (<4) detected in individual blank-field surveys [14,17,18]. Current galaxy formation models struggle to reproduce the number of ultra-bright SMGs observed [19,20,21,22] despite several including the effects of source blending and/or lensing.

.

SCUBA-2 Large eXtragalactic Survey

The SCUBA-2 Large eXtragalactic Survey (S2LXS) is a James Clerk Maxwell Telescope (JCMT) Large Program and maps an area of ~10 deg^2 at a wavelength of 850μm. This extragalactic survey is the largest of its kind and for the first time provides the surface area needed to detect >10 sources with 850μm flux densities >20mJy. We make use of S2LXS observations of the XMM-LSS field which cover an area of ~7 deg^2 , mapped to a moderate depth of 1σ~5mJy. XMM-LSS is a well-studied field with deep imaging available at ultraviolet, optical, infrared (near – far) and x-ray wavelengths. The wealth of multi-wavelength data available is essential for identifying counterparts to sources detected at 850μm.

The S2LXS XMM-LSS main catalogue is composed of 19 point sources detected at >5σ in the S2LXS XMM-LSS science map. To estimate the number counts we must first correct for incompleteness (the fraction of galaxies in each flux interval that will not be detected at >5σ in the S2LXS map), flux boosting (the flux of galaxies detected at low signal-to-noise is likely to be boosted upwards due to fluctuations in noise), and the false detection rate (the percentage of source detections in a signal-to-noise interval which are likely to be spurious). We use simulated S2LXS XMM-LSS maps and catalogues to estimate these corrections, with a view to uncovering the true underlying source distribution in the XMM-LSS field.

Constraining the 850μm number counts

The S2LXS XMM-LSS 850μm corrected differential and cumulative number counts are presented in Figure 1. In Figure 1 we also plot observational constraints from [14,17,18, 23, 24, 25] for comparison. For the majority of these surveys the brightest sources detected have 850μm flux densities <20mJy (due to the intrinsic rarity of highly luminous objects and the moderate survey areas) and so any comparison is limited, but within the available flux ranges, the S2LXS XMM-LSS results are in good agreement with previous surveys.

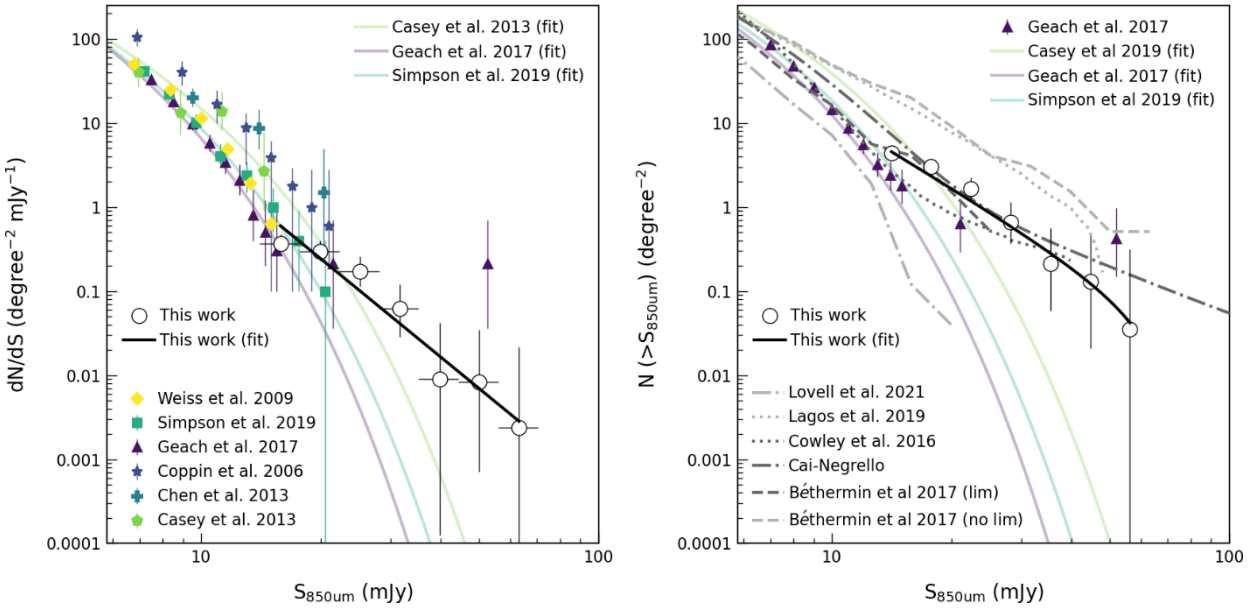

Figure 1. Number counts at 850μm measured from the S2LXS XMM-LSS survey >5σ catalogue (white circles). In the left panel we show the differential number counts from S2LXS XMM-LSS along with observational constraints from several other 850μm surveys (details in text). In the right panel we present the cumulative number counts, comparing to both observations and simulated galaxy models (details in text).

We also show the 850μm number counts from semi-analytic models [20,21], empirical models [19,26,27] and a cosmological hydrodynamical simulation [22]. The results from [20,22] take into account blending from a ~15''

beam (representative of the SCUBA-2 beam full width half maximum). The empirical model of [19] does not take into account source blending but does include a prescription for lensing. The Cai-Negrello model [26,27] combines the counts of unlensed and strongly lensed galaxies. The majority of galaxy formation models shown either significantly under or over estimate the number of observed ultra-bright sources. Only the Cai-Negrello model [26,27] reproduces the excess in the 850μm number counts observed in S2LXS XMM-LSS.

Conclusion

S2LXS XMM-LSS is the largest contiguous area extragalactic survey mapped with the JCMT at 850μm to date. The wide area of the S2LXS XMM-LSS survey allows us to detect ultra-bright, but intrinsically rare submillimetre sources, with the survey detecting 19 sources in total (with 850μm flux densities >18mJy) at a threshold of >5σ. We use the S2LXS XMM-LSS main catalogue to estimate the bright-end of the 850μm number counts, significantly reducing Poisson errors on existing measurements. We observe an upturn in the number counts, expected to be motivated by local galactic objects, sources blending in the single-dish beam and gravitationally lensed distant galaxies. The next step in our research is to determine the relative contribution of each of these sub-populations to the excess in the bright-end of the 850μm number counts.

Reference list

[1] Dole et al. A&A **451,** p417-429 (2006)
[2] Casey et al. Physics Reports **541,** p45-161 (2014)
[3] Smail et al. ApJ **490**, pL5-L8 (1997)
[4] Hughes et al. Nature **394,** p241-247 (1998)
[5] Barger et al. Nature **394,** p248-251 (1998)
[6] Chapman et al. ApJ **622,** p772-796 (2005)
[7] Pope et al. MNRAS **358,** p149-167 (2005)
[8] Swinbank et al. ApJ **617,** p64-80 **(**2004)
[9] Hainline et al. ApJ **740,** p96-120 (2011)
[10] Greve et al. MNRAS **359,** p1165-1183 (2005)
[11] Engel et al. ApJ **724,** p233-243 (2010)
[12] Magnelli et al. A&A **539,** pA155-A190 (2012)
[13] Béthermin et al. ApJL **757,** L23-L30 (2012)
[14] Geach et al. MNRAS **465,** p1789-1806 (2017)
[15] Negrello et al. Science **330,** p800-804 (2010)
[16] Knudsen et al. MNRAS **384,** p1611-1626 (2008)
[17] Coppin et al. MNRAS **372,** p1621-1652 (2006)
[18] Simpson et al. ApJ **880,** p43-64 (2019)
[19] Béthermin et al. A&A **607,** pA89-A111 (2017)
[20] Cowley et al. MNRAS **446,** p1784-1798 (2015)
[21] Lagos et al. MNRAS **489,** p4196-4216 (2019)
[22] Lovelle et al. MNRAS **502,** p772-793 (2021)
[23] Casey et al. MNRAS **436,** p1919-1954 (2013)
[24] Chen et al. ApJ **776,** p131-144 (2013)
[25] Weiss et al. ApJ **707,** p1201-1216 (2009)
[26] Cai et al. ApJ **768,** p21-45 (2013)
[27] Negrello et al. NMRAS **465,** p3558-3580 (2017)

University of Hertfordshire UH

Analysing Spiking Neural Networks Evolved for Temporal Pattern Recognition

Muhammad Yaqoob[1], Volker Steuber[1]

[1]Centre of Computer Science and Informatics Research, University of Hertfordshire, Hatfield, UK

*m.yaqoob3@herts.ac.uk, v.steuber@herts.ac.uk

Spiking activity encodes information in biological neuronal networks and artificial spiking neural networks. This information is processed by transitioning from one spiking behaviour to another due to input stimuli or recurrent activity in the network. Interpreting the mechanism of information processing in spiking neural networks is a fundamental problem in computational neuroscience. In this work, we analyse spiking neural networks evolved for temporal pattern recognition. We demonstrate the functioning of the evolved networks by revealing the role of each neuron in the network. In future, we plan to obtain minimal spiking neural networks for keyword spotting.

Keywords: spiking neural networks, temporal pattern recognition, minimal cognition, artificial evolution. neural circuits

Introduction

Understanding how temporal signals are processed by spiking neural networks (SNNs) is of great interest to the neuroscience community. Several studies have shown that information processing in the nervous systems is linked to the transition from one spiking behaviour to another. However, despite the extensive research, the relationship between the structural connectivity and functional behaviour of neural systems remains unclear. To explain information processing in SNNs, we have evolved minimal networks to perform pattern recognition with biologically meaningful neurons in the presence of noise. We have shown previously that networks evolved in a noiseless environment are highly fragile to disturbed network parameters or a slight variation in input timing. Therefore, understanding the properties of spiking networks evolved in the presence of noise, inspired by biology, is necessary to reveal the driving mechanisms of neural circuits.

Experimental Setup

A network recognising a pattern of three signals consists of three input nodes (each signal is assigned one node), three interneurons and one output neuron. The interneurons are of type adaptive exponential integrate and fire AdEx [2], defined by four state variables (membrane potential V, adaptation w, excitatory g_E and inhibitory conductance g_I). Noise is modelled as adding a random value drawn from the normal distribution centred at 0 with a standard deviation of 2 mV to membrane potential V at each network step. Interneurons can form self-loops, and inputs are not allowed to connect to the output neuron directly. A neuron can excite or inhibit other neurons at the same time. During evolution, each network is presented with a continuous random sequence of signals A, B and C as input (say BACCABCAABBABBC…). These signals are encoded as intervals of time. A signal is of length 6 ms followed by a silent interval of 16 ms. The task of the network is to respond with at least one spike in the silent interval after ABC is received.

Each independent evolutionary run had 300 individuals. The initial generation is created by generating random genomes coding for three inter-neurons. The length of genomes in the population is variable such that each region coding for a single neuron had an arbitrary number of dendrites and axon terminals. Subsequent generations are created with binary tournament selection. After winning the tournament, an individual undergoes three genetic operators; (i) one point mutation, (ii) duplication, and (iii) deletion. The fitness function rewards spiking of the output neuron after receiving signals in the correct order (ABC) and penalises spike(s) elsewhere.

Results and discussion

The structural similarities among networks obtained from different independent evolutionary runs greatly helped in understanding the properties of SNNs. A successful network that can maintain memory requires at least (n-1) self-excitatory loops with sufficient weight to sustain indefinite spiking activity [3], where n is the number of interneurons in the network. The number of interneurons grows linearly with the length of the pattern to be recognised, while the number of connections (k) grows quadratically by function $K = n^2 + 2$. For example, identifying a pattern of two signals requires 6 connections (Fig. 1a), and a pattern of three signals requires 11 conections (Fig. 1b). All perfect recogniser networks share a mechanism of strongly inhibiting (locking) the output neuron from spiking, preventing it from spiking in response to wrong patterns. The lock is only released by the second to the last correct input signal (maintained passively by no activity in the network), allowing the output neuron to spike in response to the last correct signal.

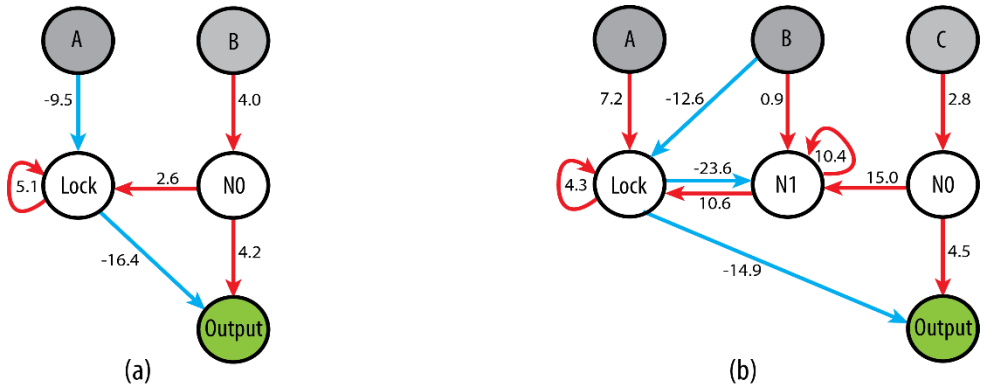

Figure 1. Topology of the minimal networks: The red and blue lines represent excitatory/inhibitory connections. The number next to each line is the amount of conductance the postsynaptic neuron receives when a presynaptic neuron spikes. (a) The minimal network for recognising two signals. The output neuron spikes only for input signal AB. The lock neuron prevents the output from spiking for other permutations (AA, BB, BA). (b) The minimal network for recognising three signals. Here, the output neuron only spikes for ABC, while the lock neuron prevents the output from spiking for all other 26 permutations (AAA … CCC).

Conclusion

We found that the spiking networks recognising temporal patterns obtained from independent runs are either equal or isomorphic. Moreover, the presence of the lock neuron in all perfect recognisers and maintenance of the penultimate state by no activity in the network is intriguing. In future work, we plan to investigate it further by modifying the evolutionary algorithm to search for other possible topologies. A different evolutionary algorithm might produce different classes of solutions. Another possible direction of future work is the evolution of networks for more complex tasks involving temporal pattern recognition.

Reference list

[1]. Huxter, J., Burgess, N., and O'Keefe, J.: (2003). Independent rate and temporal coding in hippocampal pyramidal cells. Nature, 425:828–832.

[2]. Naud, R., Marcille, N., Clopath, C., Gerstner, W.: Firing patterns in the adaptive exponential integrate-and-fire model. Biol. Cybern. 99, 335–347 (2008)

[3]. Yaqoob, M., Wróbel, B.: (2018). Robust very small spiking neural networks evolved with noise to recognise temporal patterns. ALIFE 2018: Proceedings of the 2018 Conference on Artificial Life - MIT Press, pp. 665–672.

[4]. Yaqoob, M., Steuber, V., Wróbel, B.: (2019). The Importance of Self-excitation in Spiking Neural Networks Evolved to Recognise Temporal Patterns. In: Artificial Neural Networks and Machine Learning - ICANN, pp. 758-771.

University of Hertfordshire UH

Invited Speaker: **Topology - a new lens into the brain**

Shabnam Kadir

Centre of Computer Science and Informatics Research, School of Physics, Engineering and Computer Science, University of Hertfordshire, Hatfield, UK

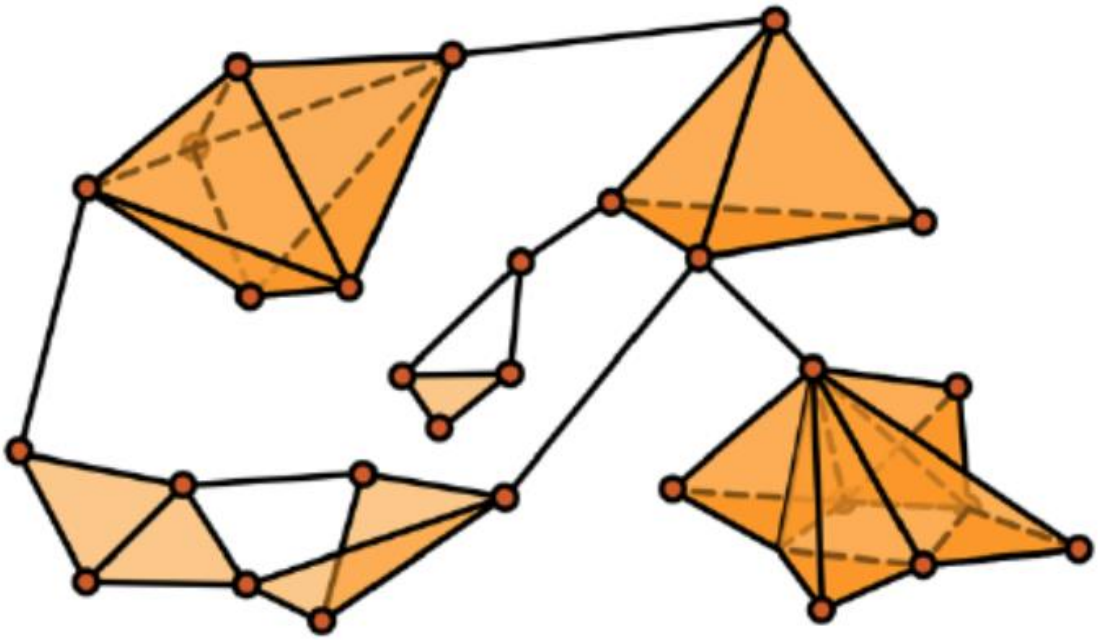

Picture by E. Dmitruk

Poster Sessions

University of Hertfordshire UH

Antimicrobial Evaluations of Metallic Nanoparticles

Etelka Chung[1*], Yuen-Ki Cheong[1], Ian Johnston[1] Mansukhlal Vadalia[2], Andrew Timms[2] and Guogang Ren[1]

[1]School of Physics, Engineering and Computer Science, University of Hertfordshire, AL10 9AB
[2]School of Life and Medical Sciences, University of Hertfordshire, AL10 9AB
*corresponding author: ec16acn@herts.ac.uk

Infectious pathogens have been issued a high warning from World Health Organisation for new antibiotics due to resistance. Metallic nanoparticles are known to exhibit antimicrobial activity thus 20 nanoparticles were investigated. AgCu nanoparticles were found to contain the highest efficacy against *S. typhimurium* and *E. faecium* using the cut well method. The nanoparticles were observed on the SEM and found that AgCu nanoparticles were smaller in size. However further characterisation including surface charge and hydrodynamic, will be performed on the nanoparticles to better understand the influence on antimicrobial activity.

Keywords: Metallic nanoparticles, antimicrobial resistance, bacteria, infection

Introduction

Nanoparticles, with sizes typically less than 100 nm, have shown antimicrobial activity against pathogens and for this reason are being adopted in medical applications [1]. Currently, antimicrobial resistance of pathogens is a major global issue and the antimicrobial efficacy of nanoparticles may provide an alternative solution to address these challenges [2, 3]. In this study, engineered Metallic Nanoparticles (MNPs) along with several other manufactured nanomaterials such as graphene based and oxides were screened for antimicrobial activity against Gram negative *Salmonella typhimurium* and Gram positive *Enterococcus faecium*. These common infectious pathogens can lead to meningitis and bacteraemia and with a high priority warning from World Health Organisation for new antibiotics due to resistance, antimicrobial nanoparticles could be a possible answer [2, 4].

Experimental

Nanoparticles (NPs) and biological cultures were provided by the Antimicrobial@UH consortium and UH microorganism collection, respectively. The Cut well method (4mm wells) was used to identify zone of inhibition of antimicrobial NPs against bacteria. Agar plates inoculated with bacterial colonies were incubated in the presence of freshly dispersed NPs suspension (1000 ppm) at 37 °C for 24 hours. Clear rings were identified and diameters were measured in cm. Nanoparticles were observed on the SEM (JEOL, UK) at 20kV at x6,000 magnification.

Results and discussion

Over 20 different NPs were tested. These included elemental Ag, Cu, metal oxides (CuO & ZnO), intermetallic alloys (AgCu & CuZn) and engineered MNP formulations (AVNPs). Overall, intermetallic silver copper (AgCu) nanoparticles were found to have the highest levels of antimicrobial activity against both *S. typhimurium* and *E. faecium*, with average inhibition diameters of 1.6 cm and 1.4 cm respectively (Fig. 1). SEM images (Fig. 2a & 1b) showed that the AgCu particle sizes appear to be smaller than those of Ag. This may result in increased exposure opportunities and physical interactions with microbial colonies; resulting in the enhanced antimicrobial activity observed in AgCu NPs. To better understand the physiochemical behaviour of these active antimicrobial NPs within biological environments, their hydrodynamic properties (sizes & surface charges) will be further investigated using technologies such as Dynamic Light Scattering (DLS), Nanoparticle Tracking Analyzer (NTA) and Zetasizer.

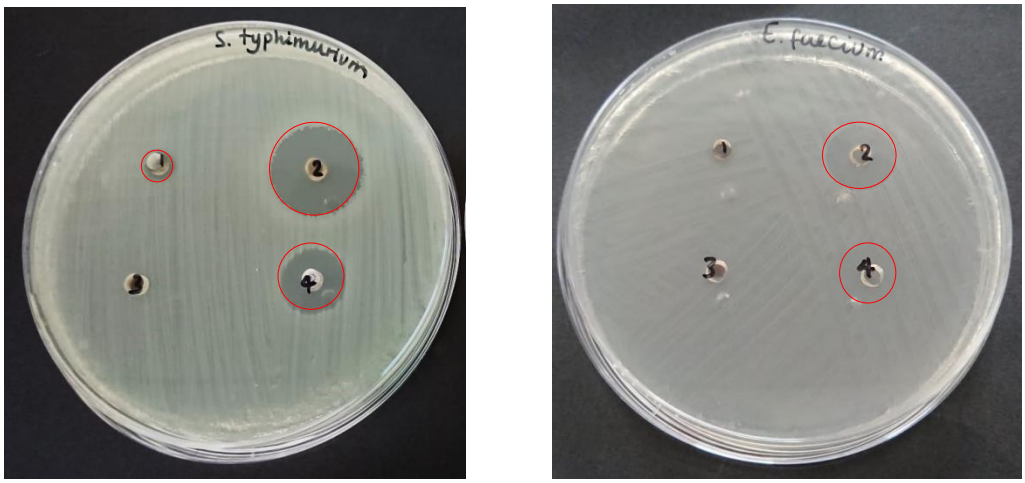

Figure 1. Cut well agar of of S. typhimurium (left) and E. faecium (right) with inhibitory zones circled in red

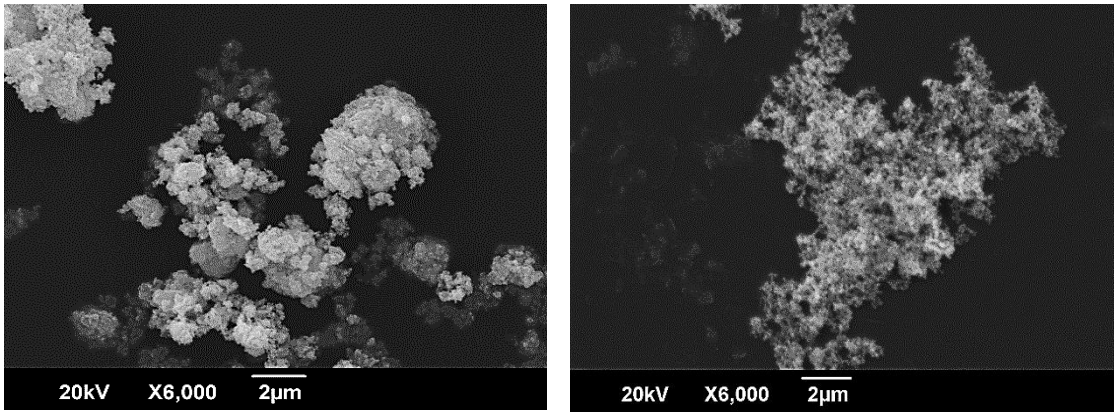

Figure 2. SEM images of Ag nanoparticles (left) and AgCu nanoparticles (right)

Conclusion

Common pathogens such as *S. typhimurium* and *E. faecium* are an infectious threat as a result of their antibiotic resistance. A possible solution may be metallic nanoparticles as they were found to exhibit antimicrobial activity with AgCu nanoparticles having the highest activity against *S. typhimurium* and *E. faecium* as investigated with the cut well method. SEM imaging has shown that the AgCu nanoparticles looked smaller in comparison to Ag nanoparticles, which may have contributed to their enhanced antimicrobial activity. Further research is required to characterize the nanoparticles and understand their behavior and influence on antimicrobial activity.

Reference list

1. Fernando, S., Gunasekara, T. and Holton, J., *Antimicrobial nanoparticles: applications and mechanisms of action.* Sri Lankan Journal of Infectious diseases, 2018. **8**(1): p. 2-11.
2. Kopit, L.M., et al., *Safety of the Surrogate Microorganism Enterococcus faecium NRRL B-2354 for Use in Thermal Process Validation.* Applied and Environmental Microbiology, 2014. **80**(6): p. 1899-1909.
3. Singh, P., et al., *Antimicrobial Effects of Biogenic Nanoparticles.* Nanomaterials (Basel, Switzerland), 2018. **8**(12): p. 1009.

University of Hertfordshire UH

Bacterial colony counting could be rapid, adaptive and automated

Minghua Zheng[1*], Na Helian[1], Peter Lane[1], Yi Sun[1] and Allen Donald[2]

[1]University of Hertfordshire
[2]Synoptics Ltd
*corresponding author: m.zheng2@herts.ac.uk

Although many attempts have been made to automate bacterial colony counting, little has tackled the counting of clustered colonies and adaptations to handle different bacteria species. In this work, we explore the counting by density estimation method via few-shot learning. We have avoided the difficult localisation and detection of clustered colonies by estimating a density map from the input image. We have also exploited exemplars provided by users to make the method agnostic and adaptive to different bacteria species. Our experiments show that using the counting by density estimation method via few-shot learning results in a promising accuracy from the data set provided by Synoptics Ltd.

Keywords: Bacterial colony counting, automation, clustered colonies, density estimation, few-shot learning

Introduction

Counting the number of colonies on an agar plate is a widely used technique in both industry and research laboratories to estimate the number of viable bacteria (total viable count) present in a test sample in a wide range of applications; these include quality control, environmental monitoring, immunological studies and medical testing. The number of colonies can be used as an important indicator of the cleanliness of a surface, the sterility of a product or the present of a bacterial infection.

Traditionally, bacterial colony counting is performed manually, which is time-consuming and prone to human error [1]. Many attempts have been made to automate it with traditional image processing methods or machine learning algorithms. But they are designed specifically for certain bacteria species without identifying and counting clustered colonies where a group of colonies are close together, touching and overlapping. This research aims to address this research gap. We investigate the impact of counting by density estimation via few-shot learning on clustered colonies and its adaptations to handle different bacteria species. The difficult localisation and detection of clustered colonies are avoided by estimating a density map where the sum of values indicates the colony count. The counting algorithm only learns from three exemplars (examples of the target colony) provided by users in the few-shot learning fashion so that it is adaptable to different bacteria species.

Methodology

FamNet [2] is used in this work due to its outstanding ability to count many different types of object. As shown in Figure 1, users are required to provide three exemplars by drawing three bounding boxes in the input plate image. These three exemplars are the support set. The plate image is the actual query image. FamNet consists of a multi-scale feature extraction module and density map estimation module.

The first module is ResNet-50 [3] whose parameters are frozen during both training and inference phase so that it only acts as a feature extractor. It takes the query image as input and returns two feature maps from the third block and fourth block in ResNet-50 respectively. Features inside the region of interest (ROI), which is the exemplar specified by the bounding box, in the feature map are used to convolve the two feature maps to form two new feature maps which are later concatenated into a new feature map. The former is called ROI pooling and the latter is called feature correlation. To recognise similar colonies at different scales, the ROI pooling and feature correlation are repeated with the three exemplars rescaled at 0.9 and 1.2. The two new resulting feature maps are concatenated with the previous feature map to form a final feature map.

The density map estimation module is a regression model that uses the correlated feature map to predict a density map. It consists of five convolutional layers where the first, second and third convolutional layer is followed by an upsampling layer. The fifth convolutional layer is convolved by 1 x 1 kernel to predict the density map whose shape is the same as that of the input image. The kernel parameters for the five convolutional layers

are 7 × 7 × 196, 5 × 5 × 128, 3 ×3 ×64, 1 × 1 × 32 and 1 × 1 × 1 respectively. The Rectified Linear Unit (ReLU) is used as activation function in each convolutional layer.

The data set used in this work is a collection of 128 plate images provided by Synoptics Ltd. The resolution of each plate image is 3 x 1040 x 1040. The ground truth annotations contain density maps and coordinates of the three bounding boxes. Exemplars specified by the bounding box have a different colony species based on different images in the data set. The whole data set is divided into training set, validation set and test set with a ratio of 6:2:2. The training method is the same as used in [2]. The optimiser is Adam. The learning rate is 10^{-5}. Batch size is 1. Epoch number is 1500. The loss function is mean square error. However, the adaption loss used in [2] is not included in this work because it has been proven ineffective based on our experiments. The results are measured by mean absolute error (MAE) and root mean square error (RMSE).

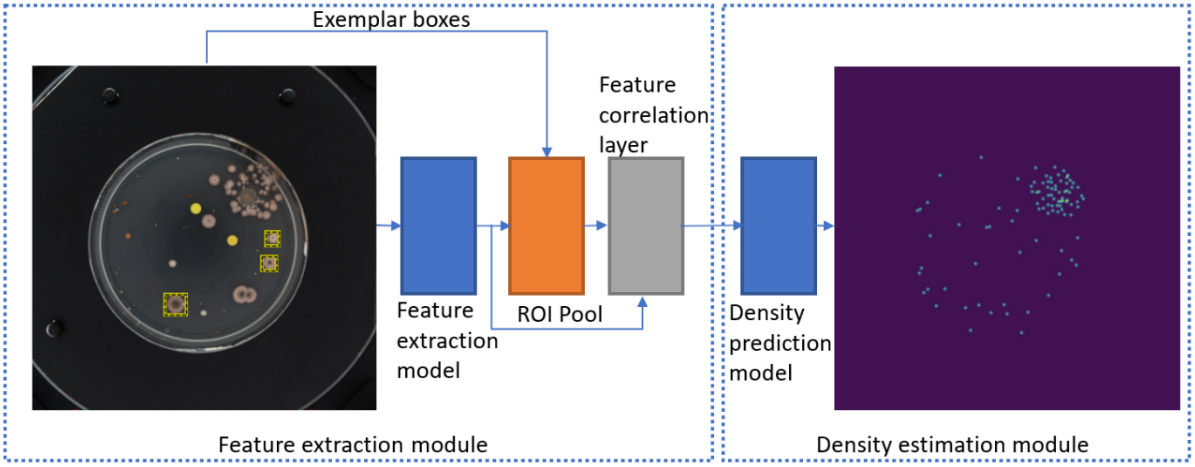

Figure 5: FamNet takes the query image (plate image) as input along with three bounding boxes representing the target colony and predicts a density map. The support set is the three exemplars provided by the bounding boxes. The colony count is obtained by summing all density (pixel) values in the predicted density map.

Table 1: Prediction results.

	MAE	RMSE
Training set	24.01	32.95
Validation set	16.34	20.65
Test set	29.80	39.75

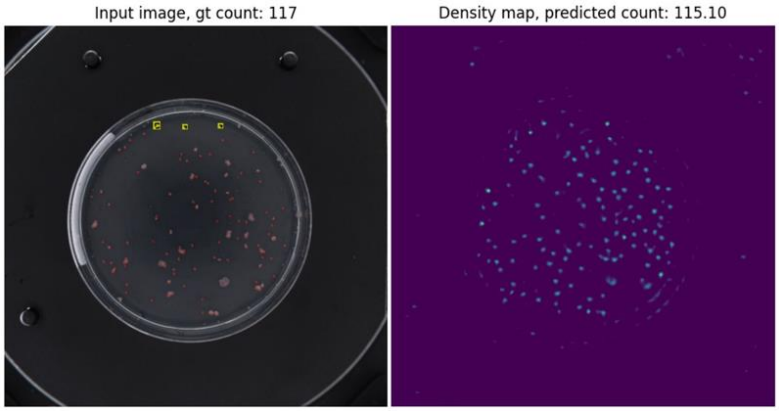

Figure 6: Predicted density map.

Results and discussion

As shown in Table 1, FamNet achieves 29.80 in MAE and 39.75 in RMSE on the test set. It has not shown the sign of overfitting because the results from the test set are close to the results from the training set despite that FamNet performs better on the validation set. FamNet can predict 115.1 colonies from a plate image that has 117 colonies as shown in Figure 2. FamNet is also able to handle different colony species because it can learn from the three exemplars. The predicted density map also contains spatial information of colonies. The time used to make a single prediction is less than a second because images are batched and the computation is shared.

Conclusion

We have investigated the impact of density estimation via few-shot learning on the clustered colonies and its adaptations to handle different colony species. The FamNet used in this work achieves 29.80 in MAE and 39.75 in RMSE on the test set. Our experimental results show this method is adaptive to different colony species because of the user-specified exemplars. In a real-world application, these three exemplars can be stored in the system and reused for other data to ensure a high level of automation. The experimental results also show the prediction is very rapid because plate images are batched and the computation is shared. However, there are still rooms to improve the prediction results by fine tuning the model or modifying the design of two modules in FamNet. Future work also concerns a deeper analysis of the counting error and FamNet.

Reference list

[1] Brugger, S. D. et al. (2012). Automated Counting of Bacterial Colony Forming Units on Agar Plates, *PLoS ONE 7(3)*, e33695.
[2] He, K., Zhang, X., Ren, S., and Sun, J. (2015). Deep Residual Learning for Image Recognition. *2016 IEEE Conference on Computer Vision and Pattern Recognition (CVPR)*, 2016-Decem, 770–778.
[3] Ranjan, V. et al. (2021). Learning To Count Everything. *2021 IEEE/CVF Conference on Computer Vision and Pattern Recognition (CVPR)*, 3393.

CFD investigation of aerofoil design effects on dynamic stall characteristics

Lewis, A.[1], Samararatne, S.[2]*

[1]Senior Lecturer, University of Hertfordshire

[2]Research Student, University of Hertfordshire

*corresponding author: samadhi.samararatne@gmail.com (Calibri, 12 pt)

The focus of this research is to use existing Computational Fluid Dynamics (CFD) methods, namely the software package Star CCM+, to model and observe effects of various aerofoil design features on dynamic stall. An overset mesh is used to model 2D, transient simulations of aerofoils undergoing dynamic stall.

Keywords: Dynamic Stall; CFD; Chimera Mesh; Overset Mesh; Transient Simulation

Introduction

Dynamic stall is a complex aerodynamic phenomenon that manifests itself on aerofoils undergoing rapid oscillatory movement, taking it into the natural stall regime. This phenomenon is primarily observed on the blades of helicopter rotors, although it has also been noted on wind turbine blades, flapping and morphing wing flyers, highly manoeuvrable aircraft, and missiles. As the incidence angle of an oscillating aerofoil surpasses the static stall limit, flow reversal starts to occur inside the boundary layer, eventually resulting in a leading edge vortex which initially results in an increase of lift, but then goes on to create a pitching moment near the leading edge of the aerofoil. This effect creates stress that an aerofoil would not see under static conditions and changes the normal static aerodynamic characteristics of the aerofoil.[1] There is a hysteresis effect as well where the flow reattaches at a much shallower angle than the angle at which the flow starts to separate.[2] Dynamic stall can have negative consequences on wings and rotor blades in some applications as it can create excessive unsteady forces and moments, leading to stress and failure, but may be beneficial if controlled on some applications as well.

There have been a number of research papers in the recent past which have explored various methods of controlling dynamic stall through changing different design aspects of an aerofoil. A thorough literature search has revealed that the leading edge of the aerofoil plays a key role in the dynamic stall characteristics and therefore, introducing things like a blunt leading edge[3] or leading edge tubercles[4] are effective at negating some of the dynamic stall build-up.

The focus of this research is to use existing Computational Fluid Dynamics (CFD) methods, namely the software package star CCM+, to model and observe effects of various aerofoil design features on dynamic stall. Although large amounts of research have been done on this topic, it remains an active research subject due to the complexity of the phenomenon, the difficulty of modelling it using CFD and the varied applications in which it arises. This research aims to recommend a set of best practices to use when modelling dynamic stall on CFD. It also aims to highlight aerofoil design features that affect dynamic stall the most, and figure out which features are best to alter in order to achieve desired dynamic stall characteristics. It will also serve as a compilation of the most efficient methods of controlling dynamic stall from literature. New methods of controlling dynamic stall are also being explored through this research.

Experimental

To simulate an oscillating aerofoil using Star CCM+, the aerofoil has to move in relation to the background. This is achieved by the use of something called Chimera or Overset meshing, which is a method of using several independent meshes to break up the flow domain. What happens when using this method is that the overset mesh is simply superimposed on top of the background mesh and a hole cutting algorithm is used to create a space in the background mesh. This hole is created at the beginning of each time step to account for the movement of the overset mesh. Information is passed between the two regions through overlapping cells. Cells in the overlapping zone should be of comparable size in both meshes, which can be managed by using volumetric

controls. For each active cell at the edge of one mesh, exists an adjacent acceptor cell. For each acceptor cell, there are three donor cells (in 2D) or four (in 3D) in the other mesh that are used to determine the contribution of the acceptor cell. Linear interpolation using shape functions are then used to weight the value of those cells to determine the cell centre value for the acceptor cell. Between two body walls, at least 4 cells on both background and overset mesh are needed to couple them, and it is recommended that the overset mesh should not move more than one cell per time step in the overlapping zone. [5]

Two volumetric mesh regions are created using a trimmer mesh for the aerofoil and the background, and then converted into 2D. The two separate mesh regions are necessary for the overset mesh to operate. The trimmer mesh model was chosen as it provides the most accurate results for external aerodynamics. A prism layer was also applied around the aerofoil in order to more accurately model the boundary layers. Several volumetric controls were added on and around the aerofoil to make the mesh finer on desired areas such as the leading edge and trailing edge. It was also important to make sure that mesh at the overlapping areas between the aerofoil region and the background region was the same, and volumetric controls were used to achieve this as well. An inlet and outlet boundary condition was chosen to better emulate the conditions in a wind tunnel, as was the real equilibrium air physics model. Emulating wind tunnel conditions was important as the simulation results would be compared against wind tunnel experiment results found in literature. An appropriate timestep was chosen considering the condition that the overset mesh can only move one cell per timestep. This was the limiting condition as this needed a lower timestep than the courant number demanded. The K-Omega SST turbulence model was chosen along with the Gamma Re-Theta transition model. A sinusoidal motion was imparted on to the aerofoil through overset mesh by prescribing a new rotational motion. The equation for the rotational rate was found by differentiating the equation that described the motion of the aerofoil. This setup was refined over a period of time and validated using experimental results available in literature.

A NACA 0012 aerofoil was used for most of the simulations as this seemed to be a popular aerofoil for dynamic stall experiments in the past and therefore had the most amount of experimental data available. [6]

Results and discussion

The CFD simulations have shown good correlation to experimental results available in literature, as seen in *Fig. 1*. A NACA 0012 aerofoil with a blunt leading edge is being experimented with as is a version with leading edge tubercles. These modifications have a significant effect on the dynamic stall characteristics but further improvements are needed in order to achieve the desired effects.

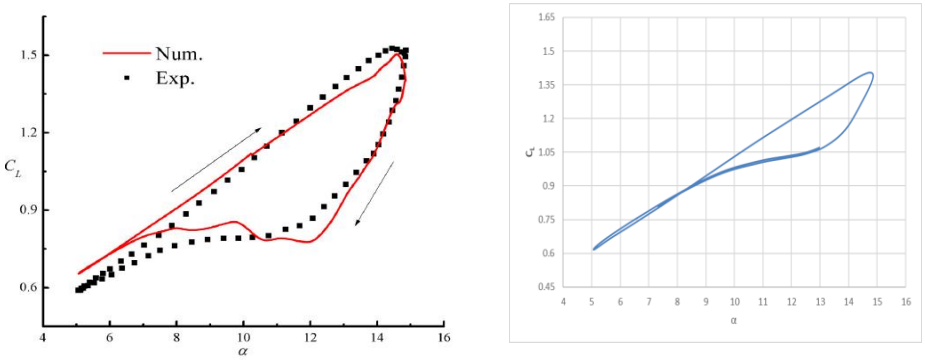

Fig. 1 - Experimental results vs. CFD results.

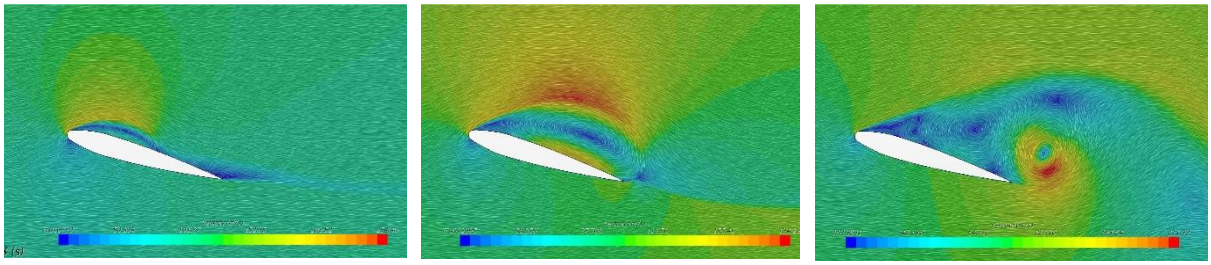

Fig. 2 – Flow visualisation of a modified NACA 0012 aerofoil undergoing dynamic stall, modelled using CFD.

Conclusion

The CFD modelling methods have been refined and the results from simulations have provided good correlation with results from experiments in literature. A set of best practices for modelling dynamic stall through CFD can now be recommended. The conditions that make the biggest difference on dynamic stall results in CFD have been identified to be the mesh, the boundary conditions, the turbulence solver and the timestep. The dynamic stall control methods that have been tested so far have shown promise, but they need more refinement in order to achieve the desired effects.

Ice accretion and erosion on aerofoils have been much researched with regard to their effect on the lift, drag and pitching moment of the static aerofoil but little to no studies have been done on their effect on dynamic stall, especially in the case of ice accretion. This is a gap in research that is ripe to be explored.

3D effects of dynamic stall – spanwise flow has shown to be effective in controlling dynamic stall vortices on insect wings[7] – have been scarcely explored using CFD methods. Whilst it is outside the scope of this research due to the computational time and demand it would take to run such simulations, it appears to be an interesting area of exploration.

Reference list

[1]Hu, H. *et al.* (2007) Journal of Aircraft **44**(6) 2083-2086.

[2] Corke, T.C. *et al*. (2015) Review of Fluid Mechanics **47**(1) 479-505.

[3] Quing, W. *et al.* (2015) Chinese Journal of Aeronautics **28**(2) 346-356

[4]Aftab. S.M.A *et al.* (2017) PLOS ONE **12**(11) e0188792

[5]Enger, S. (2014) Overset Mesh in STAR-CCM+. CD Adapco

[6] Mcroskey, W.J.*et al.* (1976). AIAA Journal **14**(1), 57-63

[7] Sun,M *et al.* (2002) Journal of Experimental Biology **27**(7) 55-70

University of Hertfordshire UH

Development of a Bespoke Hybrid Regression-based Technique for Diesel Engine Optimisation

Laurel Asimiea[1]*, Mohammad Reza Herfatmanesh[1]

[1]School of Physics, Engineering, and Computer Science, University of Hertfordshire, College Lane, Hatfield AL10 9AB, United Kingdom

*Laurel Asimiea: laurel.laurenzo@yahoo.com

Abstract: The Hybrid Regression-based Technique is introduced as a bespoke optimisation technique which can be applied to the optimisation of diesel engines to provide accurate optimal design solutions with a considerably reduced computational cost and time. In this work, its implementation results in strong comparison to the validation data and improvements to in-cylinder NOx and Soot emissions with marginally losses to in-cylinder engine performance considering 655 designs which required a computational time of 145 hours.

Keywords: Diesel Engine; Double Fuel Injection Strategy; Hybrid Regression-based Technique (HRT); Optimisation; Heterogenous design dataset

Introduction

The development of cleaner and more efficient diesel engines still gathers interest despite stringent emission regulations and calls for the ban on new internal combustion engines in the UK. One driver for advanced diesel engines is their application in hybrid powertrains pending the economical maturation of sustainable powertrains such as fully electric powertrains [1],[2],[3],[4].

Computational optimisation is a cornerstone to the development of advanced engines. Various investigations have also reported on the simultaneous improvements gained for engine parameters such as in-cylinder Indicated Mean Effective Pressure (IMEP), NOx and Soot [5]. Despite the gains achieved through computational optimisation, some challenges such as the approach towards the consideration controllable and fixed engine parameters, as well as the computational time and cost required by such studies pose a hinderance to its further application. These limitations become more obvious when 3D CFD solvers and global optimisers such as the well-known Multi-Objective Genetic Algorithm-II (MOGA-II) are involved. It is clear that the application of computational optimisation for engine development can only improve in feasibility through the exploration of new techniques by which such studies incur lesser computational cost and time while considering more engine parameters. In this work, a bespoke optimisation approach referred to as the Hybrid Regression-based Technique (HRT) is proposed for diesel engine optimisation. In the following sections, its methodology as well as the preliminary results from its implementation and conclusions shall be briefly discussed.

Methodology

The uniqueness of the HRT lies in the respective features of its three phases which include the generation of the design dataset, the process of regression modelling using the design dataset and the formulation of the predictive model as seen in Figure 1. The HRT features a heterogenous design dataset approach for its design dataset generation dissimilar to the homogenous approach currently used in the various studies. The heterogenous design dataset provides a design space with the capability of effective design exploration and more importantly, an earlier indication of the design pareto front due to its unique features. This characteristic permits the use of relatively smaller design dataset sizes and effectively reduces the computational cost and time required for 3D CFD generated designs for the dataset.

The regression modelling phase of the HRT features the application and consideration of multiple regression methods during training and validation whilst utilising a dataset random partitioning. This approach is in contrast to current methodologies wherein a single regression method is considered. During the regression modelling process, the predictors are the interesting design parameters whereas each of the considered output parameters which constitute the multi-objective function of the optimisation is used as a response. The regression modelling process is performed such that regression models are generated against each output parameter considered. Here, a regression model for an output parameter response may come from the same or different regression method compared to the model for another output parameter response. Finally, each

output parameter has a generated regression model that best predicts its response. The formulation of the predictive model involves the amalgamation of the selected regression models for each response into a hybrid form. Finally, a global optimiser algorithm is then used to govern this hybrid predictive model to generate predictions towards optimal solutions for all considered output parameters simultaneously in accordance with the predefined multi-objective function.

Results from the demonstration of the HRT

The HRT and its methodology were applied in the optimisation of a 3D CFD engine model that was validated using a single cylinder Ricardo Hydra diesel engine running at low load. The optimisation process was focused on the simultaneous reduction of in-cylinder NOx and soot emissions while either maintaining or improving in-cylinder IMEP and reducing indicated Specific Fuel Consumption (ISFC). The parameters of the double injection strategy for the engine were the considered design parameters and predictors. The HRT involved a total of 20 3D CFD simulated designs and 635 regression-based generated designs. The generation of the regression-based predictions was observed to be fast and comparable to similar studies which have featured regression-based optimisation. However, the gain in computational time and cost was obtained in the generation of the CFD designs which was significantly lower compared to similar investigations. The total number of designs generated required about 145 hours on a 32GB RAM computer workstation which when compared to similar studies which utilised a larger design dataset was lower by about 70%. Three pareto optimal designs were selected from the pool of generated designs and analysed. The first two pareto designs were found to be part of the 3D CFD designs from the heterogenous design dataset which indicated that the approach was effective in improving regression learning as well as finding optimal solutions early the optimisation process. The third design was a regression-based generated design and thus, was validated using the 3D CFD engine model. Its validation result showed a marginal (i.e., <1%) deviation in engine in-cylinder IMEP, ISFC and soot as well as a 6% deviation in NOx. A comparison of the three designs against the CFD baseline showed about 6% and 19% reduction in NOx and soot emissions, respectively, with marginal losses in performance.

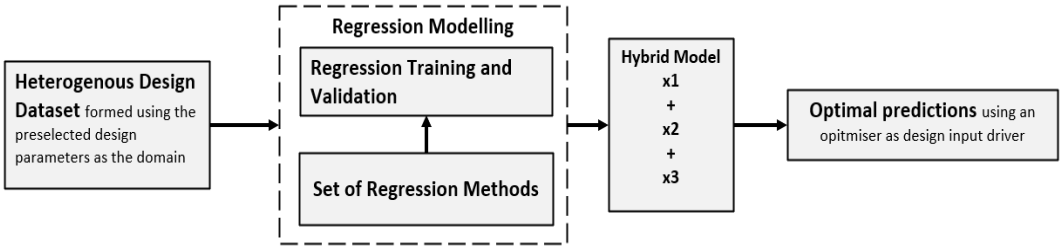

Figure 1. Simplified workflow of the HRT

Conclusion

In this work, the HRT was introduced and applied to the optimisation of a 3D CFD engine model to simultaneously reduce in-cylinder NOx and Soot emissions while either maintaining or improving IMEP and ISFC at low load. The results showed that features such as the heterogenous design dataset were effective for regression modelling as well as obtaining pareto optimal design solutions. Low deviations were observed between the regression prediction and respective CFD validation. Despite marginal losses in in-cylinder IMEP and ISFC of <1%, considerable improvements to NOx and soot emissions were also observed. The application of the HRT showed that it could provide accurate optimal predictions for reduced engine emissions and similar performance with a significantly lower computational cost and time compared to similar investigations.

Reference

[1] Motlagh T, Azadani L, Yazdani K, Applied Energy **279**, p. 1-15 (2020).
[2] Hu N, Zhou P, Yang J, Energy Conversion and Management **133**, p.138-152 (2017).
[3] Lotfan S, Ghiasi R, Fallah M, Sadeghi M, Applied Energy **175**, p. 91-99 (2016).
[4] Zexian G, Xin H, Yuanjiang P, Chen-Teng C, Peng W, Xingyu S, Boyuan W, Shiyu L, Zhi W, Shijin S, SAE Technical Paper 2020-01-2056 p. 18 (2020).
[5] Shi Y, Ge H, Reitz R, Springer London DOI: 10.1007/978-0-85729-619-1 p. 15-145 (2011).

University of Hertfordshire UH

Identifying Analogous State Types Across Simultaneously Recorded EEG-fMRI

David G. Haydock[1]

[1]*University of Hertfordshire*

Keywords: Neuroimaging, Cognitive Science, Applied Mathematics

Electroencephalography (EEG) is a well-known neuroimaging technique [1]. Studies to characterise EEG microstates; sets of transient, quasi-stable topographical scalp maps (Fig. 1a) [2], have been applied to the domain of sequence analysis in recent years. Patterns in microstate sequences (Fig. 1b) have shown meaningful relations to neurological disorders [3], psychopathologies [4], mental states [5], and personality differences [6]. Whilst observed patterns of EEG microstates capture neural spatiotemporal dynamics at the scalp, the source of these patterns within the brain and their functional significance in terms of cognitive processes/mental states remains elusive [7]. Functional magnetic resonance imaging (fMRI) has been used in conjunction with EEG in an attempt to localise the sources of EEG microstates in the brain [8], but no previous study has attempted to apply sequence analysis of fMRI states to this problem (Fig. 1c). Here, we take the first steps towards simultaneous EEG-fMRI sequence analysis by identifying complementary state types in each recording medium (Fig. 1b, d), with a future goal of applying the generated sequences to analysis that will elucidate the correlation of brain function to EEG microstates.

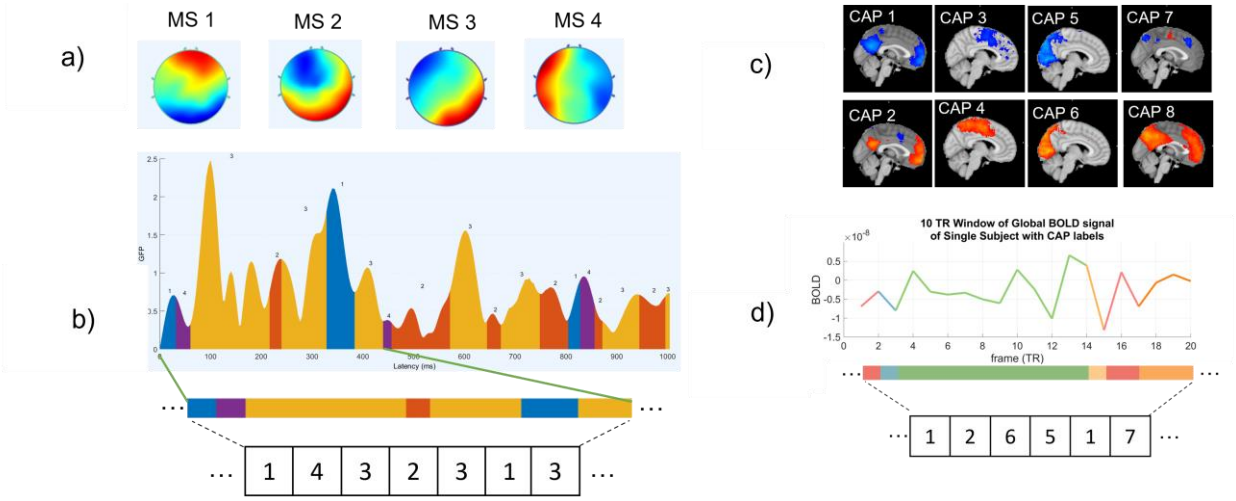

Fig. 1 – (a) Using K-means clustering of global field power (GFP) peak scalp map topographies from EEG generates a set of stable EEG microstates. (b) We subsequently 'back-fit' these states onto the original EEG times series based on a similarity measure, to generate a sequence of microstates across the time series. (c) A similar clustering approach in the time series of fMRI generates an even set of fMRI states referred to as 'co-activation patterns' (CAPs). (d) TRs are subsequently labelled with their CAP for application to sequence analysis.

References

[1] Tudor, M. *et al.* (2005). Acta Medica Croatica: Casopis Hravatske Akademije Medicinskih Znanosti **59**(4), 307

[2] Lehmann, D. (1987). Handbook of electroencephalography and clinical neurophysiology : Methods of analysis of brain electrical and magnetic signals **1**. Publisher: Elsevier, 309

[3] Pal, A. *et al.* (1st June 2021). Cognitive Neurodynamics **15**(3), 463

[4] Lehmann, D. *et al.* (Feb. 2005). Psychiatry Research: Neuroimaging **138**(2), 141

[5] Brodbeck, V. *et al.* (Sept. 2012). NeuroImage **62**(3), 2129

[6] Schlegel, F. *et al.* (Jan. 2012). Brain Topography **25**(1), 20

[7] Grech, R. *et al.* (7th Nov. 2008). Journal of NeuroEngineering and Rehabilitation **5**(1), 25 [8] Brookes, M. J. *et al.* (1st Apr. 2009). NeuroImage **45**(2), 440

Developing Microfluidic Devices and Systems for Isolation and Detection of Extracellular Vesicles, EVs

Himayasri Rao Lekkala[1], Dr Ian D. Johnston[1], Dr Nikolay G. Dimov[1] and Dr Jameel M. Inal[2]

[1]University of Hertfordshire, School of Physics, Engineering and Computer Science
[2]Cellular and Molecular Immunology Research Centre, London Metropolitan University, U.K.
hl18aav@herts.ac.ukaddress

Keywords: Extracellular Vesicles (EVs), Tangential flow filtration (TFF), Nanoparticle tracking analysis (NTA), Transmission Electron Microscopy (TEM).

Introduction

Extracellular Vesicles (EVs) are lipid-bound bilayer structures released by cells into the extracellular space. They are 30 to 10,000 nanometres in size and are present in all bodily fluids. They carry a cargo of proteins, lipids, nucleic acids, RNA, and DNA [1]. A common interest in Extracellular vesicles research is to study their ability to act as carriers of biomarkers. They also act as an additional mechanism for intercellular communication, transporting biomolecules between cells, contributing to physiological and pathological activities like metabolism and progression of cancer cells. A major hindrance in bringing EVs into the clinical setting is the lack of standardization in isolation and analysis methods.

Currently, ultracentrifugation, (UG) is the gold standard technique for EV isolation. UG has its drawbacks of long process times, large sample volumes to process, less yield, and expensive equipment. Alternatively, ultrafiltration, a size-based separation is another common technique, used for the isolation of EVs [2]. It uses membranes with a molecular weight cut-off (MWCO) to separate the EVs based on their size. The process is less time-consuming than UG and requires no special instrumentation. This contribution here conveys a novel bench-top method using ultrafiltration in addition to tangential flow filtration for isolating EVs from complex media in three easy steps.

The objective of the tangential flow filtration (TFF) operation, presented in this contribution, is to reduce the accumulation of contaminants at the membrane surface, preventing fouling. It is also called crossflow filtration because the feed flows in at a 90-degree angle with the filtration flow. A major drawback of the existing ultrafiltration methods is the clogging and trapping of EVs due to the shear forces. In our device the feed flows in the parallel direction to the membrane. This flow continuously sweeps the surface of the membrane to protect it from clogging during the purification of the EVs. It is one proven ways to filter liquids with a high concentration of substances. The TFF is used to collect either the material passing through the membrane called permeate or the material retained by the filter called retentate. Tangential flow ultrafiltration devices are used extensively in bioprocessing since they exhibit high yield, which is beneficial, example in therapeutic applications.

Experimental

The microfluidic Tangential Flow Filtration device, µTFF, shown in (Figure 1) was engineered at the University of Hertfordshire, for the isolation of EVs.

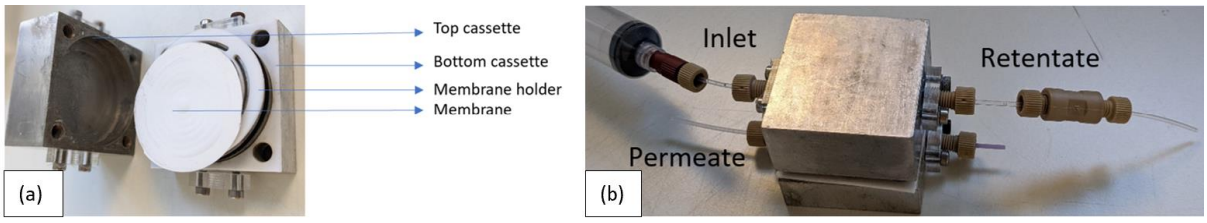

Figure 1. (a) Exploded view of the device. (b) The device is clamped and connected to the tubing.

The device has been tested using *E. coli* K12 culture media. The process was done in three stages changing the membranes accordingly at each stage. At stage A, the prepared *E. coli* K12 culture media was filtered using a 0.1-micron porous membrane to filter the bacteria of 0.5µm width and 2µm length. The purified sample was collected as permeate P_A and the bacteria is retained above the membrane and comes out as retentate, R_A. The permeate is a collection of EVs from *E. coli*, protein, and other molecules. The permeate of stage A is used as a

feed for stage B. At stage B, a 500kDa membrane was used to filter EVs for purity. At this stage, the protein and other molecules were filtered as permeate, P_B, and EVs were retained as retentate, R_B. Retained R_B was used as feed for stage C. At stage C, a 20 nm filter was used and a concentrated sample of EVs is retained as retentate, R_C. The excess protein along with other possible contaminants was filtered, staining most of the fluid at this stage. The three-stage TFF process of isolation of EVs is shown in figure 2, below.

Figure 2. A Block diagram representing the three stages of TFF.

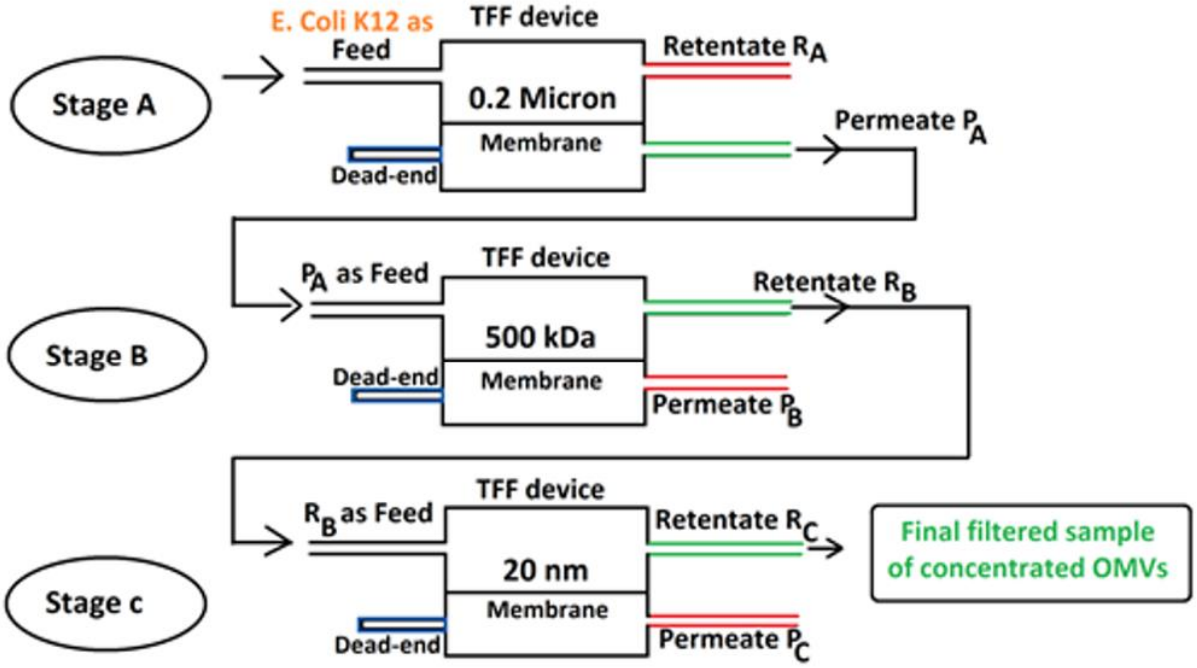

Results and discussion

As part of this project, we engineered and characterised a microfluidic Tangential Flow Filtration (µTFF) system, as shown in figure 1(a). We isolated EVs from *E. coli* samples using the µTFF and analysed the samples to get an insight into the size and shape with Transmission Electron Microscopy, (TEM), as shown in figures 3(a) and 3(b). The concentrations of EVs were measured using Nanoparticle Tracking Analysis (NTA) and is shown in figure 3(c).

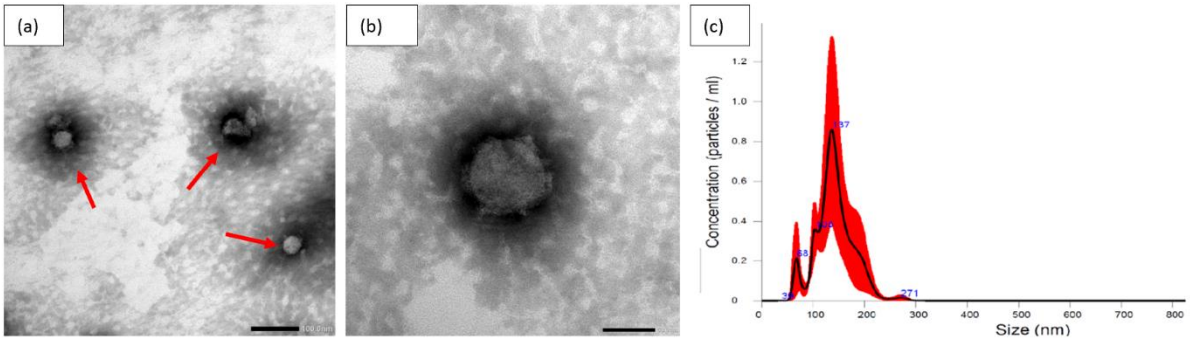

Figure 3. Image from the TEM analysis (a) TEM of EVs extracted from E. coli K12 culture, pointed used arrows. (b) Individual EVs (from E. coli) from TEM analysis. (c) NTA histogram from the retentate at stage C TFF process, using 20 nm filtration membrane to obtain concentrated EVs.

NanoSight NS300 system (Malvern Instruments Ltd.) with a laser of wavelength 405nm was used to analyse the particle size and concentration of EVs sample obtained at the retentate stage C. The sample was administered at stop-flow conditions at three different locations at 25 °C. The data was recorded in three sets of three videos each 30 s with a 1 s delay between recordings. The camera level was adjusted to 5 and the detection threshold was set at 6. The sample was measured in triplicate and data were combined for analysis using the NTA software version 3.2 (Malvern, UK).

Using a 20 nm ultrafiltration membrane, at stage C it is expected that the TFF device retains EVs and filters protein and other molecules less than 20 nm in diameter. Figure 3, (C) shows the particles in the range of 30 to 300 nm indicating the presence of EVs.

Conclusion

We conveyed a microfluidic device and method for the effective isolation of bacterial Extracellular Vesicles (EVs) by applying µTFF process. The purification and maximum quantification of these vesicles is achieved in three stages using the µTFF device. The feed flows in parallel to the surface of the membrane under a constant flow rate. There is a functionality that allows to monitor the pressure continuously and to estimate when the clogging of the membrane occurs. Moreover, using that insight the potential damage to EVs could be reduced further by regulating the transmembrane pressure and balancing it with the flow parallel to the membrane.

To date, the microfluidic system we developed, allowed the reproducible isolation of EVs, documented in the NTA and TEM analysis. Further understanding of the µTFF device, its optimal operating parameters, and working range, will be sought to enhance EV isolation towards potential scale-up for the development of EV-based therapies, vaccines, and formulations.

References

[1] Deatherage B, Cookson B. Membrane Vesicle Release in Bacteria, Eukaryotes, and Archaea: A Conserved yet Underappreciated Aspect of Microbial Life. Infection and Immunity. 2012;80(6):1948-1957.
[2] Ch Veziroglu E, Mias G. Characterizing Extracellular Vesicles and Their Diverse RNA Contents. Frontiers in Genetics. 2020;11o, S.K. *et al* (2003) Journal of microelectromechanical systems 12(1) 70.

University of Hertfordshire UH

Carbon-to-oxygen ratio as a clue to the formation of Ross 458c

Josefine Gaarn[1], Ben Burningham[2]

[1 2]Centre for Astrophysics Research, University of Hertfordshire

Keywords: Ross 458c, retrievals, brown dwarfs, atmospheric studies, C/O ratio

Brown dwarfs, intermediate mass objects with masses between planets and stars, are thought to primarily form like stars. However low-mass companions might form like planets, in a disk. Comparing the carbon-to-oxygen ratio (here, estimated from the methane/water ratio) of the primary and its companion, can provide clues to the formation mechanism and pathway, as they are expected to be the same if the objects formed at the same time. We make use of archival FIRE near-infrared spectroscopy covering 1.0-2.4 µm [1] to estimate the abundances for Ross 458c, a potentially planetary mass object orbiting a pair of red dwarf stars. We find that the atmosphere of Ross 458c is best described by a cloudy model, and a C/O ratio of 1.97. It is thus unlikely that Ross 458c shares a common C/O ratio with its primary stars, suggesting that Ross 458c might have formed in a disk like a planet.

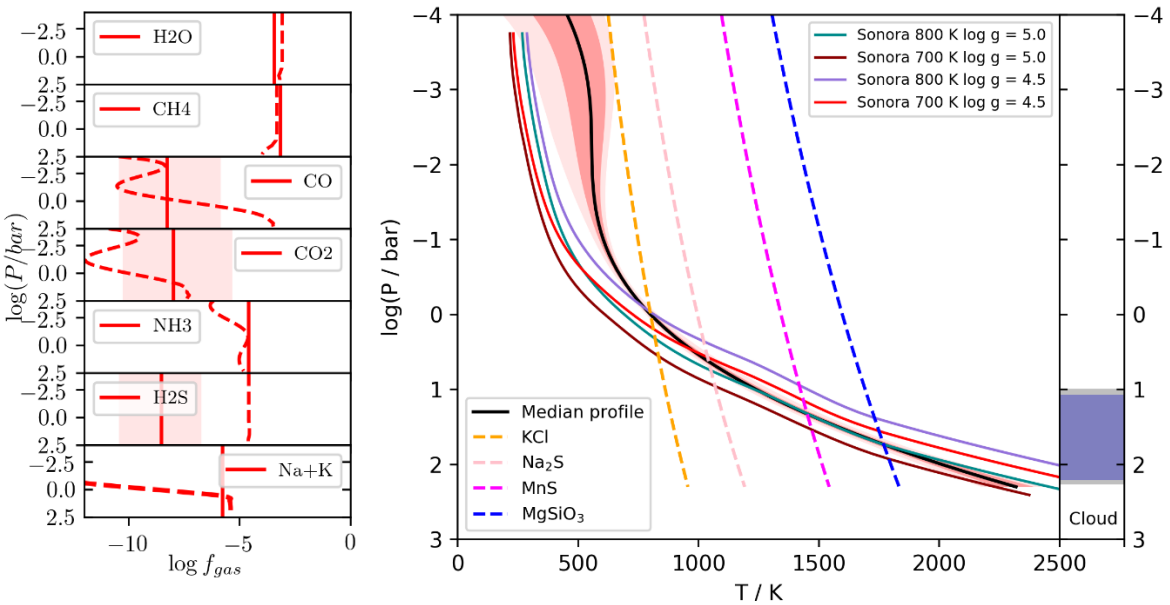

Fig 1. Left – Retrieved gas fractions (solid line) compared to equilibrium predictions (dashed line). Right – Retrieved thermal profile with cloud condensation curves and Sonora grid models overplotted.

References

[1] Burgasser, A. J. *et al.* (2010) ApJ **725**(2) 1405

University of Hertfordshire UH

Using LSA to reduce Textual-based neural models' complexity

Harpreet Singh[1], Syed Muhammad Kamran[2], Na Helian[3]

[1,2,3]University of Hertfordshire (SPECS)

Keywords: Latent Semantic Analysis (LSA), Sentiment Analysis, Text classification, Natural Language Processing (NLP)

Text data is a common unstructured data type, and it is readily available and collectable due to the surge of social media, online encyclopaedia, and other text-based online platforms. Several pieces of literature have purposed studies on analysing text using Machine learning models for text classification tasks. Many state-of-the-art studies employ complex neural network models, containing enormous model parameters to train, which requires extensive training time and hardware requirements. This study aims to use Latent Semantic Analysis (LSA) - a Natural Language Processing technique on text-based neural network models to investigate if we can reduce the complexity of the model (in terms of the number of trained parameters) without compromising text classification performance. The main objective behind this research is to reduce model complexity by applying LSA two different aspects of text-based neural network models. The first aspect is the input word vectors which are reduced to lower dimensions by applying two dimensional (2D) LSA and the second aspect is the output of the Embedding layer where the embeddings are converted into low-rank approximations using a three-dimensional (3D) LSA before succeeding to the following neural layers, which means reducing the number of independent columns in input. Both this aspect is common among popular text classification models. This study investigated the combined impact of the above aspects on a text-classification neural network.

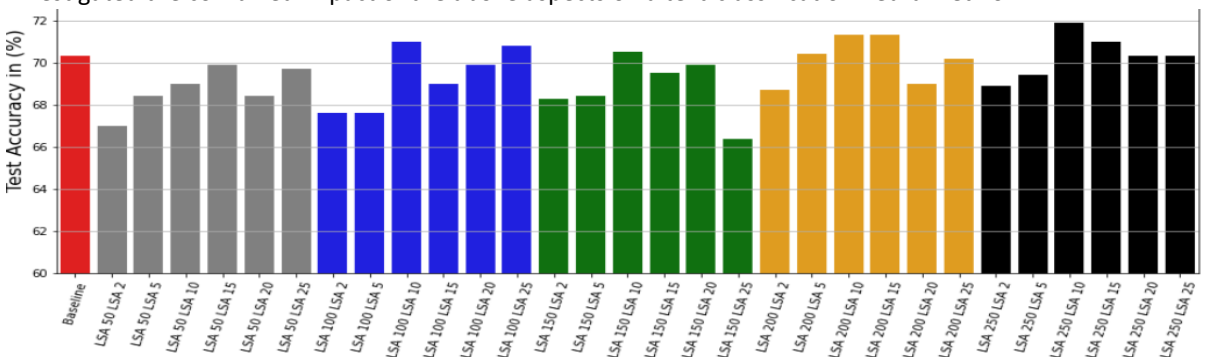

Fig. 2 – Test Accuracy vs Proposed models with variable ranks of 2D and 3D LSA applied to two different aspects of BLSTM-2DCNN (Baseline) on a subset of Sentiment140 dataset. The models are named as "LSA X LSA Y" where X is the rank of 2D LSA applied at preprocessing step and Y is the rank of 3D LSA applied to output of Embedding layer.

The proposed model have LSA applied to- first- input word vectors, second- the Embedding Layer output of an existing text-based neural model, BLSTM-2DCNN [1]. The BLSTM-2DCNN model is used as the baseline during experimentation. Experiments are conducted on two different text classification tasks which are PAN-2018 datasets [2] (for Author Identification task) and Sentiment140 dataset [3] (for Sentiment Analysis). In this study, 300 vector long input word vectors are reduced to 50, 100, 150, 200 and 250 dimensions using 2D LSA which reduced the overall model training parameters to 5%, 15%, 29%, 48% and 72% respectively. Models generated using the same value for LSA 2D but with different values for LSA 3D have a reduction in the rank of the input matrix which means incorporating more domain knowledge. The results show that the 3D LSA can be effectively used to obtain the low-rank approximation of the Embedding Layer output and provide performance boost over baseline when combined with certain 2D LSA ranks. However, the best LSA ranks value for peak performance varies across dataset. *Fig. 1* shows various model performance with various combination of 2D- 3D LSA rank value, and it is worth noting that some combinations give significant boost to the performance compared with baseline.

References

[1] P. Zhou, Z. Qi, S. Zheng, J. Xu, H. Bao, and B. Xu, "Text Classification Improved by Integrating Bidirectional LSTM with Two-dimensional Max Pooling." pp. 3485–3495, 2016.

[2] M. Kestemont *et al.*, "Overview of the Author Identification Task at PAN-2018: Cross-domain Authorship Attribution and Style Change Detection," *CEUR Workshop Proc.*, vol. 2125, 2018.

[3] A. Go, R. Bhayani, and L. Huang, "Twitter Sentiment Classification using Distant Supervision," CS224N Project Report, Stanford, 2009.

University of Hertfordshire UH

LBP-CA: A Short-term Scheduler with Criticality Arithmetic

Sajid Fadlelseed[1*], Raimund Kirner[2], and Catherine Menon[3]

[1]*Department of Computer Science, University of Hertfordshire, Hatfield, UK*
*Corresponding author: {q.fadlelseed, r.kirner, c.menon}@herts.ac.uk

In safety-critical systems a smooth degradation of services is a way to deal with resource shortages. Criticality arithmetic is a technique to implement services of higher criticality by several tasks of lower criticality. In this paper, we present LBP-CA, a mixed-criticality scheduling protocol with smooth degradation based on criticality arithmetic. In the experiments we show that LPB-CA can schedule more tasks than related scheduling protocols (BP and LBP) in case of resource shortage, minimising the negative effect on low-criticality services. This is achieved by considering information about criticality arithmetic of services.

Keywords: real-time systems; safety integrity level; scheduling; mixed-criticality

Introduction

Criticality Arithmetic (CA) or SIL-arithmetic as termed in [1], is a Mixed-criticality (MC) model that assembles a number of replicated tasks with low criticality levels, to implement a service of higher criticality level. The Adaptive Tolerance-based Mixed-criticality Protocol - Criticality Arithmetic (ATMP-CA) [4] is CA-aware mid-term scheduler that optimises the utility of individual tasks when permanent fault occurs e.g., core-failure, to maximise the overall system utility, here we present a novel CA-aware short-term scheduler (LBP-CA) which assures return to Normal-mode from Critical-mode, much earlier than reference schedulers that do not take the use of criticality arithmetic into account. MC systems enter the Critical-mode whenever a transient fault e.g., task overrun occurs, which results in abandoning release of Low-criticality tasks to avoid their interference on High-criticality tasks during the Critical-mode [5].

Reference schedulers are Bailout Protocol (BP) [3] and Lazy Bailout Protocol (LBP) [2]. BP and LBP define three criticality modes to schedule the execution of tasks with different criticality levels: Normal-mode, Bailout-mode and Recovery-mode. Bailout-mode represents the Critical-mode explained above, and Recovery-mode is used to ensure that the last High-criticality task with Low-priority is executed before returning to Normal-mode. LBP differs from BP in that instead of dropping Low-criticality tasks during Bailout and Recovery modes, they are added to a Low-priority queue for possible execution when the system returns to Normal-mode. Though LBP may drop less tasks than classic BP, it doesn't improve the BP functionality that operates the process of returning to Normal mode.

System Model: We assume a single processor mixed-criticality system, which consists of multiple services that could have different levels of criticality. A service can be implemented by one task or multiple tasks using criticality arithmetic [1]. Each service is identified by the tuple: $\boldsymbol{s} = \langle \boldsymbol{id}, \boldsymbol{l}, \boldsymbol{T} \rangle$, where $\boldsymbol{id}$ is the service identifier, $\boldsymbol{l}$ is the service criticality and $\boldsymbol{T}$ is the set of tasks implementing the service. Each individual task () is defined by the tuple $\boldsymbol{\tau} = \langle \boldsymbol{id}, \boldsymbol{p}, \boldsymbol{d}, \boldsymbol{c1}, \boldsymbol{c2}, \boldsymbol{L}, \boldsymbol{s} \rangle$, where $\boldsymbol{id}$ is the task identifier, $\boldsymbol{p}$ is the task period, $\boldsymbol{d}$ the task deadline, $\boldsymbol{c1}$ *optimistic* worst-case execution time estimate (WCET1), $\boldsymbol{c2}$ *pessimistic* worst-case execution time estimate (WCET2), task criticality is defined by $\boldsymbol{L}$ and $\boldsymbol{s}$ is the service that is implemented by the task.

Experimental Setup

We have implemented a short-term scheduling simulator which is configured to simulate mixed-criticality services on a single processor system. The simulator has also implemented the underlying scheduling algorithm (deadline-monotonic) and the references mixed-criticality protocols (BP and LBP) and the novel mixed-criticality protocol (LBP-CA).

We have generated a task-set with random parameters for task periods and worst-case execution time and mix of implicit and constrained deadlines. The criticality of a task or service is either High or Low, which corresponds to the criticality level of the task. We have constrained the task generation such that it includes a single High criticality CA-aware service (S2). The complete structure of tasks and services is implemented in the following task-set in Table 1.

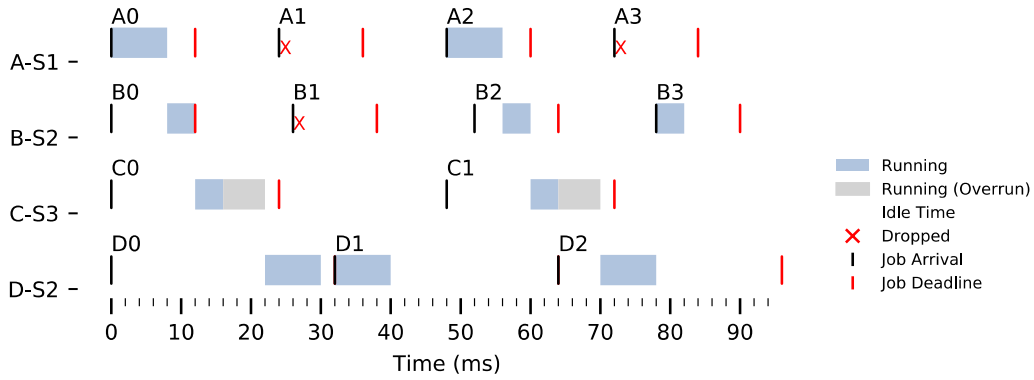

(a) BP protocol (3 *dropped jobs, 10 completed jobs)*

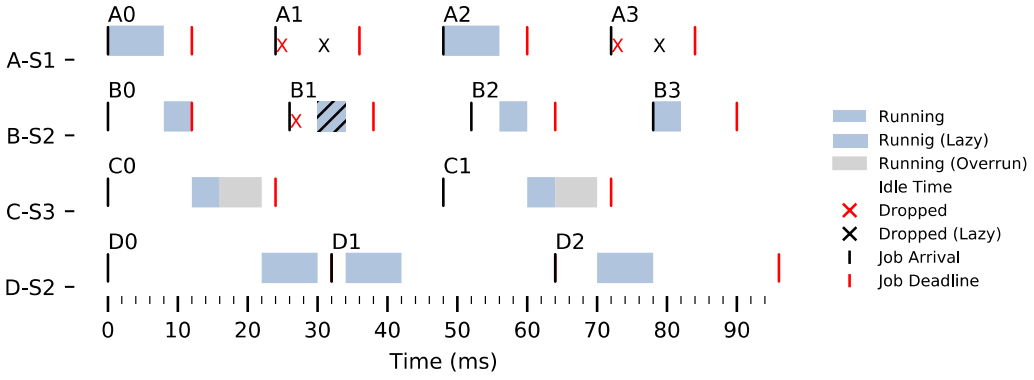

(a) LBP protocol (2 *dropped jobs, 11 completed jobs)*

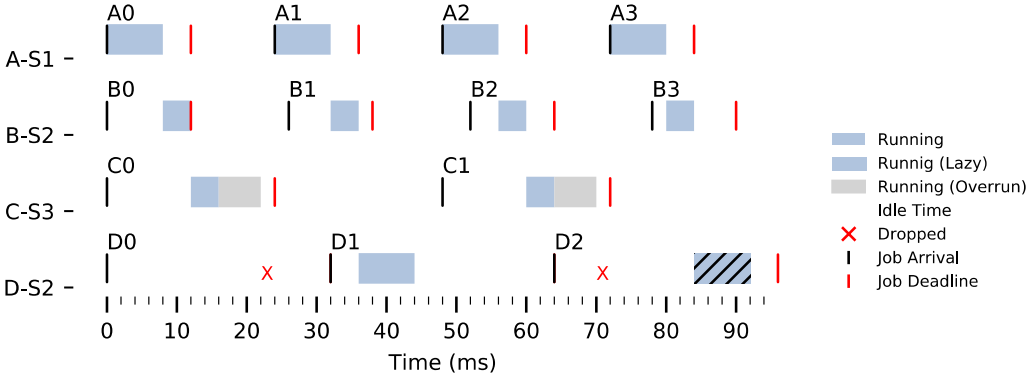

(a) LBP-CA protocol (1 *dropped job, 12 completed jobs)*

Figure 1. Comparison of scheduling mixed-criticality tasks between BP, LBP and LBP-CA

t.id	t.p	t.d	t.c1	t.c2	t.L	s.id	s.l
A	24	12	8	8	Low	S1	Low
B	26	12	4	4	Low	S2	High
C	48	24	4	10	High	S3	High
D	32	32	8	8	High	S2	High

Table 1. Set of Services and Tasks (only S2 use Criticality Arithmetic)

Results and discussion (Section heading, Calibri 12 pt)

The purpose of our experiment was to show that the LBP-CA returns to Normal-mode with the least number of abandoned Low-critical tasks compared to reference protocols. Figure 3 shows the schedule for the task-set presented in Table 1. In Figures 3 (a), (b) and (c), we can observe that job $\boldsymbol{C0}$ overruns its $\boldsymbol{c1}$ estimates, which results in entering Critical-mode. As per Figures 3 (a), (b) and (c), in BP and LBP protocols we can observe that the overrun caused the system to enter the Bailout-mode and abandon the Low-Criticality jobs ($\boldsymbol{A1}$ and $\boldsymbol{B1}$), to avoid possible interference with High-Criticality jobs. However, the LBP protocol (Figure 3 (b)) shows the successful allocation for the job $\boldsymbol{B1}$ using its lazy execution mechanism. In contrast, our LBP-CA protocol (as shown in Figure 3 (c)) scheduled all jobs successfully except job $\boldsymbol{D1}$. This is because the first instance of its replica B has been executed successfully. Hence entering Recovery-Mode has been mitigated. Overall, the collected simulation results indicate that the LBP-CA drops a smaller number of Low-Criticality jobs and efficient management for the system run-time modes in comparison to reference schedulers (BP and LBP protocols).

Conclusion

Integrating CA to Mixed-criticality schedulers as in (LBP-CA), allows efficient mode-change management between Normal-mode and Critical-mode/s due to transient faults. LBP-CA can access information about criticality arithmetic (CA) via task redundancy compared to referenced scheduling protocols (BP and LBP) which are CA-agnostic. Our simulation data shows that even at/after resource shortage, LBP-CA returned to the normal state prior to BP and LBP, providing a smoother service degradation.

References

[1] Menon, C., Iacovelli, S. and Kirner, R., 2020, May. ODRE Workshop: Using SIL Arithmetic to Design Safe and Secure Systems. In 2020 IEEE 23rd International Symposium on Real-Time Distributed Computing (ISORC) (pp. 213-218). IEEE
[2] Iacovelli, S. and Kirner, R., 2019. A lazy bailout approach for dual-criticality systems on uniprocessor platforms. Designs, 3(1), p.10.
[3] Bate, I., Burns, A. and Davis, R.I., 2015, July. A bailout protocol for mixed criticality systems. In 2015 27th Euromicro Conference on Real-Time Systems (pp. 259-268). IEEE.
[4] Fadlelseed, S., Kirner, R. and Menon, C., 2021. ATMP-CA: Optimising Mixed-Criticality Systems Considering Criticality Arithmetic. Electronics, 10(11), p.1352.
[5] Vestal, S., 2007, December. Preemptive scheduling of multi-criticality systems with varying degrees of execution time assurance. In 28th IEEE international real-time systems symposium (RTSS 2007) (pp. 239-243). IEEE.

University of Hertfordshire UH

Investigating Instance Weighted Spectral Clustering using Genetic Algorithms

Paul Moggridge 1[1*]

[1]*University of Hertfordshire*

*corresponding author: p.moggridge@herts.ac.uk

Spectral clustering is versatile clustering algorithm, however, there exists conditions under which it can provide inaccurate results. This work investigates if using a weighted sub-sampling approach can enhance the accuracy of spectral clustering on challenging datasets. To choose the weights which guide the sub-sampling, a genetic algorithm is employed. The outcome of the experiments was that it is possible to enhance the accuracy of spectral clustering using a weighted sub-sample of instances. In this work, the genetic algorithm had knowledge of the ground truth (which is not suitable for real clustering problem) however, it demonstrated that it is possible to perform a weighted sub-sample that increases the accuracy of spectral clustering. This raises the question of how to define these weights.

Keywords: Spectral Clustering, Genetic Algorithms, Instance Weighted Clustering

Introduction

Clustering is an unsupervised learning technique. The purpose of clustering is to find groups of data points which are similar to each other within a dataset. Spectral clustering is a popular and versatile clustering algorithm. It is able to group data points of arbitrary shape into clusters. However, there are some conditions under which it can fail to accurately group the data points [1]. These conditions include datasets where the there is high density clusters positioned adjacent to low density clusters (this can occur in imbalanced datasets) and datasets which contain geometrically defined clusters of uniform density. Research has been completed to overcome these weaknesses but the results generally involve directly modifying the implementation of the spectral algorithm. Hence there is a gap for a simpler solution to these weaknesses.

An approach which could lead to a simpler solution is instance weighting. Weights could be used by a sub-sampling step to select instances to present to the spectral clustering to give spectral clustering a cleaner / more-representative view of the data. Sub-sampling has been shown to benefit accuracy for classification algorithms, particularly in the case of imbalanced datasets [2][3]. In clustering, instance selection is less researched and it is not clear what the best approach is.

Evolutionary algorithms, such as Genetic algorithms can be used to search a for an optimal solution within a large problem space. This makes it suitable for a many problems. Genetic algorithms have been directly applied to clustering [4][5]. However, they can also be applied to a select a sample [3][6]. Some research finds that genetic algorithm based under-sampling for classification decreases accuracy [6] while others find that increase accuracy [3]. It appears this work is the first attempt to use a genetic algorithm to investigate sub-sampling (instance selection) for the spectral clustering algorithm.

Experimental

The objective of the methodology was to search for a weighting scheme which could increase the robustness and accuracy spectral clustering. To test if the spectral clustering a been improved three datasets that are known to be challenging for spectral clustering were trialed " Disc Tubes", "Three Wells" and "Imbalanced Blobs". Additionally, the "Half Moons" dataset was was trialed as it is popular benchmark for clustering algorithms which can handle clusters of arbitrary shape. An overview of these datasets can be seen in Table 1.

The investigation uses a genetic algorithm to search for a weighting scheme [7]. The genetic algorithm maintains a population of individuals. These individuals consist of a list of float values, where the length of the list corresponds to the number of instances in the given dataset, thus providing each instance with a corresponding weight value in each individual. The genetic algorithm performs selection, crossover and mutation on the population searching for optimal values for the weights. To guide the genetic algorithm's search it is uses a fitness function. The fitness function favours members of the population which have a high Normalized Mutual

Information (NMI) based on the ground truth. While an accurate clustering is inevitably somewhat subjective, NMI provides an good indication of accuracy. To evaluate an individual with the NMI, the fitness function uses the float values as weights to guide a sub-sampling step which selects sample of data to send to spectral clustering. The number instances in the sample is chosen dynamically based on the weights. The fitness function repeats the sub-sampling and spectral clustering step 3 times to obtain an average NMI value.

Name	**Number of Instances**	**Number of Features**	**Clusters**	**Brief Description**
Disc Tubes	175	2	3 (144 + 15 + 16)	Geometrically defined clusters, a box on the left, two circles on the right.
Half Rings	60	2	2 (30 + 30)	Two half rings, partially interlocking.
Three Wells	120	2	3 (60 + 30 + 30)	One large dispersed cluster with two small dense cluster adjacent to it.
Imbalanced	200	2	2 (180 + 20)	Two clusters, with imbalance in their counts of instances.

Table 1. An overview of the four datasets trialed.

As spectral clustering within the fitness function does not cluster the full dataset, it is necessary to propagate the cluster labels. The data points which did not pass through spectral clustering receive their cluster assignment via a label propagation function which assigns the cluster label based on a radial basis function. Spectral clustering used the nearest neighbor method for constructing it's affinity matrix with neighbors = 10.

The settings for the genetic algorithm were as follows, maximum number of iterations 50, population size 20, mutation probability 0.15, elit ratio 0.01, crossover probability 0.5, parents portion 0.2 and crossover type set to "uniform".

Results and discussion

The resultant instance weights for the datasets can be seen on the left of Figure 1 indicated by the colour intensity of the purple. The red x's on instances indicate that instance has below 0.1 weight, indicating that it is among the least likely instances to be sampled. On the right of Figure 1, you can see the fitness function, since the genetic algorithm minimizes the fitness function, a minus sign is placed in front of the NMI score, hence lower is better (-0.9 on the figure is actually 0.9 average NMI score).

For the Disc Tubes dataset spectral clustering typically achieves 0.54 accuracy but with the genetic algorithm controlling the weights for sub-sampling this increased to over 0.9. See the Disc Tubes result on the top left of Figure 1, note that the two circular clusters on the right of the sub-figure are surrounded by low weight points. On this dataset and Three Wells dataset, it appears to have learnt that not including the points on the edges of clusters makes the dataset easier to cluster.

For the Imbalanced dataset, spectral clustering typically achieves 0.53 accuracy but with the genetic algorithm controlling the weights sub-sampling this increased to over 0.6. On this dataset, it appears to have learnt balancing the clusters makes the dataset easier to cluster.

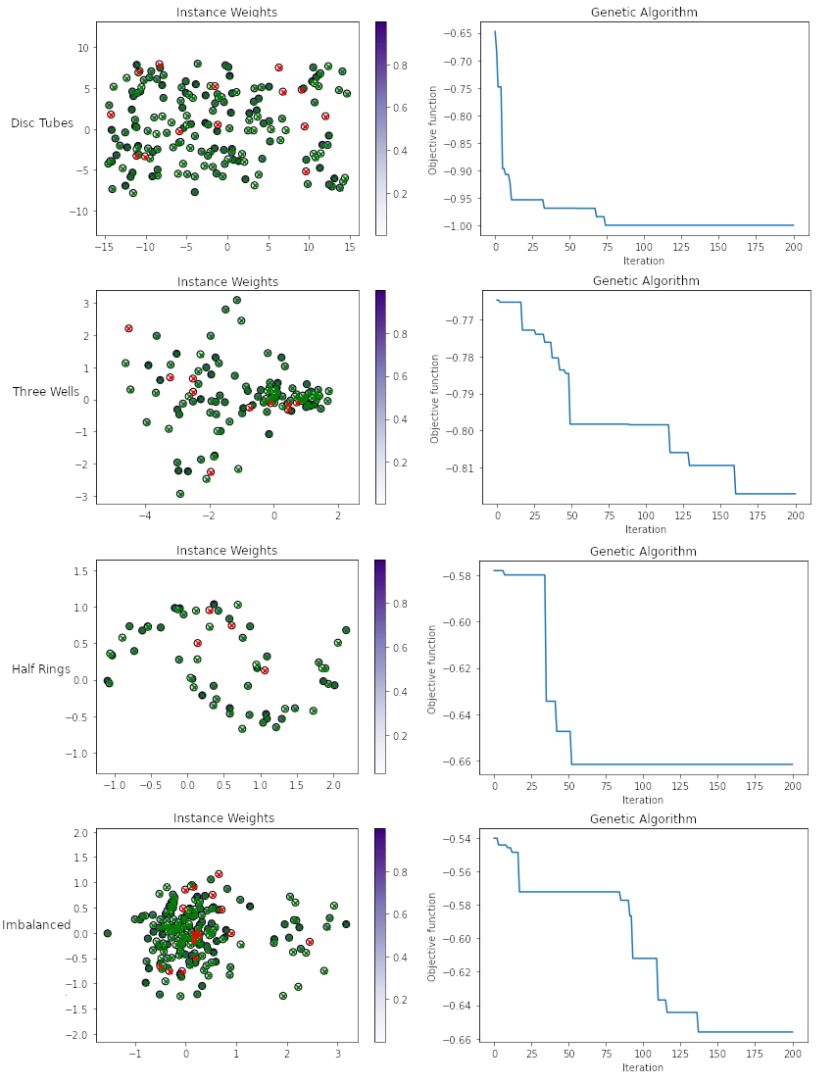

Figure 1. The results of the experiments, the sub-figures on the left shows the weights found by the genetic algorithm for each data point, the sub-figures on the right show fitness function over time

Conclusion

In conclusion, more computation, searching and analysis is required to find a model for choosing instance weights for the spectral clustering algorithm, but these small scale initial tests show there may be a model for weighting instances to increase the accuracy of spectral clustering. The genetic algorithm based sub-sampling was able to increase the accuracy of the spectral clustering across all datasets tested, mostly the gain was minor (increase of ~0.1 NMI score) although in one case it was able to increase accuracy by a large margin (increase of ~0.5 NMI score). The results support hypothesis that weighted sub-sampling can increase the accuracy and robustness of spectral clustering, if an appropriate weighting approach could be found.

Reference list

[1] Nadler B and Galun M. Advances in Neural Information Processing Systems **19** (2006).
[2] Tsai C, Lin W and Hu Y and Yao G Information Sciences **477** p.47-54 (2019).
[3] Ha, Jihyun and Lee, Jong-Seok, Int'l Conf. on Ubiquitous Info. Management and Communication **95** p.1-6 (2016).
[4] Freitas A, Data Mining and Knowledge Discovery Handbook, p.371-400 (2009).
[5] Lorena L and Furtado J, Evolutionary Computation, **9** p.309-327 (2001).
[6] Tsai C, Eberle W and Chu C. Knowledge Based Systems **39** p.240-247 (2013).
[7] Solgi R and PyPi https://pypi.org/project/geneticalgorithm/

University of Hertfordshire UH

Climate Extremes in Coupled Climate Models

Marc Norgate[1], P. R. Tiwari[1, 2], D. Kumar[3]

[1]Centre for Atmospheric and Climate Physics Research, University of Hertfordshire, UK

[2]Centre for Climate Change Research, University of Hertfordshire, UK

[3]Department of Meteorology, University of Reading, UK

Climate change affects human health [1,2,3, 4]; however, there have been no regional scale, systematic efforts to quantify the climate extremes (e.g., heatwave) related human health impacts that have already occurred due to climate change. Here, we use 13 state-of-the-art coupled climate models from CMIP6 experiments (simulation performed with Shared Socioeconomic Pathways -SSPs) [4] along with their ensembles to estimate their fidelity and associated uncertainties in predicting climate extremes over South Asia region that has resulted from human-induced warming, during the historical, near and far future period.

Keywords: Climate change, Climate Extremes, Climate model, SSP, human health

Introduction

The effects of climate change and global warming can be seen across the globe. Each decade is warmer than the last and has already had some serious effects on the world's population, from more frequent wildfires to an increase in the number, duration and intensity of tropical storms [6].

Heatwaves are a type of climate extreme weather event, generally defined as three or more consecutive days of extreme temperature. The frequency, intensity and duration of extreme heat events have increased [7] and are continuing to increase [8]. They have a significant impact on human health and have caused many deaths globally, with a greater impact on the elderly, women and those suffering from chronic respiratory disorders [9]. This poses a risk to the world's population, especially those in lesser developed countries who will struggle to mitigate this increase in heatwave severity. The increase in global warming has seen an increase in heatwave characteristics (frequency, duration and higher extreme temperatures) over Southeast Asia [10].

This work aims to utilise state-of-the-art Climate Model Inter-comparison Project 6 (CMIP6) simulations to assess how climate extremes will change in the future over South Asia.

Experimental

13 CMIP6 models (see Table 1) are used in simulating maximum temperature over South Asia. The historical analysis is from 1901–2014 and this time period is used to examine the fidelity of these models. Shared socioeconomic pathways (SSPs) SSP1-2.6, SSP2-4.5 and SSP5-8.5 have been used for the future time period 2015-2100 and have been split into near-future (2030-2060) and far-future (2070-2100) to evaluate future changes in maximum near-surface temperature over South Asia. SSP1-2.6 represents a "green road", SSP5-8.5 represents fossil-fueled development and SSP2-4.5 represents a middle road [11]. We looked at June, July and August (JJA) for all time periods. The ensemble mean (EnsM) has been used for all 13 models.

Model	Country	Horizontal Resolution (lon and lat)	Model Vertical Levels (km)
ACCESS-CM2	Australia	192 x 144	85
CANESM5-CanOE	Canada	128 x 64	49
CMCC-ESM2	Italy	288 x 192	30
CNRM-CM6-1	France	362 x 294	75
FIO-ESM-2-0	China	192 x 288	26
GFDL-ESM4	USA	360 x 180	49
GISS-E2-1-H	USA	144 x 90	40
HadGEM3-GC31-LL	UK	192 x 144	85
INM-CM5-0	Russia	180 x 120	73
KACE-1-0-G	South Korea	192 x 144	85
MIROC6	Japan	256 x 128	81
MPI-ESM1-2-LR	Germany	192 x 96	47
UKESM1-0-LL	UK	192 x 144	85

Table 1: ESM's used

The maximum near-surface air temperature from CRU [12] at 0.5° resolution is used to evaluate the fidelity of these CMIP6 models. CRU is a well trusted source of historical observations [13] which is why is has been used for model validation.

Results and Discussion

We applied various skill metrices for model performance evaluation and found that ensemble of all the 13 CMIP6 models is close to the observation (Fig. 1 a & b) whereas individual model performance varied geographically. This is because individual models have their own interannual variability which affects the overall performance. Further we computed the temperature changes over 114 years (Fig. 1c) at 95% significance level and found that the EnsM seems to overestimate the temperature most notably seen over the Indo-Gangetic plain, Oman and Yemen. However, the EnsM still does a good job of modelling the climate over this region.

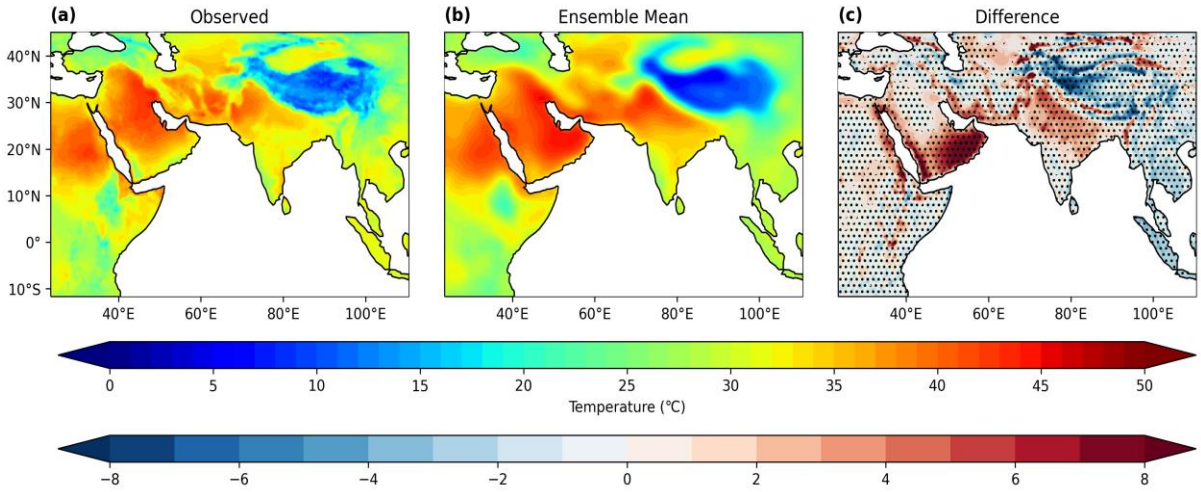

Fig. 1 – (a) JJA temperature changes (^{0}C) for 114 years (1901-2014); (a) Observed, (b) CMIP6 ensemble and (c) difference between ensemble & observation. The dots show the area of 95% significance.

Using SSPs we then looked at future changes in maximum temperature over South Asia (Fig. 2). All scenarios show an increase in temperature during the NF period with SSP585 being the most extreme increase. With sufficient mitigation strategies (SSP126) the maximum temperature over South Asia appears to level off during the FF period, whereas if we continue a fossil-fuelled development (SSP585) the maximum temperature is shown to continue to rise at a similar rate.

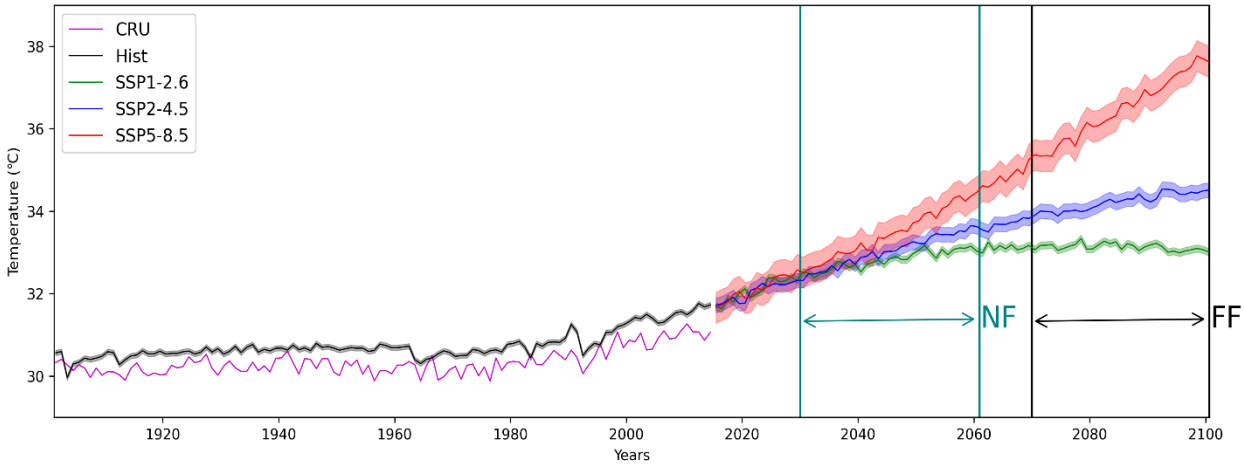

Fig. 2 – Historical (1901-2014) and future (2015-2100) changes in JJA maximum near-surface temperature over South Asia. NF shows the near-future period (2030-2060) and FF shows the far-future period (2070-2100). The purple line is the observed temperature, and the black line is the EnsM temperature for the historical period. For the future time period the green, blue and red lines represent SSP126, SSP245 and SSP585 respectively.

University of Hertfordshire UH

Conclusion

Climate extremes such as heatwaves have multiple and cascading impacts on society. Most densely populated parts of the world like South Asia (population of more than 1,980,000,000) [14] are prone to such extremes that put a large amount of people's health at risk. Our analysis shows that there is an increase in heatwave severity by the end of the century. Temperature predictions over South Asia were made using CMIP6 models where SSP based emission pathways are a key factor and our findings support that there is an urgent need for more ambitious mitigation and adaptation strategies to minimize the public health impacts of climate change. If we continue with fossil-fuelled development, temperatures over the South Asian region will continue to rise.

Reference List

[1] Delmotte et al, IPCC, 2021: Climate Change 2021: The Physical Science Basis. Contribution of Working Group I to the Sixth Assessment Report of the Intergovernmental Panel on Climate Change. Cambridge University Press, (2021).

[2] Rogelj, J. et al, Paris Agreement climate proposals need a boost to keep warming well below 2 °C. Nature **534**, p. 631–639, (2016).

[3] Benmarhnia et al, Vulnerability to heat-related mortality: a systematic review. Epidemiology **26**, p. 781–793, (2015).

[4] Cabrera et al, The burden of heat-related mortality attributable to recent human-induced climate change. Nature Climate Change **11**, p. 492–500, (2021).

[5] Eyring et al Overview of the Coupled Model Intercomparison Project Phase 6 (CMIP6) experimental design and organization, Geoscientific Model Development **9**, p1937–1958, (2016).

[6] H.-O. Pörtner, D.C. Roberts, M. Tignor, E.S. Poloczanska, K. Mintenbeck, A. Alegría, M. Craig, S. Langsdorf, S. Löschke, V. Möller, A. Okem, B. Rama (eds.), IPCC, 2022: Climate Change 2022: Impacts, Adaptation, and Vulnerability. Contribution of Working Group II to the Sixth Assessment Report of the Intergovernmental Panel on Climate Change [Cambridge University Press], (2022).

[7] Perkins, S. E. and L. V. Alexander, On the Measurement of Heat Waves, Journal of Climate **26.13**, p. 4500–4517, (2013).

[8] Zhao, Alcide, Massimo A. Bollasina, and David S. Stevenson, Strong Influence of Aerosol Reductions on Future Heatwaves, Geophysical Research Letters **46.9**, p. 4913–4923, (2019).

[9] Dippoliti, Daniela, Paola Michelozzi, Claudia Marino, Francesca Dedonato, Bettina Menne, Klea Katsouyanni, Ursula Kirchmayer, Antonis Analitis, Mercedes Medina-Ram´on, Anna Paldy, The impact of heat waves on mortality in 9 European cities: results from the EuroHEAT project, Environmental Health **9.1**, (2010).

[10] Dong, Zizhen, Lin Wang, Ying Sun, Ting Hu, Atsamon Limsakul, Patama Singhruck, and Sittichai Pimonsree, Heatwaves in Southeast Asia and Their Changes in a Warmer World, Earth's Future **9.7**, (2021).

[11] Keywan Riahi et al, The Shared Socioeconomic Pathways and their energy, land use, and greenhouse gas emissions implications: An overview, Global Environmental Change, Volume **42**, p. 153-168, (2017).

[12] Harris, I., P.D. Jones, T.J. Osborn, and D.H. Lister, Updated high-resolution grids of monthly climatic observations - the CRU TS3.10 Dataset. International Journal of Climatology **34.3**, p. 623–642, (2017).

[13] Mitchell, Timothy D. and Philip D. Jones, An improved method of constructing a database of monthly climate observations and associated high-resolution grids, International Journal of Climatology **25.6**, p. 693–712, (2005).

[14] Population of Southern Asia (2022) - Worldometer, 2022

Analysis of Modal Parameters' Variations due to Increased Impact Energy Damage in CFRP Laminates

Amafabia, Daerefa-a Mitsheal[1], David-West, Opukuro[1], Montalvão, Diogo[2] and Haritos, George[3]

[1] School of Physics, Engineering, and Computer Science, University of Hertfordshire, College Lane, Hatfield AL10 9AB, United Kingdom ;
[2] Department of Design and Engineering, Faculty of Science and Technology, Bournemouth University, Poole House, Talbot Campus, Fern Barrow, Poole BH12 5BB, United Kingdom.
[3]School of Engineering and the Environment, Kingston University London, Kingston upon Thames, Penrhyn Road KT1 2EE, United Kingdom.

Abstract: Oftentimes damage in composite structures is difficult to detect by visual inspection. Although the nature of Carbon Fibre Reinforced Plastic composite (CFRP) enhanced structures' specific mechanical properties when in comparison with steel or aluminium, medium to low energy impact may be sufficient to compromise its structural integrity. In this work, CFRP laminates of distinct stacking configurations were subjected to free-free suspended Experimental Modal Analysis (EMA) from 0 to 800 Hz frequency. Both damaged and undamaged samples of identical stacking sequence were examined. The results indicated a correlation between the changes in the modal parameters and the amount of energy dissipated.

Keywords: Frequency Response Function (FRF); Carbon Fibre Reinforced Plastic (CFRP); Modal Parameters; Composite; Experimental Modal Analysis.

1.0 Introduction

The good mechanical properties of composite structures, such as stiffness-to-weight ratio and strength has endeared it to several industries for various applications [1–5]. Despite its good mechanical properties, the materials are prone to failure in the through thickness direction of the fibre. In the case of aerospace structures, hailstone, bird strike, mishandled dropped equipment during maintenance/manufacturing, or debris and stones released during landing and take-off. Typically, medium to low energy impacts may introduce damage on the surface of the structure that is hard to detect by visual inspection or Visual Testing (VT). Such damage is known as BVID (Barely Visible Impact Damage). Damage due to such impacts can spread across the through thickness of the material by diverse damage mechanisms, but still not visible. This would definitely decrease the life span of the structure [6], with high safety concerns.

Through vibration testing, the behaviour of the global properties of a structure could be used for damage detection and identification. A review on damage detection using Structural Health Monitoring (SHM) and techniques has been conducted by [7–9]. Montalvão *et al.* [10] reviewed the vibration-based SHM with interest in composite materials. Although there are numerous techniques for identifciation of damage, the most frquently used technique is modal analysis [11]. This technique is based on the changes in the modal properties of structures. It is challenging to investigate the relationships between the characteristics of mechanical systems. However, by the assumption that the basic properties are of a Single Degree of Freedom (SDOF) system and studied individually, the dynamic properties of the mechanical system can be defined [12].

2.0 Experimental

The test plates were vertically suspended under a free–free suspended configuration with two strings (see figure 1). A force transducer is coupled at the edge of the test sample and connected to a mechanical shaker through a stinger. Samples were excited with a multisine [13] excitation signal in the frequency range of 0 to 800Hz with a 0.25Hz resolution.

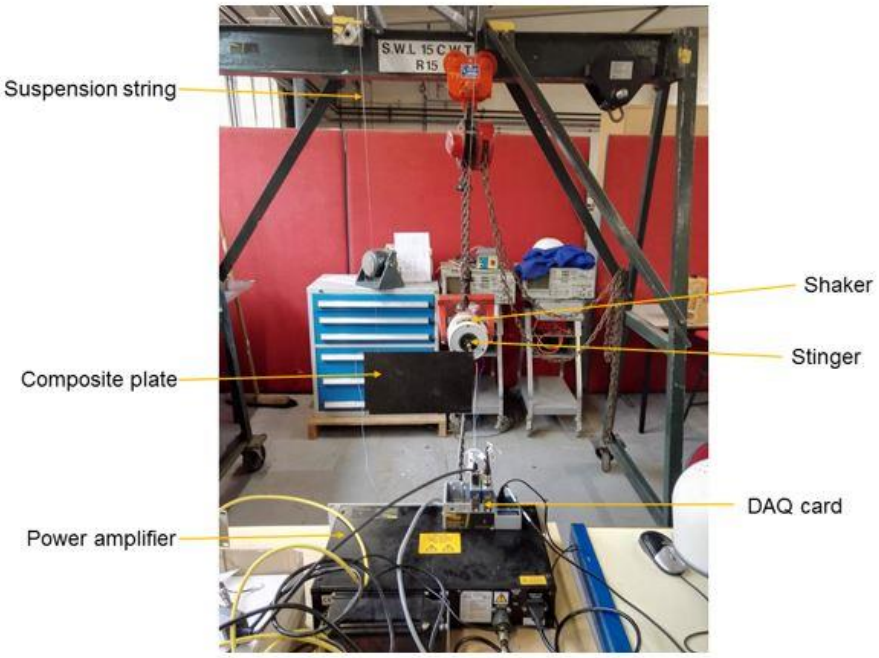

Figure 7. Experimental setup

The responses were determined at different locations, with 3 lightweight PCB teardrop accelerometers, type 352A24, each weighing 0.8 g. These were placed at the corners of the samples to measure the Frequency Response Functions (FRFs) at locations where the likelihood to have nodal lines is the lowest. The study considered both damaged and undamaged test specimens of similar stacking sequence.

3. Results and discussion

From the plots in Figure 2, it is observed that as there is an increase in the amount energy, the percentage change in both parameters increases. Except for plate C2, there seems to be a modal sensitivity to damage threshold where the modal parameters visibly start increasing. This happens from about 15J to 20J and helps understanding much of the discussion in previous sections where the sensitivity of the modal parameters to damage may not always be so clear.

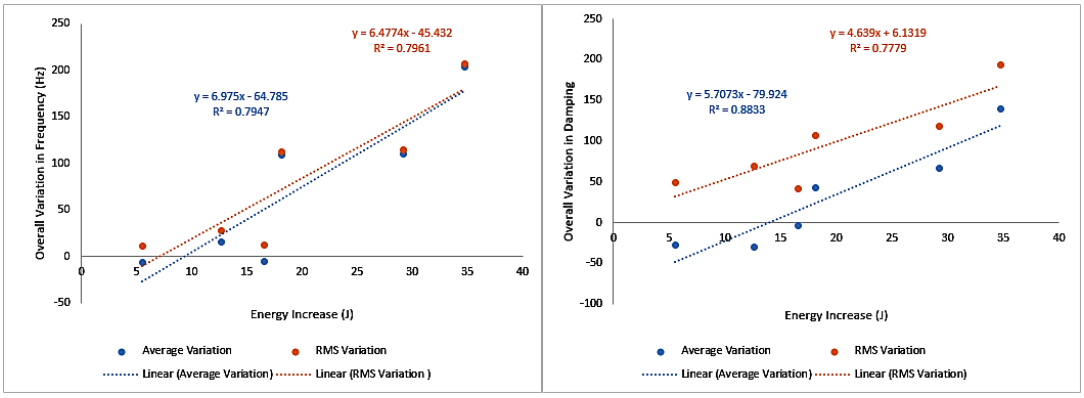

Figure 2. Linear trend for identifying the correlation between energy increase and modal parameters from Plate A1: (LHS) modal frequency (RHS) modal damping.

Assuming that the relations would be linear, R-squared correlation coefficients were determined, ranging from 0.76 to 0.85 and from 0.58 to 0.97 for the modal frequency and modal damping factors, respectively. This suggests the existence of a relationship between the increase in energy and the change in percentage in both modal damping and frequency. However, even if it still shows the greater dispersion on the results from the modal damping factor (because of a larger range), it is supporting the initial assumption that the hysteretic modal damping factors increases with damage in the CFRP laminates.

Conclusions

In this work, one important finding was that there are variations in the percentage in the modal damping and frequency as the amount of energy increases. The linear equations indicated a relationship between the amount of energy and the percentage changes in both modal damping and frequency. This occurred mostly from a threshold energy level between 15J and 20J.

References

[1] Kessler SS, Spearing SM, Atalla MJ, Cesnik CE, Soutis C. Damage detection in composite materials using frequency response methods. Compos Part B Eng 2002;33:87–95.

[2] Ye L, Lu Y, Su Z, Meng G. Functionalized composite structures for new generation airframes: A review. Compos Sci Technol 2005;65:1436–46.

[3] Montalvão D, Ribeiro AMR, Duarte-Silva JAB. Experimental Assessment of a Modal-Based Multi-Parameter Method for Locating Damage in Composite Laminates. Exp Mech 2011;51:1473–88.

[4] Montalvão D, Karanatsis D, Ribeiro AM, Arina J, Baxter R. An experimental study on the evolution of modal damping with damage in carbon fiber laminates. J Compos Mater 2014;49:2403–13.

[5] Huang L, Sheikh AH, Ng CT, Griffith MC. An efficient finite element model for buckling analysis of grid stiffened Laminated composite plates. Compos Struct 2015;122:41–50.

[6] Abrate S. Impact on Laminated Composites: Recent Advances. Appl Mech Rev 1994;47:517.

[7] Amafabia DM, Montalvão D, David-West O, Haritos G. A review of structural health monitoring techniques as applied to composite structures. SDHM Struct Durab Heal Monit 2017;11:91–147.

[8] Doebling, S.W., Farrar, C.R., Prime, M.B. and Shevitz DW. Damage Identification and Health Monitoring of Structural and Mechanical Systems from Changes in Their Vibration Characteristics: A Literature Review. (No. LA--13070-MS). Los Alamos Natl. Lab., NM (United States): 1996, p. 1–136.

[9] Doebling SW, Farrar CR, Prime MB. A summary review of vibration-based damage identification methods. Shock Vib Dig 1998;30:91–105.

[10] Montalvao D, Maia NMM, Ribeiro AMR. A Review of Vibration Based Structural Health Monitoring with Special Emphasis on Composite Materials. Shock Vib Dig 2006;38:295–324.

[11] Sinou J-J. A Review of Damage Detection and Health Monitoring of Mechanical Systems from Changes in the Measurement of Linear and Non-linear Vibrations. Mech Vib Meas Eff Control 2009:643–702.

[12] Maia NMM, Silva JMM. Theoretical and Experimental Modal Analysis. Taunton: Research Studies Press and John Wiley and Sons, Somerset; 1997.

[13] Guillaume P, Verboven P, Vanlanduit S PE. Multisine Excitations- New Developments and Applications in Modal Analysis. Proc 19th Int Modal Anal Conf (IMAC XIX) 2001;2:1543–9.

University of Hertfordshire UH

Identifying the optimum fuel cell current density range for a SOFC-GT hybrid power system

Adrian Felix[1*], Christos Kalyvas[1], Peter Thomas[1]

[1]*School of Physics, Engineering and Computer Science - University of Hertfordshire*

*Corresponding author: a.i.felix@herts.ac.uk

Solid oxide fuel cells and gas turbines can be combined to form a hybrid system with high thermodynamic efficiency and good transient load performance. The performance and reliability of the system depends on temperatures of the fluid streams and solid components at various points in the combined cycle. This study used a steady state mathematical model of the system to identify the optimum range of current density values in which temperature difference between air and fuel streams at the inlet and outlet of the fuel cell do not exceed the critical value of 100 K, and the corresponding voltage and efficiencies.

Keywords: hydrogen; SOFC; sustainable energy; transportation

Introduction

Solid oxide fuel cells are solid-state electrochemical devices that convert chemical energy of fuel into electrical energy with more than 65% efficiency at temperatures higher than 650^{o}C [1]. However, due to the slow rate of electrochemical reactions, they have poor response to transient load demands dynamic operating conditions which make them unsuitable for aircraft and automotive applications [2]. One solution to this is hybridising with a Brayton cycle gas turbine generator to form a system that combines the high efficiency of the SOFC and dynamic performance of the gas turbine [3]. The resulting Solid Oxide Fuel Cell-Gas Turbine (SOFC-GT) hybrid cycle, as shown in Figure 1, can give a combination of high efficiency from the SOFC and good response to transient loads of the GT.

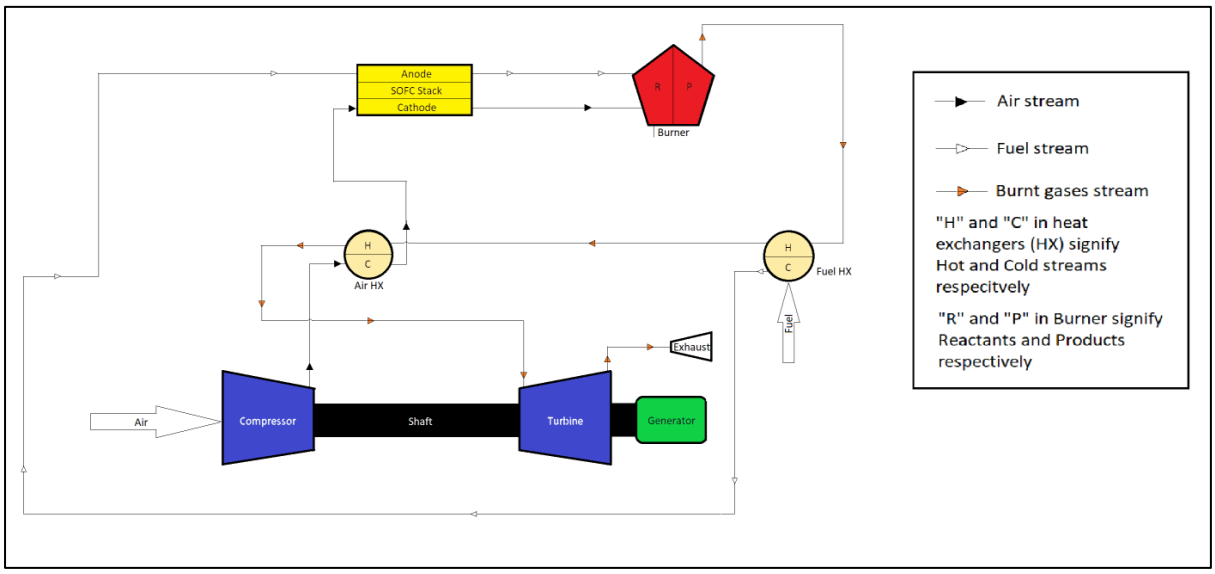

Figure 8: Schematic of a SOFC-GT hybrid system

It is the high operating temperatures of SOFCs that make them suitable for hybridisation with GTs, however, those high temperatures also make them prone to degradation under thermal stresses. It has been established that cell degradation exceeds critical levels if the temperature difference between fluid streams at the inlet and outlet of the SOFC channels exceed 100 K [1]. This increase in fluid stream temperature across the channels are caused by heat released from the electrochemical reaction between fuel and oxygen called polarisation losses. These losses are proportional to current drawn from the fuel cell which is conventionally expressed as area-specific current density [4].

This study aims to identify the range of current density values of a fuel cell in a SOFC-GT system where the minimum power required from the system is met and fluid stream temperature difference across the fuel cell does not exceed 100 K. The corresponding cell voltage and system efficiency for this range of operation were also recorded. To carry out the study, a mathematical model of the SOFC, compressor, turbine, burner, and heat exchangers that make up the system was made using mass and energy conservation equations.

Experimental

Each component that makes up the hybrid system was modelled as a control volume and mathematical equations for mass and energy balance in steady state were derived according to established literature [1], [5]. These equations were modelled on the MATLAB/Simulink environment to simulate the hybrid system.

Table 2: Model operating parameters

Parameter	Value
Pressure ratio	7
Isentropic efficiency of turbine and compressor	0.85
Air flowrate	0.50 g/s
Fuel (H_2) flowrate	0.003 g/s
Active surface area	400 cm^2
Number of cells in stack	120
Air heat exchanger effectiveness	0.75
Fuel heat exchanger effectiveness	0.50

Operating parameters used for the hybrid system model are listed in Table 1. Electrochemical parameters used for the fuel cell model were taken from previous experimental data and models [5]. Keeping all other parameters constant, current density of the fuel cell was varied from 1 to 4.5 A/cm^2, where the polarisation curve is in its linear region, and this is the most common operating range for any SOFC.

Results and discussion

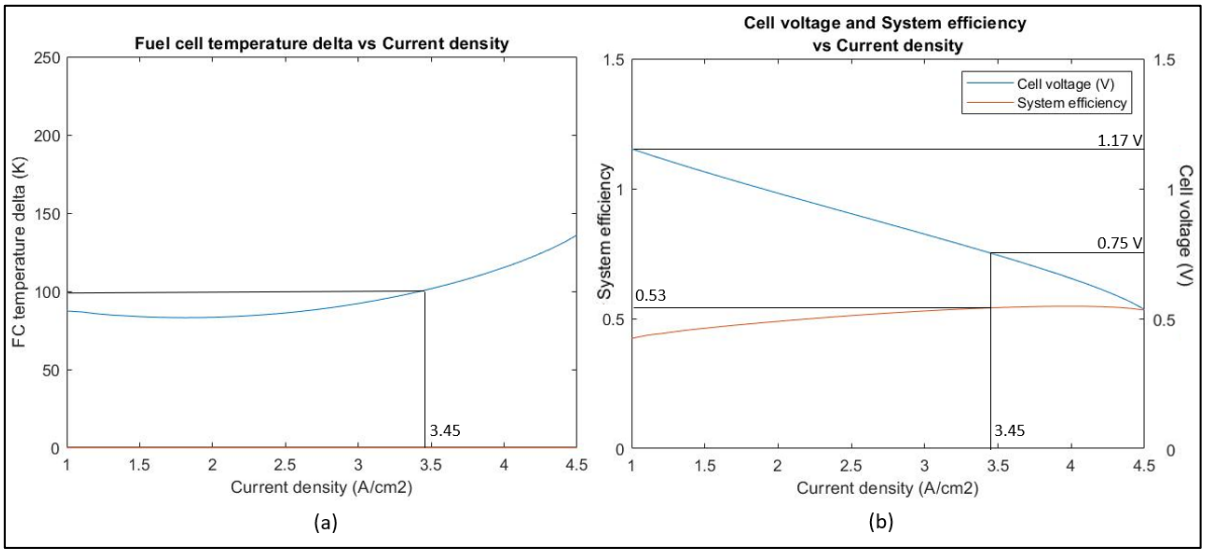

Figure 2: Steady-state model results

As seen from Figure 1 (a), the upper limit of current density was found to be 3.45 A/cm^2. Therefore, the desired operating range for the fuel cell – where the fuel cell is in linear region of polarisation curve and temperature delta is within acceptable limits – was found to be between current density 1 A/cm^2 and 3.45 A/cm2. As shown by Figure 1 (b), the corresponding per-cell voltage range is between 1.17 V and 0.75 V. Interestingly, thermal efficiency of the system was found to peak at 53% and plateau at that value even at higher current densities. This can be attributed to the larger polarization losses at higher current densities resulting in more energy wastage in the form of heat.

Conclusion

A steady-state mathematical model of a SOFC-GT hybrid system was implemented on MATLAB/Simulink which was run at constant fuel and air flowrates, but varying current density. It was found that the safe range of current density values for the system under given flow conditions was between 1 A/cm^2 and 3.45 A/cm^2. Voltage per cell of the SOFC was found to be between 1.17 V and 0.75 V and thermal efficiency of the system peaked at 53%. This model can be used to perform a similar study on other SOFC-GT systems of similar configuration by simply varying the parameter values.

References

[1] K. Kendall and M. Kendall, *High-Temperature Solid Oxide Fuel Cells for the 21st Century: Fundamentals, Design and Applications: Second Edition*. 2015.

[2] N. K. Borer *et al.*, "Overcoming the adoption barrier to electric flight," *54th AIAA Aerosp. Sci. Meet.*, vol. 0, no. January, 2016.

[3] N. K. Borer, S. C. Geuther, B. L. Litherland, and L. Kohlman, "Design and performance of a hybrid-electric fuel cell flight demonstration concept," *2018 Aviat. Technol. Integr. Oper. Conf.*, pp. 1–15, 2018.

[4] A. L. Dicks and D. A. J. Rand, "Solid Oxide Fuel Cells," in *Fuel Cell Systems Explained*, 2018, pp. 235–261.

[5] J. Milewski, K. Świrski, M. Santarelli, and P. Leone, "Advanced methods of solid oxide fuel cell modeling," *Green Energy and Technology*, vol. 40. pp. 1–12, 2014.

Metal-only Planar Lens for Wireless Communications

Qi Luo[1], Wei Hu[2]

[1]University of Hertfordshire, UK; [2]Xidian University, China

Keywords: Lens, antenna, transmitarray

The lens is known for focusing or dispersing a light beam through refraction. In wireless communication, the lens is used to increase the directivity of the radio frequency (RF) front end [1]. For example, the directivity of the antenna can be improved by more than 10 dB by using a lens. The traditional lens has a curvature profile and is made of dielectric materials. Transmitarray (TA), which is also referred to as planar lens, combines the features of lens and phased array antenna [2]. A TA normally consists of a large number of periodic elements printed on printed circuit boards (PCBs) and is widely used in satellite communication systems and radar systems.

In this paper, we present our recent research progress in using metal to realize a planar lens [3]. As the planar lens is made of metal, it is very robust and can be deployed to operate in harsh environments and is suitable for space applications. Moreover, the fabrication does not include chemical processing as the PCBs, it is also more environmentally friendly and can be easily recycled. Figure 1 demonstrates the design concept of the metal-only lens that works at the centre frequency of 8.5 GHz. A photo of the fabricated prototype under measurement in the anechoic chamber is also shown in Figure 1. Be noted that, for such a planar lens, there is always a limitation on the operation bandwidth.

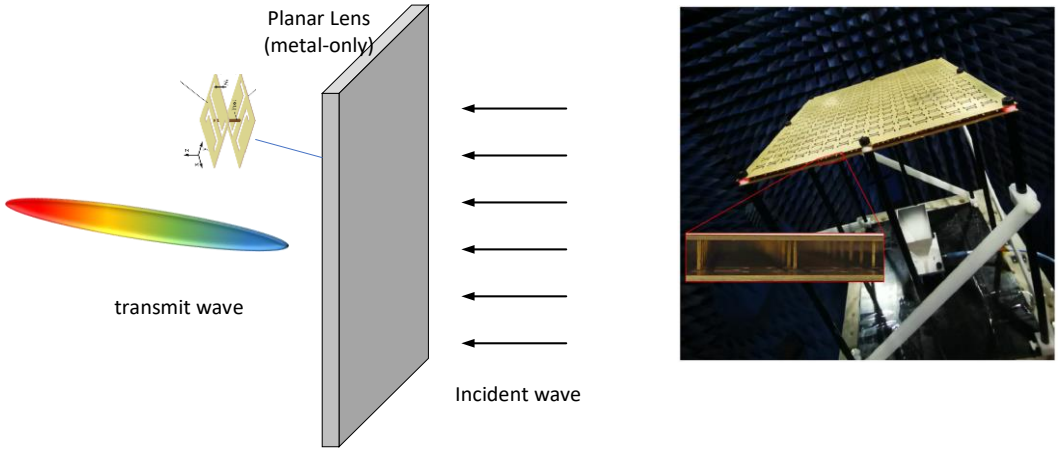

Fig. 1 – The concept of the metal-only planar lens (left) and the prototype under measurement in the anechoic chamber. This lens operates at the centre frequency of 8.5 GHz.

References

[1] Luo, Q., Gao, S., Liu, W. and Gu, C. (2019). Other Types of Low-cost Smart Antennas. In Low-cost Smart Antennas (eds Q. Luo, S. Gao, W. Liu and C. Gu).

[2] Q. Luo, S. Gao, M. Sobhy, and X. Yang, “Wideband transmitarray with reduced profile,” IEEE Antennas Wireless Propag. Lett., vol. 17, no. 3,

pp. 450–453, Mar. 2018.

[3] W. Hu et al., "A Wideband Metal-Only Transmitarray With Two-Layer Configuration," in IEEE Antennas and Wireless Propagation Letters, vol. 20, no. 7, pp. 1347-1351, July 2021

University of Hertfordshire UH

Systematic Evaluation of Mineral Wastes for Use in Cementitious Binders

Surya Maruthupandian[1], Napoleana Anna Chaliasou[1], Antonios Kanellopoulos[1]

[1] University of Hertfordshire

Keywords: Mine tailing, Mineral waste, Cementitious binders

Mineral waste can be defined as the *"residues, tailings or other non-valuable material produced after the extraction and processing of material to form mineral products"* [1]. The mineral wastes from ore and mineral processing show a chemical composition similar to that of Portland cement. A past studies have also reported the cementitious properties of mineral wastes [2]. However, certain limitations with regards to their usage are also reported including high crystallinity and inert nature [3]. Some of the past studies [4] indicate a high potential for use of mineral wastes in cementitious binders after some processing to convert the crystalline phases to amorphous phases. This process is known as activation. However, existing research also points out the lack of a standard method of assessment for the reactivity of these binders and absence of an activation method or mix design procedure which is more systematic rather than trial and error is evident.

The present research focuses on developing a more systematic method of characterisation of the materials and hence determine the suitable method of activation. The study was performed on mineral waste from two different sources. The mine tailing used in the study, is a by-product of graphite mining and was provided by Talga Resources. The mine tailing is predominantly silicate and was provided in dry state. The silt used in the study is from the Eco Aggregates plant in Welwyn Garden City, United Kingdom. The silt produced is a by-product from a construction waste recycling plant. Both the materials had a few lumps which were broken, and oven dried at 80ºC for 24 hours, sieved through 600 µm sieve and used for further tests. The mineral phases of the mineral wastes were initially determined using XRD as shown in Fig. 1.

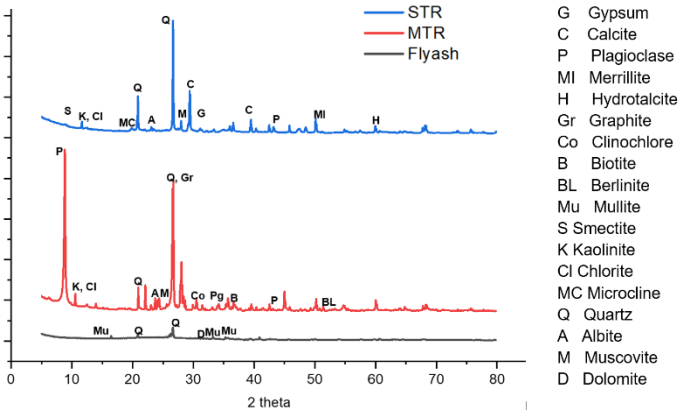

Fig. 1 – XRD phases of mine tailing, silt and Fly ash

Based on the phases the activation was carried out using thermal activation and mechanical activation. The mineral wastes after activation were characterised using microscopic studies and mineralogy, dissolution of Si and Al, pozzolanic activity by R3 tests. Depending on the findings of the study suitable method for preparation of cementitious is proposed.

References

[1] D. J. Harrison *et al.*, "Utilisation of mineral waste: case studies," p. 92pp, 2002, [Online]. Available: http://nora.nerc.ac.uk/9018/.

[2] S. Solismaa *et al.*, "Valorization of finnish mining tailings for use in the ceramics industry," *Bull. Geol. Soc. Finl.*, vol. 90, no. 1, 2018, doi: 10.17741/bgsf/90.1.002.

[3] R. Argane, M. Benzaazoua, R. Hakkou, and A. Bouamrane, "A comparative study on the practical use of low sulfide base-metal tailings as aggregates for rendering and masonry mortars," *J. Clean. Prod.*, vol. 112, pp. 914–925, 2016, doi: 10.1016/j.jclepro.2015.06.004.

[4] J. Kiventerä, P. Perumal, J. Yliniemi, and M. Illikainen, "Mine tailings as a raw material in alkali activation: A review," *Int. J. Miner. Metall. Mater.*, vol. 27, no. 8, pp. 1009–1020, 2020, doi: 10.1007/s12613-020-2129-6.

University of Hertfordshire UH

A Machine Learning Pattern for CNNs with Mixed-Feature Modes

Aklil Kiflay[1], **Athanasios Tsokanos**[1] **Raimund Kirner**[1]

[1]*Department of Computer Science, University of Hertfordshire, Hatfield, United Kingdom*

Convolutional Neural Network (CNN) **is a** ***Deep Neural Network*** **(DNN) that is well-suited to local feature extraction. DNN learns features useful for a particular learning problem from raw input data, thus reducing reliance on domain experts. However, automatic learning of features via DNN comes at a cost, as it requires relatively high computing resources. An approach to reduce DNN's resource requirement is to use additional hand-crafted features as input, providing a compromise between automation and resource demand. In this paper, we present a hybrid DNN with mixed-mode features, and demonstrate its application in intrusion detection using** ***UNSWNB15*** **dataset.**

Keywords: Neural network; intrusion detection

Introduction

While conventional classification approaches rely on hand-crafted features derived from raw input data, DNNs can extract features with limited involvement of a domain expert. However, the automatic learning of features via DNN comes at a cost, as it requires relatively high memory and computing resources (increased number of layers and neurons per layer). Thus, an approach to reduce the required memory and computing resources of DNN is to use additional hand-crafted features as input, providing a compromise between automation and resource demand.

In this research we present a machine learning pattern for CNNs with mixed-mode features, i.e., using a combination of automatically learned and hand-crafted features. Fig. 1 shows the standard architecture of a CNN [1], where $CONV_1$ represents a combination of convolutional layers for feature extraction and pooling layers for data compression. The key feature of a CNN is that the convolutional layers use local filters that are suited to learn local features. In addition, CNNs feature standard fully-connected neural network layers to achieve the classification based on feature combination, denoted as $FCNN_1$ The idea of the mixed-feature mode CNN pattern is to use a combination of features learned automatically from the raw input data in combination with hand-crafted provided by a domain expert, as shown in in Fig. 2.

Considering the special architecture of CNNs, we feed the hand-crafted features directly in the fully connected neural network $FCNN_1$, bypassing the CNN's feature extraction layers $CONV_1$. Note that in Fig. 2 we also show that this machine learning pattern can be used by more advanced CNN-based architectures, for example, as shown in the figure, with two competitive feature learning stages $FCNN_1$ and $FCNN_2$, and two competitive fully-connected neural network stages $CONV_1$ and $CONV_2$.

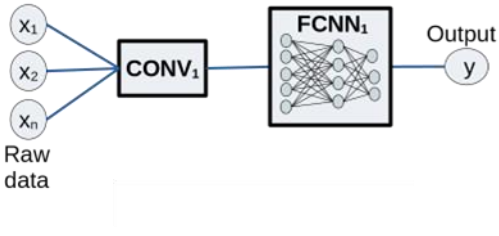

Fig. 1. A standard CNN

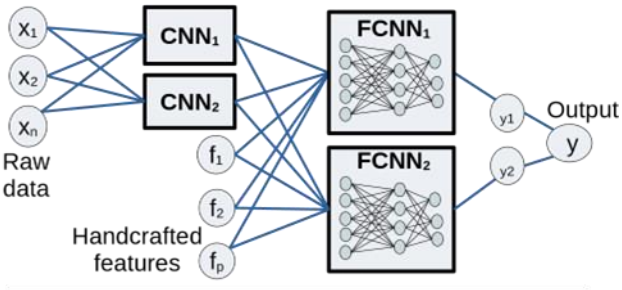

Fig. 2. A hybrid CNN Hand-crafted features

Our motivation for this machine learning pattern for CNNs with mixed-mode features comes from a concrete use case, a *network intrusion detection systems* (NIDS) [3]. The particular problem with building NIDS systems based on DNN is that there is typically only limited amount of real attack traffic available, while at the same time small variations of existing attack traffic can be used to deceive the NIDS. Using 1dimensional CNNs is generally a useful approach for NIDS, as with CNNs the filter-based focuses on local traffic patterns, providing more robustness against variations of the attack traffic. Using the proposed machine learning pattern for CNNs with

mixed-mode features allows us to add additional hand-crafted features specifically designed to increase the robustness of the NIDS.

The main function of an NIDS is to enable the quick discovery of potential cyber-attacks. This in turn shortens the dwell time of cyber threats inside a network. One way to discover cyber-attacks quickly is by designing NIDS frameworks with low total attack detection time. However, the majority of ML-based NIDS frameworks highly depend on a feature engineering step, which typically comes in the form of separate feature extraction and feature selection pipelines. To this effect, different network traffic feature engineering approaches have been explored by NIDS researchers in the past. However, previous works mainly focus on increasing cyber-attack detection accuracy, and minimizing the rate of false alarms. As a result, there has been limited effort on approaches that decrease the overall time taken by an NIDS to detect cyber-attacks. As a way of addressing this gap, we use one dimensional Convolutional Neural Network (1D CNN) to design an end-to-end NIDS framework, thus avoiding the need for separate feature engineering pipelines, while at the same time maintaining domain knowledge through the use of hand-crafted features as input.

Experiment

The experiment was conducted using TensorFlow 2.8 running on NVIDIA GeForce RTX 2060 GPU, and Ubuntu 20.04 operating system. The *UNSW-NB15* [4] dataset was used for model training and evaluation. *UNSW-NB15* consists of network packet flows each with 47 features extracted from a 100 GB raw packet capture. It contains representative samples of modern normal traffic and nine major families of cyberattacks. Out of the *UNSW-NB15* dataset, 30% samples were set aside as a test set. From the remaining 70% samples, 20% of them were used for validation and the rest for training. Initially, data pre-processing (encoding and normalization) was performed on the dataset resulting in an input shape of $(196,1)$.

The hybrid model architecture takes two types of data inputs. While the two CNN layers take the original dataset samples as input, the FCCNs use both hand-crafted features and the CNN outputs. To prepare the hand-crafted features, a random forest classifier was used to select the most important features of the dataset. A feature's importance is calculated based on its contribution in the classification output of the random forest classifier. In this way, the contribution of individual traffic features was evaluated and ranked from high to low. While monitoring classification accuracy, low-ranked features were recursively excluded to identify the most important ones. Low-ranked features whose exclusion does not result in a classification accuracy of less than 90% were discarded. A feature importance threshold of 0.31 resulted in 13 most important features. The FCNNs take these 13 pre-identified features and the outputs of the convolution layers as input.

For the CNN layers, convolutions with 64 filters, and kernel size of 5 were used, followed by 2 max pooling layer compressing the convolution output by half. Batch normalization was applied on the outputs of each max pooling layers with batch size of 32. Consequently, the input to the FCNNs was formed from the CNN deep features, and the most important features pre-selected using random forest. In each FCNN block, two dense layers with 64 and 32 neurons were used. After the 64-neuron dense layer, a dropout layer with a dropout rate of 0.25 was used to reduce over-fitting. While Relu activation function was used in the hidden layers, sigmoid was used in the output layer. Binary cross entropy and Adam were used as a loss function and an optimizer algorithm, respectively. The model was trained for 200 epochs. Finally, the results from the two FCNNs were combined to obtain the final classification output.

Results

Fig. 3 shows the training and validation accuracy. With a limited fluctuation, the result shows that both training and validation accuracies follow the same trend, maintaining more than 93% accuracy from around epoch 25. This suggests that the model has very limited over-fitting problem. Furthermore, this was also confirmed by evaluating the model after training. An accuracy of 93.5% was obtained by evaluating the model on the test set.

Training and validation accuracy

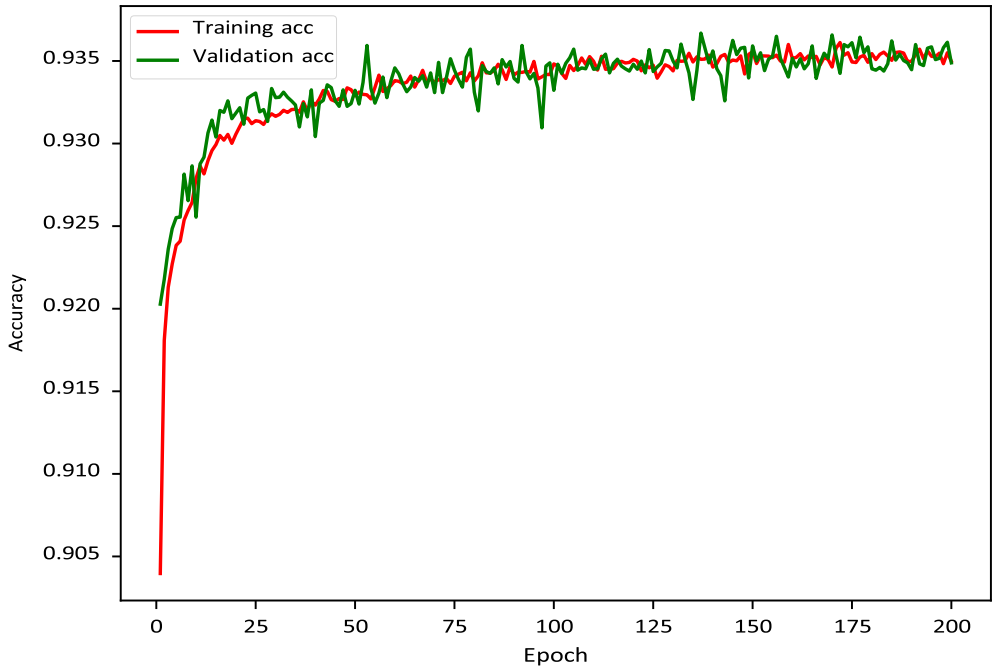

Fig. 3 – Accuracy

Conclusion

The use of CNNs with mixed-mode features can help in reducing model complexity, resulting in reduced computing resource consumption. Furthermore, using handcrafted features to supplement CNN extracted deep features can increase classification accuracy. In conclusion, although various hybrid DNN architectures need to be explored, the proposed machine learning pattern with mixed-mode features is an application-independent pattern and thus might be also beneficial for other DNN problems.

References

[1] LeCun, Y. *et al.* (2015). Nature **521**(7553), 436
[2] Liu, P. (2019). Proceedings of 11th Int. Conf. on Computer and Automation Engineering, 62
[3] Zhao, J. *et al.* (2021). Information Fusion **72**, 22
[4] Moustafa, N. *et al.* (2015). 2015 military communications and information systems conference (MilCIS). IEEE, 1

University of Hertfordshire UH

Antimicrobial efficacy and safety of G-UV and UV-enhanced nanoparticles

Patrick Irigo[1], G Ren[2]

[1]University of Hertfordshire

Abstract

Antimicrobial NPs (nanoparticles) can inactivate up to 99.997% of pathogens including: viruses, gram-positive and gram-negative bacteria and fungi. The project aims to explore and validate the efficacy of G-UV (germicidal ultraviolet) and UV-R (UV radiation) stimulated NPs. This would be carried out using numerical modelling and machine learning to predict the UV wavelength and dose required to generate sufficient synergistic microbicidal action against pathogens.
Keywords: Germicidal ultraviolet, nanoparticles, pathogens, COVID-19, irradiation modelling.

Background and Project Relevance

Airborne pathogens are known to be the major causes of pandemics due to the ease of transmission and transport through air. A good example is the COVID-19 (SARS-CoV-2) virus which is highly infectious and lethal. As of May 2021, a statement from WHO reported a record high 5 million verified deaths due in 213 countries **Error! Reference source not found.**. The primary mode of transmission is through direct contact (nose, eyes or mouth), with aerosolised respiratory droplets from an infected patient which can be produced by coughing, sneezing or talking. The contact routes created by inert materials can serve as vectors of transmission following contact with the respiratory tracts of an infected person, this introduces a substantial risk in regards to transmission as they are difficult to locate **Error! Reference source not found.**.

G-UV can be used to disinfect air, water, and solid surfaces although surface disinfection is restricted by micro-shadows and absorption by protective layers, therefore, it is advisable that G-UV devices are used as a supplemental infection control strategy. It is believed that the substitution of human-safe far-UVC light replacing conventional mercury-line UVGI Ultraviolet-C light, is the most disruptive technology-based non-pharmaceutical pandemic countermeasure in human history. Hence this study will Investigate the efficacy and safety of "potentially" safe Far-UVC for disinfection. UV-R activated microbicidal NPs can be integrated into the design of anti-microbial fabrics (linen, merino wool, and hem) and air filters including facemasks and HEPA (high efficiency particulate air) filters, to enhance the microbicidal performance and control the spread of infections, particularly in healthcare settings **Error! Reference source not found.**.

Methodology

The objectives of this study can be divided into three main stages.
Stage 1 involves the design of a fully automated UV LED test rig to investigate three practical areas such as:

a. The microbial reduction levels using varying sources and wavelengths (222nm and 365nm),
b. The spatial distribution and intensity on different target surfaces as seen in (*Figure 9*),
c. The dose needed to trigger photoreaction in nanoparticles.

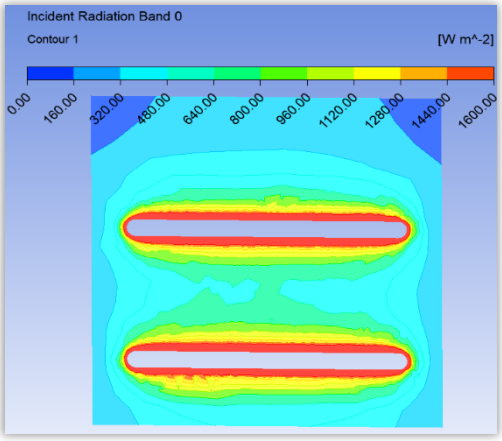

Figure 9. UV-R spatial distribution (dual lamp setup).

Stage 2 involves validating the experimental studies using numerical modelling software. The irradiation model would be calculated using ANSYS Fluent solver with user-defined functions (UDF) integrated to determine the spatial distribution and intensity at varying UV-R wavelengths, intensities and arrangements. The spatial distribution of UV-R. The spatial distribution was solved using the radiative transfer equation (RTE) and the DO method (Discrete Ordinates), in addition to the three conservation laws,
is determined by calculating the essential functional parameters including: the lamp and fixture geometry, the UV output of the lamp, the reflection, refraction and absorpition from the surfaces in the vicinity of the lamp.

Equation 1.

$$\nabla\cdot\left(\left(I_\lambda(\vec{r},\vec{s})\,\vec{s}\right) + (\alpha_\lambda + \sigma_s)\, I_\lambda\,(\vec{r},\vec{s})\right) = \alpha_\lambda n^2 I_{b\lambda} + \frac{\sigma_s}{4\pi}\int_0^{4\pi} I_\lambda(\vec{r},\vec{s}')\,\varphi\,(\vec{s},\vec{s}')\,d\Omega'$$

Where: $\vec{r}$ is position vector, $\vec{s}$ is direction vector, $\vec{s}'$ is scattering direction vector, s is path length, α_λ is spectral absorption coefficient, n is refractive index, σ_s is scattering coefficient, $I_{b\lambda}$ is black body intensity, I_λ is radiation intensity which depends on position and direction, λ is wavelength, ϕ is phase function and Ω' is solid angle. Irradiation modelling is a key consideration when looking to adapt UV systems to precise disinfection processes and for the disinfection of the desired microorganisms, and it also helps to provide a foundation for sizing UV disinfection gadgets.

Stage 3 involves an appraisal of the efficacy and safety of G-UV and NPs for bioburden reduction and its suitability as counter-measure to prevent or control future pandemics. This involves investigating effective proactive methods of implementing the current advancements in nanotechnology augmented as an effective adjunct technology with G-UV, to minimise the risk of transmission and proffer safe routes to the resumption of public gatherings.

Results

The microbicidal properties and applications of G-UV and UV-R stimulated NPs will be established in this paper by studying the required dose needed to the induce their antimicrobial action and achieve certain levels of microbial reduction illustrated in (*Figure 10* & *Figure 11*). This study will also seek effective proactive methods of implementing the current advancements in nanotechnology augmented as an effective adjunct technology with G-UV, in order to minimise the risk of pathogen transmission and proffer safe routes in the ongoing return of public gatherings.

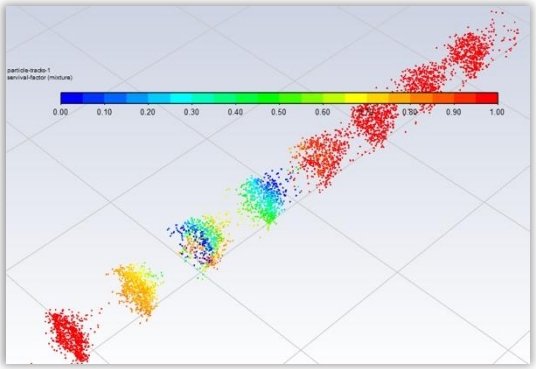

Figure 10. Survival fraction for SARS-CoV-2 (Z = 0.05526 m^2/J) in a uniform lamp configurations (η = 90%).

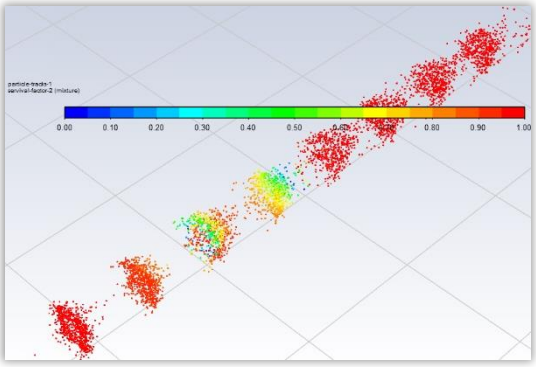

Figure 11. Survival fraction for SARS-CoV-2 (Z = 0.05526 m^2/J) in a uniform lamp configurations (η = 90%).

Conclusion

The analysed data will be integrated as the basis for an appraisal of the efficacy and safety of G-UV and NPs for bioburden reduction and as a suitable counter-measure to inhibit the CoV outbreak, which could potentially deliver a supplementary solution for enhancing indoor air quality (IAQ) within residential and public spaces **Error! Reference source not found.**.

University of Hertfordshire UH

Reference list

[1]. WHO (2021) WHO Coronavirus (COVID-19) Dashboard. WHO Coronavirus (COVID-19) Dashboard With Vaccination Data, WHO. Available at: https://covid19.who.int/ (Accessed: 4 May 2021).

[2]. Aydogdu, M. O., Altun, E., Chung, E., Ren, G., et al. (2021) 'Surface interactions and viability of coronaviruses', Journal of The Royal Society Interface, 18(174), p. 20200798. doi: 10.1098/rsif.2020.0798.

[3]. Matharu, R. K., Ciric, L., Ren, G. and Edirisinghe, M. (2020) 'Comparative study of the antimicrobial effects of tungsten nanoparticles and tungsten nanocomposite fibres on hospital acquired bacterial and viral pathogens', Nanomaterials, 10(6). doi: 10.3390/nano10061017.

Effects of Sensor Spacing and Material Thickness of Al 6082-T6 using Acousto-Ultrasonics Technique

Kumar Shantanu Prasad[1], Gbanaibolou Jombo[1], Sikiru Oluwarotimi Ismail[1], Yong Kang Chen[1], Hom Nath Dhakal[2]

[1]Centre for Engineering Research, School of Physics, Engineering and Computer Science, University of Hertfordshire, UK; [2]Advanced Materials and Manufacturing (AMM) Research Group, School of Mechanical and Design Engineering, University of Portsmouth, UK

Keywords: Acousto-Ultrasonics technique, Non- destructive testing, Lamb waves

Acousto-ultrasonic waves, which are similar to acoustic emissions, are generally ultrasonic in nature. The acoustic emission method depends on loading to excite spontaneous waves, whereas acousto-ultrasonics technique (AUT) does not require any passive loadings. AUT differs mainly because its waves begin and generate eternally by a pulsed source [1]. Acousto-ultrasonics, as a technique for non-destructive evaluation of structures, provides the ability to detect and characterise defects, damage responses and variation in properties of materials. AUT uses analysis of simulated stress waves generated through localised ultrasonic excitation for detecting and mapping variations of mechanical properties. The accuracy of acousto-ultrasonics testing depends on many factors, amongst which are sensor spacing and the effect of material thickness on lamb wave mode propagation. Therefore, this present study mainly focused on the effects of relative spacing of the transducer and the thickness of Al 6082-T6 specimen on AUT implementation. The Stress Wave Factors (SWF) studied and utilised for the work was based on the report of Vary [1]. From the results obtained, it was evident that, (Fig. 1), the peak voltage varies with maximum of 1931 mV and 1197 mV at 60 mm and 120 mm sensor spacing, respectively in the frequency range of 100 kHz to 400 kHz. Other factors that were relevant to the test technique can be subsequently grouped: coupling (contact pressure and type of couplant), emitted ultrasonic pulse (emitter transducer type, pulse energy and pulse or burst mode), received signal (receiving transducer type, gain and signal gating) as well as relative spacing of the transducers [2]. When all the aforementioned parameters were kept constant, then the AUT depended on material variation in the Al 6082-T6 specimen. Parameters that probably characterised the material include structure of the material (morphology, defects and internal interfaces) and geometric effects (extent of the test specimen and thickness of the test specimen) [3]. These quantities will be further studied on the same sample, as the investigation continues or a recommended future work.

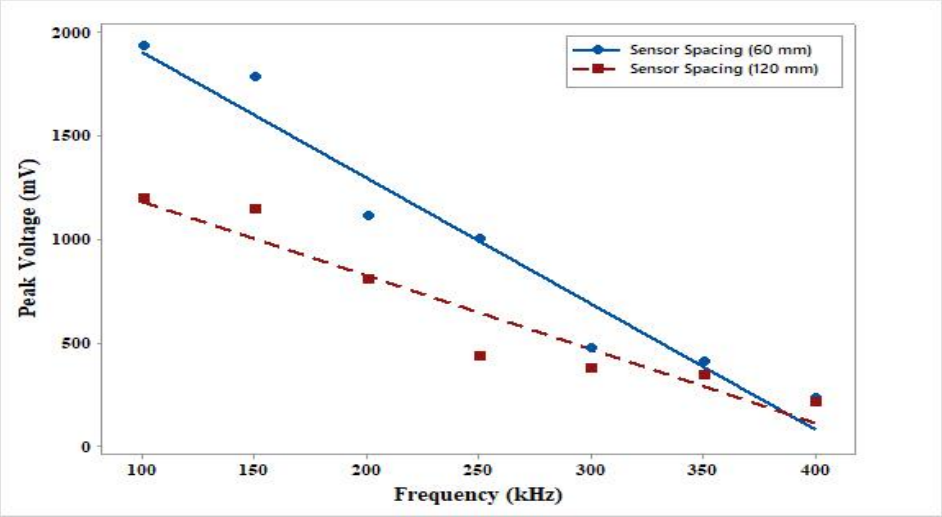

Fig. 12- Peak Voltage at different sensor spacing

References

[1] Vary A. (1988) Acousto-Ultrasonics **1**(1) 28

[2] Bhatt, M. and Hogg, P. J. (1988) NDT International **21**(10) 274

[3] Kautz, H. E. (1987) NASA Lewis Research Centre Cleveland, OH, United States, New York

University of Hertfordshire UH

Protostellar radio variability: A window to high-energy processes in young stars through the eyes of ALMA, VLA, and VLBA

Jaime Vargas-González[1], Jan Forbrich[1] S. Dzib[2] J. Bally[3] V. Rivilla[4,5]

[1]*Centre for Astrophysics Research, University of Hertfordshire, UK;*
[2]*Max-Planck-Institut für Radioastronomie, Germany;*
[3]*Center for Astrophysics and Space Astronomy, University of Colorado, USA;*
[4]*CSIC-INTA, Spain;*
[5]*INAF, Italy*

Keywords: Astrophysics, stars, radio interferometry

Low-mass protostars (<2 Solar masses) are widely known for their intense magnetic activity and highly variable luminosity as revealed by X-ray and radio observations [1]. At their early evolutionary stages (≤10^6 years, just a thousandth of the Sun's age) they present energetic flare events orders of magnitude more intense than Solar flares. These high-energy processes thus represent a crucial ingredient in the evolution of protostellar surrounding and ultimately the evolution of planetary systems. These processes can be traced by nonthermal radio emission from (gyro)-synchrotron radiation as a result of electrons gyrating along magnetic field lines in the protostellar surface. In this context, we are presenting unprecedented new insights into the radio time-domain of protostars, studying their variability at radio frequencies using the most sophisticated radio facilities on Earth such as the Very Large Array (VLA), the Atacama Large Millimeter/submillimeter Array (ALMA), and the Very Long Baseline Array (VLBA). In order to efficiently observe hundreds of protostars we have looked at the Orion Nebula Cluster (ONC), the richest young stellar cluster in the Solar neighborhood. We started with a large program using the VLA observing at centimeterwavelengths, revealing hundreds of sources at high-spatial resolution, studied their radio luminosity and variability on timescale from minutes to years (see Fig. 1), and additionally discovered fast motions from non-stellar radio features in the observed field [2]. We then set the first systematic search for strong radio flares at higher-frequencies using ALMA at millimeter-wavelengths finding a wide range of variability in a sample of more than 100 sources, while also discussing the advantages and limitations for variability studies using our method on this dataset, particularly towards complex regions such as the ONC. Finally, we conducted a multi-epoch VLBA survey for nonthermal radio emission from protostars [3]. This dataset allow us to obtain intensity and polarisation information at any time resolution down to a few seconds in an exceedingly more efficient way only achievable with the VLBA. We studied a large sample of VLBA light curves from seconds to years where we find strong variability on timescales of days and even within the individual epochs of a few hours.

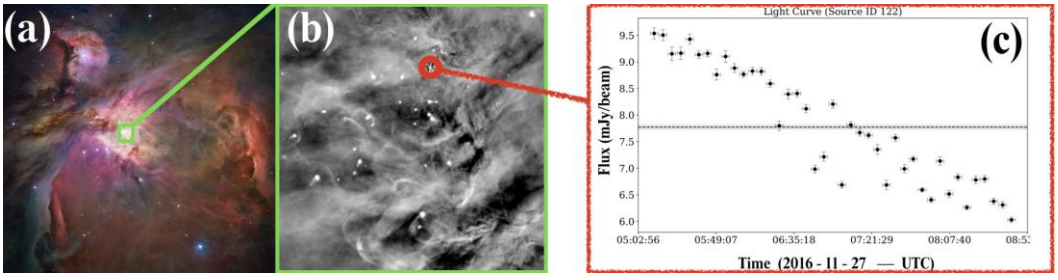

Fig. 1 – **(a)** *Optical image of the ONC from the HST archive (Credit: NASA, ESA, M. Robberto, and the HST Orion Treasury Project Team).* **(b)** *Section of a VLA radio map covering the field shown in green in the left image.* **(c)***Light curve of one source indicating its decreasing radio flux during the observations.*

References

[1] Feigelson, E. *et al.* (1999). ARA&A **37**, 363
[2] Vargas-González, J. *et al.* (2021). MNRAS **506**, 3169
[3] Forbrich, J. *et al.* (2021). ApJ **906**, 23

Detection of plant damage using an E-nose

Shavika Rastogi[1,2], Samuel Sutton[2], Ritesh Kumar[2,3], Michael Schmuker[2]

[1]International Centre for Neuromorphic Systems, Western Sydney University, Sydney, AU ;
[2]Biocomputation Group, University of Hertfordshire, Hatfield, UK ;
[3]CSIR-Central Scientific Instruments Organisation, Chandigarh, India

Keywords: E-nose, MOX sensors, Plant identification

Herbaceous plants are often damaged by pests, with negative outcomes like decrease in growth or even plant death. Early detection of plant damage could help trigger countermeasures early. Different plants release different volatiles while being cut [1]. Identification of the characteristic volatiles could help identifying the damaged plant. In this preliminary study we investigate whether metal-oxide (MOX) gas sensors detect plant damage in an uncontrolled environment, and if they can discriminate the volatiles specific to different plants.

A desktop fan was used to generate an airstream that could transport volatiles to an enose (Fig. 1A). Volatiles were generated by cutting five different herbs: Parsley, Thyme, Mint, Rosemary and Basil (all potted, ASDA Hatfield) at 0.1 m distance from an rapid-responding e-nose designed in our lab [2] (Fig. 1B). We used four different fan speeds and two different fan distances (0.5 m and 1 m) to investigate the influence of different levels of turbulence in odour transport on the detection and identification of volatiles.

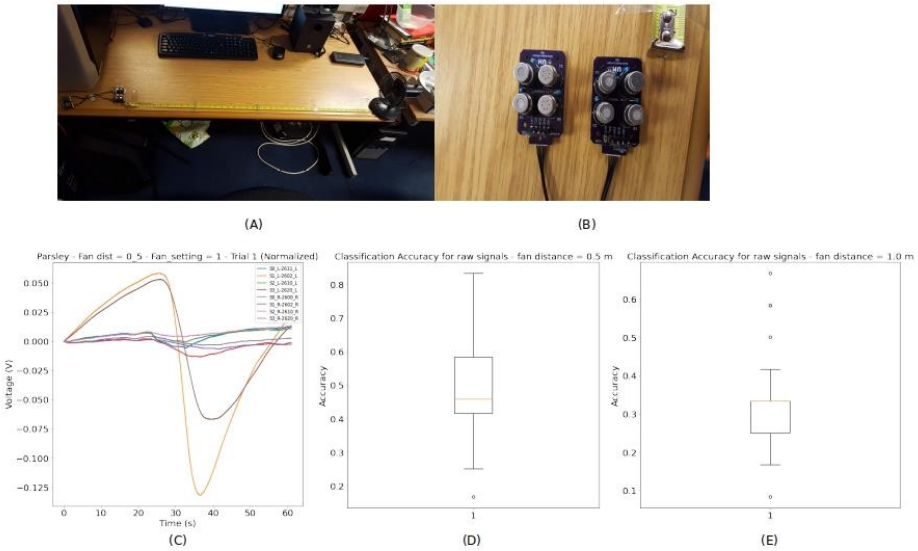

Fig. 1 – (A) Experimental setup (B) E-nose sensor platform (C) Normalised raw data for Parsley herb (8 sensors). D,E) Linear SVM classification accuracy for fan distance (D) 0.5 m (E) 1.0 m.

Results:

Fig. 1C shows the exemplar e-nose recordings. Voltage recordings were normalised by subtracting the sample value at t=0 s from all samples. Plants were being cut at t=20 s. The change in sensor signal after 20 s indicates the detection of plant volatiles. The pattern of different relative response magnitudes across sensors may hold information about the identity of the plant. We trained a linear SVM to discriminate between signals generated from different plants across 4 fan speeds. Median recognition accuracy for d=0.5 m was 0.46 ([0.42,0.58] 1st/3rd quartile range, 80/20 random train/test split, 50 repeats; Fig. 1D). There was considerable variability, and the median accuracies were only moderately different from random choice (0.2). At fan distance d=1 m accuracy was reduced to 0.33 ([0.25,0.33], Fig. 1E), potentially due to the increased intermittency of the flow.

Conclusion and outlook:

Our in-house MOX sensor e-nose can detect volatiles generated by plants upon physical damage. Plant recognition accuracy was moderate and adversely affected by increased intermittency of the flow. In the future we aim to increase the invariance to intermittent flow by selecting transient features like e.g. “bouts” of odor encounters [3], that might improve recognition accuracy in uncontrolled conditions.

References:

[1] Pickett J.A. et al., in Chemical Ecology: From Gene to Ecosystem (eds. M Dicke and W Takken), p. 161-173. Springer (2006).
[2] Drix D. et al. ACS Sensors 6(3), 688-692 (2021).
[3] Schmuker, M. et al. Sensors Actuators B Chem 235, 636–646 (2016).

University of Hertfordshire UH

The use of BASHTI as an organic ACL fixation technique

Narges Ghias[1], Amir Nourani[1], Mahdi Mohseni[1], Hossein Korani[1], Hadi Moeinnia[1], Amirhossein Borjali[1], Mahmoud Chizari[2]*

[1] Department of Mechanical engineering, Sharif University of Technology, Tehran, IR
[2] School of Engineering and Computer Sciences, University of Hertfordshire, College Ln, Hatfield AL10 9AB, UK
*corresponding author: m.chizari@herts.ac.uk

Abstract: This study aimed to investigate the effect of graft size on the strength of reconstructed ACL using BASHTI technique. 20 laboratory samples of BASHTI fixation were built using bovine digital tendons in four different sizes and artificial bones while other geometrical parameters were selected the same for all of the samples. A loading scenario simulating the ACL real condition was used to observe the fixation strength. The results showed that BASHTI is an acceptable fixation method for ACL reconstruction. Also, it was observed that the graft size has a significant effect on the biomechanical properties of this fixation method.

Keywords: BASHTI technique, ACL reconstruction, Ligament size, Fixation strength

Introduction

Anterior cruciate ligament (ACL) injury is common, especially between heavy sports athletes. Different techniques have been used for the fixation of the ACL graft. Most of these techniques use an external implant. There are problems associated with these treatments such as tendon twist, possible impingement [1], or tunnel enlargement [2]. In 2015, a new method was introduced called bone and site hold tendon inside (BASHTI) technique [3]. BASHTI is an organic and implant-less ACL reconstruction method that all of the components of the fixation comes from the human body. This technique mainly uses the patient's tibia bone instead of the interference screw to build the fixation [3] (Figure 1). As a result, there is no need for high-cost external implants such as an interference screw. Recent studies investigate using sheathed core bone plug for this fixation and increasing the reliability because although it could have some disadvantages such as ultimate load to failure and equivalent stiffness, it is hard to insert the block into the structure without the sheaths. Also, one of the failure modes in BASHTI technique is the fracture of the central core during the insertion procedure; using the sheathed core bone plug decreases the possibility of this [4].

Figure 13. BASHTI fixation Model

Another study discovers the effect of frequency of insertion on the maximum shear strength of the structure, in which two insertion methods were compared; a group of specimens was inserted using a hand-hammer, and another group was inserted using an auto hammer. The results indicated that the maximum shear strength was higher in the specimens, in which a hand-hammer was used. It shows that the maximum shear strength is influenced by the frequency of insertion. BASHTI technique in this study is used for biceps tendon reconstruction

[5, 6]. Also, it has been shown that this method provides suitable strength in comparison to using an interference screw to fix the injured ACL [7]. Moreover, study on the influence of the geometrical parameters on the fixation strength of BASHTI technique also defines a tendon compression (TC) parameter and investigates the effect of TC on the maximum strength. It was concluded that TC often increases the fixation strength. However, an over-compression can occur in samples with higher TC, which negatively affects the fixation strength [8]. Bone density and also geometry parameters such as graft size, core bone diameter, and the bone tunnel diameter are some important parameters that could affect the final biomechanical parameters of the BASHTI fixations for ACL reconstruction [9, 10]. This study aims to investigate the effect of the ligament size on the final strength of BASHTI fixation technique under an ACL loading condition. Four different ligament sizes are used to prepare specimens, which undergo a three-step loading. The maximum strength and the level in which it occurs are discussed.

Experimental

20 laboratory samples of the reconstructed ACL were prepared using bovine digital tendons and Sawbones artificial bone blocks (Pacific Research Laboratories, Malmo, Sweden). The Sawbones with a density of 320 kg/m3 were selected to represent the tibia bone properties [11]. Tendons were harvested from dissecting bovine's leg and were separated from the muscles around it without any injuries in specimens. To have the same mechanical properties, cows with the same race were chosen. The tendons were harvested shortly after being slaughtered, and they were frozen freshly at -20°C [12, 13]. Tendons are also kept moist during the test so that the properties remain the same.

The specimens were divided into 4 Groups considering the tendon sizes of 6 mm, 7 mm, 8 mm, and 9 mm. The bone tunnel size set to 10 mm, and the core bone diameter was 8.5 mm for all four groups. Tunnels and core bones were produced by special drills. The final grafts were prepared and fixed with the hand-hammer [5, 6] (Figure 2. a & b). Samples were tested under a three-step loading scenario simulating the real condition of an ACL reconstruction, which is 10 cycles of 0.1 Hz periodic loading between 10 N and 50 N as the pre-load [13], 150 cycles of 0.5 Hz periodic loading between 50 N and 200 N immediately followed by a 20 mm/min pull-out loading to evaluate the final strength and stiffness of BASHTI fixation samples of each group (Figure 2. c).

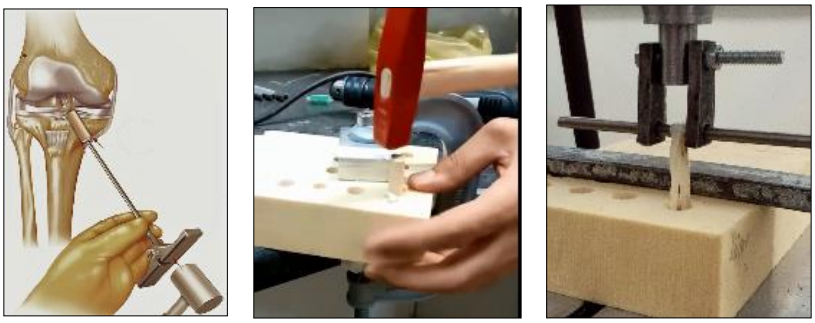

Figure 2. a & b. Hammering the core bone into the bone tunnel, c. Sample on the testing machine

Results and discussion

All the samples from the groups 1 and 2 failed during the second cyclic loading step while all the samples from the groups 3 and 4 reached the pull-out loading step. The average of maximum strength load for the groups 1 to 4 were 77±40 N, 87±44 N, 386±128 N, and 348±146 N (95% CI), respectively, using the sample t distribution. These data were statistically analysed using ANOVA one-way method and it was calculated that the ligament size had a significant effect on the BASHTI fixation ($p < 0.001$). It was observed that the tensile strength of this fixation is higher than 200 N (i.e. the required strength for knee active motions during rehabilitation [14]) for groups 3 and 4. So it could be concluded that this fixation method is acceptable for ACL reconstruction. Also, it

could be seen from the results of the groups 3 and 4 that increasing the ligament size, while the core bone and the tunnel diameters were considered constant, does not necessarily increase the strength of BASHTI fixation. It is believed that when the tunnel and the core bone diameters are considered constant and the ligament size increases too much, the site gets saturated, and the core bone does not penetrate the bone tunnel properly to create a stable fixation.

Table 3. Results of four groups

Group No.	Geometry (mm)			Tensile Strength (N)
	Tunnel	Core Bone	Tendon	
1	10	8.5	6	77±40
2	10	8.5	7	87±44
3	10	8.5	8	386±128
4	10	8.5	9	348±146

Conclusion

BASHTI technique is an acceptable alternative for the conventional ACL reconstruction method. The experiments showed that the ligament size had a significant effect on fixation strength. Also, it was shown that the increase in the ligament size when other geometrical parameters are considered constant, may cause an increase or decrease in the fixation strength according to the value of the geometrical parameters.

Reference List

[1] Saithna, A., Chizari, M., Morris, G., et al., Clinical Biomechanics, 30(6) 551, 2005.
[2] Borjali, A. et al., (2020) bioRxiv, DOI: 10.1101/2020.09.03.281915.
[3] Bashti, K., Tahmasebi, M.N., Kaseb, H., et al., Archives of Bone and Joint Surgery, vol. 3, no. 1, pp. 29–34, 2015.
[4] Borjali, A., Farrahi, G., Jafarzadeh, et al., in: The 27th Annual International Conference of Iranian Society of Mechanical Engineers-ISME2019.
[5] Nourani, A., Mohseni, M., Korani, H., et al., in: The 27th Annual International Conference of Iranian Society of Mechanical Engineers-ISME2019.
[6] Mohseni, M. et al., (2022) Scientia Iranica, DOI: 10.24200/sci.2022.58026.5525
[7] Borjali, A. et al., (2021) BMC Musculoskeletal Disorders 22(1) 1-13
[8] Moeinnia, H., Nourani, A., Borjali, A., et al., Journal of Knee Surgery, 33(5), 2020.
[9] Dehestani, P. et al. (2022) Journal of Experimental Orthopaedics 9(1) 1-12
[10] Mohseni, M. et al., (2021) Archives of Clinical and Experimental Surgery 10(11) 1-7
[11] Snow, M., Cheung, W., Mahmud, J., et al., Knee Surgery Sports Traumatology Arthroscopy, 20(2) 262, 2011.
[12] Beynnon, B.D., Amis, A.A., Knee Surgery, Sports Traumatology, Arthroscopy, 6 Suppl 1, S70-6, 1998.
[13] Chizari, M., Wang, B., Barrett, M., et. al., Biomedical Engineering: Applications, Basis and Communications, 22, 427–436, 2010.
[14] Lim, B., Shin, H., Lee, Y., Knee Surgery Sports Traumatology Arthroscopy, 23, pages1231–1238, 2015

Thermodynamic Analysis of R32 Heat Pump System for Domestic Hot Water Generation

Roopesh Chowdary Sureddi[1], Liang Li[1*], Muhamad Yulianto[2], Niccolo Giannetti[2], Kiyoshi Saito[2]

[1] School of Physics, Engineering and Computer Science, University of Hertfordshire, Hatfield, AL10 9AB, UK.

[2]Department of Applied Mechanics and Aerospace, Faculty of Science and Engineering, Waseda University, Shinjuku-ku, Tokyo 1698-555, Japan.

Keywords: Heat Pump System, R32, Domestic Application,

Carbon reduction technologies remain one of the leading research topics currently. Heat pumps offer an efficient way for energy conservation in both heating and cooling applications. The utilisation of new refrigerants with lower global warming potential (GWP) reduces the release of carbon content. The most commented refrigerant is R132a, with a high GWP of around 1300 for the heat pump system. In recent years, R32 has been researched extensively as an alternative for R132a as R32 has a lower GWP of about 700. In this study, a small-scale test rig of the R32 heat pump for domestic hot water application has been developed and investigated experimentally and theoretically. The test rig consisted of a number of essential components, including an R32 compressor, finned tube heat exchanger, water pump, connections, data logger etc. This study aims to analyse the performance of a heat pump water heating system with R32 under different environmental and load conditions. In this paper, the experimental investigations were mainly carried out on an R32 heat pump system with different ambient temperatures and workloads. Subsequently, the effects of different ambient temperatures of 35^{o}C, 25^{o}C and 16.5^{o}C on the system performance are evaluated, compared and analysed. In addition, the effection of different water mass flow rates of 0.005 kg/s, 0.007 kg/s, 0.015 kg/s, 0.023 kg/s, and 0.035 kg/s on the system performance and investigated as well. The calculated COPs, heat transfer rates and maximum outlet water temperatures of the R32 heat pump system at respective loads and conditions to obtain the results has been analysed. The test results and analysis are essential to understand the system operation at different ambient temperatures and situations which can significantly contribute towards optimal R32 heat pump design and system performance controls.

Corresponding author. Tel.: +44(0) 1707284151.

E-mail address: l.li30@herts.ac.uk (L.Li).

University of Hertfordshire UH

Constrained-type Particle Swarm Optimisation for Asynchronous Irregular Behaviour in a Loosely Balanced Spiking Neural Network

Samuel Sutton[1], Volker Steuber[1] Michael Schmuker[1]

[1]*Biocomputation group, Department of Computer Science, University of Hertfordshire, Hatfield, UK*

Keywords: spiking neural network, balance, sustained activity, particle swarm, optimisation

Cortical neurons that exhibit asynchronous irregular spiking activity are able to encode and propagate multidimensional population codes more efficiently. This activity also enables neural populations to react more rapidly to noisy stimuli. Loose temporal balance of excitatory/inhibitory synaptic input currents into each neuron has been suggested as the cause of irregularity in cortical spike trains [1]. Large simulated networks of integrate-and-fire point neurons with sparse, random connectivity, referred to here as loosely balanced networks, have been used to study such sustained asynchronous irregular (AI) activity [2]. This self-sustained AI activity facilitates rapid response to small changes in input [3]. For such output spike train activity to emerge, appropriate adjustments of specific parameters are required to achieve AI activity in balanced networks with sparse random connectivity. Previously, Vogels and Abbott [3] conducted a grid-based parameter search, systematically varying the strengths of the excitatory and inhibitory synapses of all neurons in the network. They demonstrated it was possible to achieve AI state activity by meeting three conditions: sustained activity, relatively low firing rates, and inter-spike intervals (ISI) CVs near 1. Further, they explored the impact of synaptic conductance on the stability, firing rate and irregularity of a balanced network in order to facilitate the propagation of signals. In the current work, we demonstrate a cost function that aims to find a configuration of input parameters to a loosely balanced network that produces AI behaviour by default. A Constriction-type Particle Swarm Optimisation (CPSO) [4] with global best topology was used to automate our search. Fig.1*a* depicts a schematic of the loosely balanced network utilised in our simulations. Fig.1*b* illustrates our cost functions for each of the recorded spike train statistics calculated. We chose to optimise towards AI behaviour. The particle best fitness versus swarm iteration plot is shown in Fig.1*c*. Fig.1*d* are the particle fitness and spike train statistics recorded and calculated from the simulated network in that position in excitatory and inhibitory conductance parameter space over 250 swarm iterations.

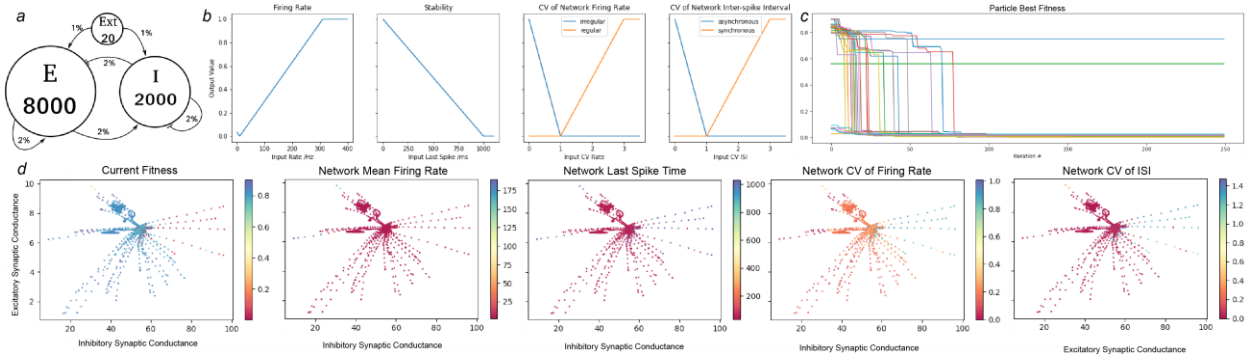

Fig. 1 – a. Schematic of the spiking neural network used. b. Cost Functions used by CPSO. c. Fitness Vs Iteration for all Particles. d. Particle positions visited coloured by particle fitness and resulting network spike train statistic.

Our results demonstrate (Fig.1*c*&*d*) that our search for AI behaviour was successful, with all but two particles crossing the fitness threshold of our cost function. Six of the best scoring particles were initialised in an area that produced a high fitness while the two worst particles became trapped in a local minima. This suggests we need to further alter our swarm parameters. In comparison to a grid parameter search, this method explores the two dimensional parameter space at a finer spatial resolution with the explicit purpose of finding configuration of input parameters that produce AI behaviour. In this two dimensional parameter space this method requires far more simulations to adequately explore the global minima in which this behaviour is observed. CPSO becomes comparatively more effective than the previous grid search method at exploring the parameter space with increasing dimensionality. We aim to use this method to optimise a parameter search to reveal areas of input parameters that produce balanced networks with robust specific behaviours to wider range of network stimulus.

References

[1] Denève, S. *et al.* (2016). Nat. Neurosci. **19**(3), 375
[2] Brunel, N. (2000). Neurocomputing **32–33**(3), 307
[3] Vogels, T. P. *et al.* (2005). J. Neurosci. **25**(46), 10786
[4] Clerc, M. *et al.* (2002). IEEE Trans. Evol. Comput. **6**(1), 58

Design of a hybrid concentrated solar – micro gas turbine CHP system

SeyedVahid Hosseini[1], Hossein Madani[2], Sara Hatami[2], Yasser Sorouraddin[1], Mahmoud Chizari[1]

[1]University of Hertfordshire; [2]Samad Power Ltd

Keywords: Micro gas turbine, Concentrated solar, Hybrid, Power generation

Solar energy can be hybridized with other energy sources to compensate for the fluctuation of solar irradiation in energy generation systems [1]. Among other energy sources and devices, a micro gas turbine has the flexibility to combine with a solar dish to achieve an optimum hybrid solar system [2, 3]. The combination of a solar dish collector with a micro gas turbine has the potential to increase the power density to be used in distributed power generation and microgrids. In order to design this type of hybrid system, the solar dish is usually determined based on the available irradiation of the installation environment; other components, consequently, are sized to achieve the high temperature of the cycle on an established configuration with iterative nested loops method [4]. This conventional method lacks configuration flexibility. Therefore, to consider the possibility of different configurations, a global method is implemented in this paper and applied for a test case in Pretoria, South Africa. In this order, the 0-D governing equations of all the components including both the solar side and gas turbine side are presented in a similar generic form and integrated into the global matrix. The heat and pressure loss between the components is also represented in the same 0-D manner. A multi-dimensional Newton-Raphson method is employed to solve the system of equations to satisfy mass, energy, and heat transfer equations. Two different arrangements of the system and the result of simulation for internal parameters are shown in Fig 1.

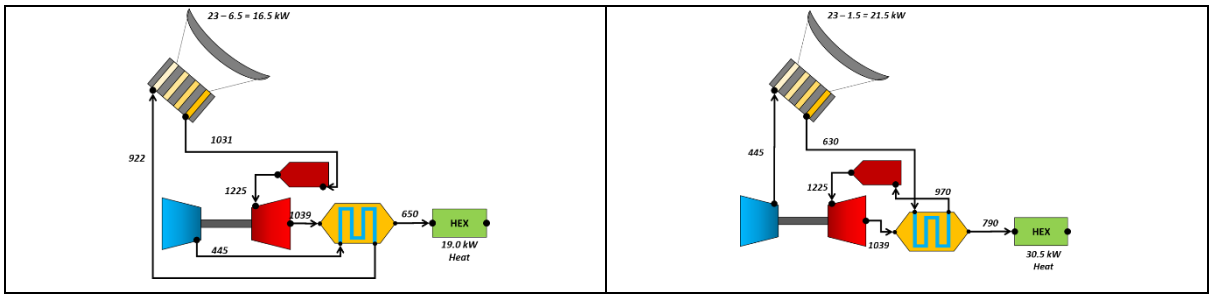

Fig. 1 – Two sample configurations for the hybrid system: a) Hot receiver, b) Cold receiver

With this simulation architecture, the effect of ambient conditions and each component characteristics on the overall system performance can be easily evaluated; The effect of recuperator effectiveness on power and heat output of the system is shown in Fig. 2. The simulations reveal that the higher the working temperature of the thermal energy storage, the higher the electrical efficiency of the fuel and the higher contribution of the solar energy in both configurations.

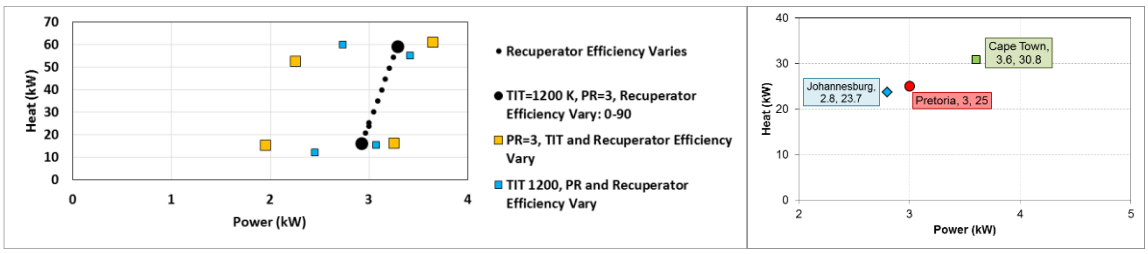

Fig. 2 – a) effect of recuperator effectiveness, TIT and compressor PR, b) effect of ambient conditions

University of Hertfordshire UH

References

[1] Kasaeian A., Bellos E., Shamaeizadeh A., Tzivanidis C. (2020), Solar-driven polygeneration systems: Recent progress and outlook,Applied Energy, Volume 264.
[2] Hosseini S.V., Izadi A., Madani S.H., Chen Y., Chizari M. (2021) Design Procedure of a Hybrid Renewable Power Generation System. Energy and Sustainable Futures. Springer Proceedings in Energy. Springer, Cham.
[3] Hosseini S.V., Izadi A., Boloorchi A.S., Madani S.H., Chen Y., Chizari M. (2021) Optimal Design of Environmental-Friendly Hybrid Power Generation System. Energy and Sustainable Futures. Springer Proceedings in Energy. Springer, Cham.
[4] Ssebabi B., Dinter F., Spuy J, Schatz M. (2019), Predicting the performance of a micro gas turbine under solar-hybrid operation, Energy, Volume 177.

A Multi-object Spectroscopic Survey of HII regions in M31

Chloe Bosomworth[1], Jan Forbrich[1,2]

[1]*Centre for Astrophysics Research, University of Hertfordshire;* [2]*Center for Astrophysics | Harvard & Smithsonian;*

Keywords: astrophysics, galaxies

Giant Molecular Clouds are the main sites of star formation, composed primarily of molecular hydrogen. They contain information on the chemical history of galaxies that is critical to our understanding of galaxy formation and evolution. HII regions are mainly made up of ionised hydrogen, and are typically found in GMCs where star formation has recently taken place. We have conducted a multi-object spectroscopic survey using the MMT telescope to probe cloud-scale metallicities in the Andromeda galaxy (M31), observing almost all of the Herschel-identified Giant Molecular Associations in M31 [1]. The MMT is a 6.5m telescope, making it one of the largest optical telescopes in the Northern Hemisphere. A range of metallicities have been found in the past for similar targets [2]. By probing these beyond simple radial gradients we aim to explore the impact of metallicity on the CO X-factor and on cloud-scale star formation laws, as well as the metallicity structure for HII regions in M31. Using $H\alpha$ and other emission lines, we will both securely identify HII regions and obtain metallicity measurements across M31 from emission line ratios. For these measurements, we plan to estimate oxygen and nitrogen abundance using strong-line diagnostics. I will present first results of this survey.

As shown in Figure 1, our survey covers the entire disk of the galaxy. These results supplement SMA observations of resolved individual GMCs in M31, on scales comparable to Milky Way studies [3,4]. Figure 1 also displays a close-up view of one of our sources, and the corresponding spectrum obtained.

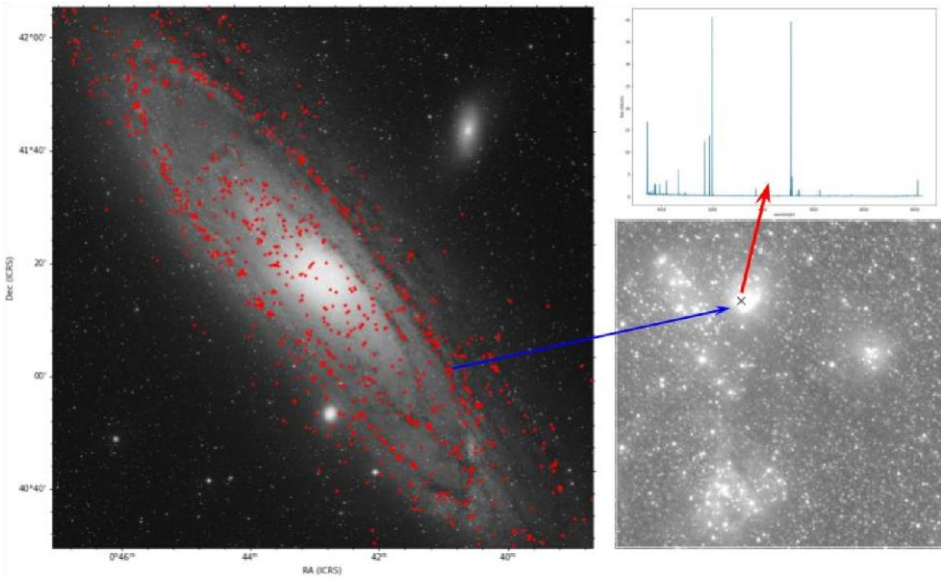

Fig. 1 – ***LEFT:*** *Sources observed with the MMT, shown in red, overlaid on the M31 image from the Digitized Sky Survey (DSS).* ***BOTTOM****: HST PHAT survey image (F475W, wavelength 4750 A) showing the field of view around one of our˚ sources, labelled as 'x'.* ***TOP****: An optical spectrum obtained for 'x'.*

References

[1] Kirk, J.M. *et al.* (2015) ApJ **798**(1) 58

[2] Sanders, N.E. *et al.* (2012) ApJ **758** 133

[3] Forbrich, J. *et al.* (2020) ApJ **890** 196

[4] Viaene, S. *et al.* (2021) ApJ **912** 68

University of Hertfordshire UH

Topological insight into brain dynamics during task execution

Emil Dmitruk[1*], Christoph Metzner[2,3], Volker Steuber[1], Shabnam Kadir[1#]

[1]*University of Hertfordshire*
[2]*Technische Universität Berlin*
[3]*Charité-Universitätsmedizin Berlin, Germany*
*corresponding author: e.dmitruk@herts.ac.uk
[#]corresponding author: s.kadir2@herts.ac.uk

Persistent homology is a branch of algebraic topology that has recently given a lot of insight on how the brain operates. However, there is still a lot to be said about the how the higher cognitive functions operate. In this work we are looking into the topological properties of the sliding window correlations by developing a method to study the changes of topological properties of a dynamical system- brain that is executing a motor task.

Keywords: persistent homology; task-based fMRI; topological data analysis; dynamical systems; functional connectomics;

Introduction

What happens in the human brain while a person rests or performs a task? The literature provides many studies explaining brain activity patterns in the resting state. What is not yet well understood are the processes underlying higher order cognitive functions, which can be observed during task execution. In this work we investigate the evolution of topological properties of the brain activity during task execution to learn more about the underlying functional connectivity patterns. Namely, we analyse how the topological properties - persistence of the cycles [1] change over the fMRI recording acquired during simple motor tasks[2].

Experimental

We use motor task fMRI recordings from Midnight Scan Club (MSC) [2] and derive topological properties from the sliding window correlations. However, before introducing topological computations, we parcellate the brain scans into brain regions defined in the AAL2 atlas[3] (Figure 1.a) and compute an average voxel intensity time series for each of the regions(Figure 1.b). Then, we compute Pearson correlation between all regions for a sliding window. For each position of the sliding window we are getting a correlation matrix(Figure 1.c), that we later use to derive clique filtration [4] which reveals the evolution of topological properties (Figure 1.d). We quantify the evolution of the topological properties by studying changes in birth-death diagrams. In the last step, we compute pairwise Wasserstein distance between all pairs for correlation matrices and thus obtain Wasserstein distance matrix (Figure 2).

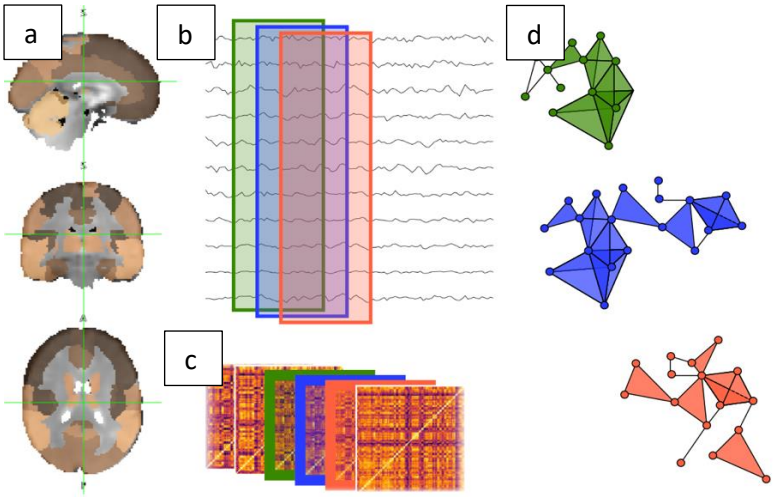

Figure 1. Data processing. Midnight Scan Club task-related fMRI scans are parcelled into brain regions according to AAL2 brain atlas (a); time series are generated as an average brain activity in each of AAL2-defined brain regions and the Pearson correlation is computed for a moving window (b); correlation matrices resulting for a moving window (c); graphical representation of cycles formed in the filtration of ordered correlation matrix (d).

Results and discussion

Interestingly, our initial results indicate that some of the task transitions are correlated in time with the occurrence of higher ordered topological structures. Figure 2.a shows an example of Wasserstein distance matrix for cycles of dimension 4 for one fMRI scan from MSC data set. For many samples the Wasserstein distance is zero and closer inspection of their clique filtration revealed that they do not have topological structures of dimension 4. However, for some samples the distance is non-zero which shows that there are topological structures of dimension 4. Also, the appearance of those topological structures correlates with the onsets and offsets of the stages of executed tasks (shown in Figure 2.b). We hypothesise that high-dimensional topological structures are related to the brain state transitions. What we found surprising is the fact that not all transitions are accompanied by formation of those structures.

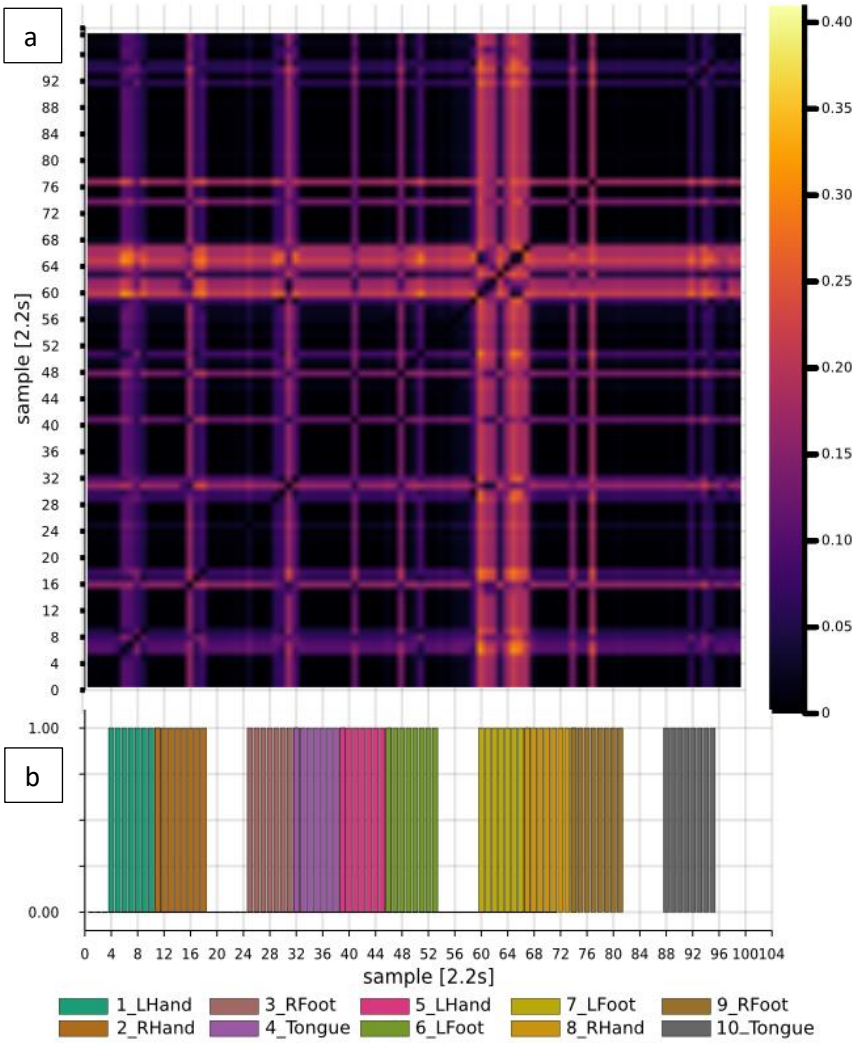

Figure 2. Wasserstein distance matrix (for cycles of dimension 4) representing the pairwise similarity of topological structures in a sequence of correlation matrices (a); information about task execution (b).

Conclusion

We present a novel method for studying dynamic systems and show its application to a task-based fMRI recordings. This is one of very first attempts on using high dimensional topological structures to study the functional dynamics of the brain. An important advantage of our method is the fact that we are working on the recordings of individuals and not on the population data, which is the most common practice in the field. By focusing on individuals, we aim to get more understanding of differences between individuals' brain functional connectomics.

University of Hertfordshire UH

Reference list

[1] A. Zomorodian, 'Fast construction of the Vietoris-Rips complex', *Comput. Graph. Pergamon*, vol. 34, no. 3, pp. 263–271, 2010, doi: 10.1016/j.cag.2010.03.007.

[2] E. M. Gordon *et al.*, 'Precision Functional Mapping of Individual Human Brains', *Neuron*, vol. 95, no. 4, pp. 791-807.e7, Aug. 2017, doi: 10.1016/j.neuron.2017.07.011.

[3] E. T. Rolls, M. Joliot, and N. Tzourio-Mazoyer, 'Implementation of a new parcellation of the orbitofrontal cortex in the automated anatomical labeling atlas', *NeuroImage*, vol. 122, pp. 1–5, Nov. 2015, doi: 10.1016/j.neuroimage.2015.07.075.

[4] C. Giusti, E. Pastalkova, C. Curto, and V. Itskov, 'Clique topology reveals intrinsic geometric structure in neural correlations', *Natl. Acad. Sci.*, pp. 13455–13460, 2015, doi: 10.1073/pnas.1506407112.

Characterisation Experiments for a Multichannel Electronic Nose

Nik Dennler[1,2], Damien Drix[1], Shavika Rastogi[2,1], Michael Schmuker[1]

[1]*Biocomputation Group, University of Hertfordshire, Hatfield, UK*

[2]*International Centre for Neuromorphic Systems, Western Sydney University, Sydney, AU*

Keywords: electronic nose, gas sensing, characterisation experiments, artificial olfaction

The processing of sensory information is essential for an agent to successfully interact with its outside world. While biology-inspired processing strategies have successfully been applied to tasks dealing with with vision [1], auditory perception [2], touch [3] and vibration sensing [4], for the sense of smell there persists a major performance gap between artificial systems and biology [5]. This is particularly evident if one considers the temporal domain: Mammals are able to discriminate temporal correlations of rapidly fluctuating odours at frequencies of up to 40 Hz [6], while metal-oxide (MOx) gas sensor based olfactory systems are usually several orders of magnitude slower [7]. Progress in the field is partly hampered by the poor availability of datasets, from which some have limitations posed by sensor drift [8].

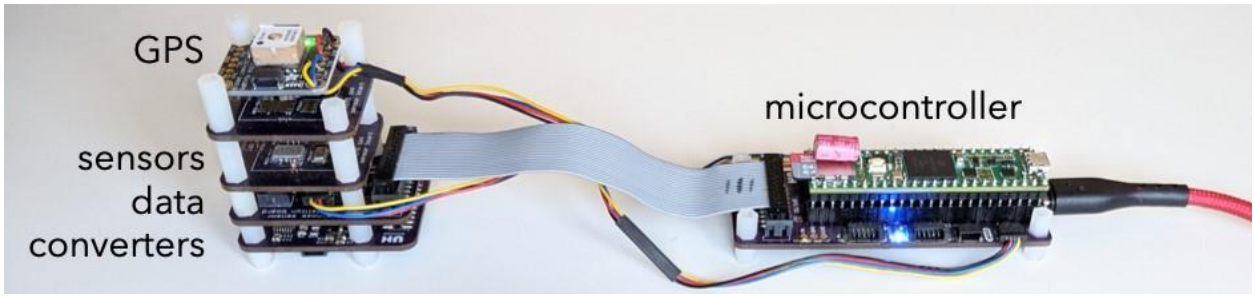

Fig. 1 – High-frequency and heater-modulated MOx multichannel electronic nose.

Our lab has constructed a high-frequency and heater-modulated MOx multichannel electronic nose, which we previously used to record natural olfactory scenes. We demonstrated that short data sequences are enough to train and test a classifier [9] and for generating spike-events [10]. In an upcoming series of experiments, we aim to fully characterise the device in a laboratory setup.

We will test the capabilities and limitations of the electronic nose under different conditions. First, we aim to find the optimal heater modulation that allows for rapid and accurate odour recognition. Second, we want to know to what extent the electronic nose matches the capability of mammals in rapidly distinguishing correlated and anti-correlated odour pairs. Further, we investigate the recognition of an odour within naturalistic plume dynamics, and the distinction of an odour mixture originating from single or multiple sources (based on pre-recorded plume dynamics). Finally, we want to know the limit of detection for single and multiple odours. We use the setup described in [6], which consists of a micro-valve based odour deployment system, that allows for tight control over temporal and spatial parameters.

References

[1] Lichtsteiner, P. *et al.* (2008). IEEE Journal of Solid-State Circuits **43**(2), 566
[2] Schaik, A. van *et al.* (2005). 2005 IEEE International Symposium on Circuits and Systems. IEEE, 4213
[3] Bartolozzi, C. *et al.* (2016). Nature materials **15**(9), 921
[4] Dennler, N. *et al.* (2021a). 2021 IEEE International Conference on Artificial Intelligence Circuits and Systems
[5] Covington, J. A. *et al.* (2021). IEEE Sensors Journal **21**(11), 12969
[6] Ackels, T. *et al.* (May 2021). Nature **593**(7860), 558
[7] Pashami, S. *et al.* (2012). Sensors **12**(12), 16404
[8] Dennler, N. *et al.* (2021b). arXiv preprint arXiv:2108.08793 (submitted, under review)
[9] Drix, D. *et al.* (2022). (submitted, under review)
[10] Dennler, N. *et al.* (2022). Proceedings of the Neuro-Inspired Computational Elements Workshop. NICE '22 (in press)

Open Forum Discussion

University of Hertfordshire UH

Flywheel Energy Storage System, is it the future for internal combustion engine vehicles?

Mahmoud Eltaweel and Mohammad Reza Herfatmanesh

School of School of Physics, Engineering and Computer Science, University of Hertfordshire

Keywords: Energy Recovery System, Flywheel, Mechanical Storage, Internal Combustion Engines

1. Concerns over global warming and carbon emission reduction targets have led to the development of novel energy recovery systems. Considerable amount of energy is lost during urban driving due to continues braking, which can be recovered and stored. Flywheel energy storage system can recover and store the vehicle's kinetic energy during deceleration with high efficiency. A conventional flywheel can run up to 30,000rpm and can deliver up to 40bhp, that can be kept for 20 to 30 minutes. Flywheel energy storage system is very durable, smaller, lighter and much more sustainable than a petrol-electric hybrid system with comparable overall fuel economy figures to that of hybrid vehicles. The system can reduce the fuel consumption by up to 20% while decreasing the carbon dioxide emissions by approximately 400 kg annually for an average lightweight vehicle in the United Kingdom, calculations made based on a WLTP Class-3 cycle.

In order to meet future emission targets for a wide range of vehicle applications, hybrid systems have been identified as a key technology. There are currently only electric hybrid systems available to the general public. Both electric and hydraulic hybrid systems are commercially available in the bus and truck market. It is possible to implement the functionality of a hybrid system using multiple technologies. In this comparison, flywheel hybrid systems stand out due to their high power density and good energy density. Hybrid systems are comprised of two major components: one for storing energy and the other for moving it from the storage to the vehicle [1]. The high-speed flywheel is the energy store in a mechanical flywheel-based hybrid system. Continuous Variable Transmissions (CVTs) have been used in the Flybrid system, which is the most famous commercial flywheel system on the market. Prior to this application, the Flybrid flywheel had a diameter of under 200 mm, weighed about 5 kg, and stored 540 kJ of energy in it. This has a 108 kJ/kg energy density [2].

It was assumed that the one-way energy transfer efficiency of kinetic energy recovery system KERS would be 85% when constructing a lightweight vehicle model with mass 1800kg. Variables include the vehicle's deceleration rate and the KERS system's storage power. It appears that up to 800kJ of energy can be stored in the flywheel during braking. In all cases, the majority of the available energy is stored when the Flybrid KERS power is more than 200kW, regardless of the deceleration rate at which it's used. This is predicated on the assumption that the KERS-connected axle can generate sufficient braking force to prevent the vehicle from rolling [3].

The UK's Department of Transport estimates that the average UK motorist drove 9,200 miles in 2019. When it comes to fuel efficiency, the average car in the United Kingdom gets 38.8 miles per gallon, or 13.7 km per litre [4]. According to the UK's Department of Transport, the average car in the UK emits 120 grammes of CO2 per km, resulting in an annual emissions total of approximately 1,777 kg of CO2 [4]. In this case, it was assumed that the flybrid system studied will be mechanically connected to the vehicle via a Continuous Variable Transmission (CVT) with an 85 percent fixed efficiency [2]. For vehicles manufactured after 2017, the WLTP cycle is used to measure official fuel consumption and CO2 emissions, which includes a typical journey at low, medium, and high speeds. In this study, WLTP Class-3 was used to measure the potential fuel savings in an average light-weight vehicle in the United Kingdom [5]. According to a WLTP Class-3 cycle, using the flywheel energy storage system in a lightweight vehicle (1,800 kg) can reduce fuel consumption by 237 litres and CO2 emissions by 390 kg per year.

Reference:

[1] I. Foley, "Williams Hybrid Power—Flywheel energy storage," *Engine Expo*, 2013.
[2] J. Hilton, "Flybrid systems—Mechanical hybrid systems," *Proc. Engine Expo*, 2008.
[3] D. Bender, "Flywheels," in *Energy Storage*, World Scientific, 2017, pp. 249–289.
[4] UK Department for Transport, "Transport statistics Great Britain," 2018.
[5] "International: Light-duty: Worldwide Harmonized Light Vehicles Test Procedure (WLTP) | Transport Policy."

Stress and deformation analysis of shaft-mounted permanent magnet rotor of high-speed CHP micro-turbine

Adrian Felix[1], Mahmoud Chizari[1]

[1]School of Physics, Engineering and Computer Science, University of Hertfordshire

Keywords: Permanent magnet rotor, Centrifugal load, Interference fit

Background and Purpose: The Permanent Magnet (PM) rotor of the motor/generator in the micro-turbine analysed in this project is made up of three components:

- Yoke: a cylindrical component with tapered inner surface, perfectly cylindrical outer surface and stepped profile at either end mounted on the turbine shaft
- Segmented magnet: There are eight identical permanent magnet segments fixed to the outer surface of the yoke by adhesive bonding
- Retaining sleeve: a cylindrical sleeve that sits on the outer surfaces of the permanent magnet and stepped surface of the yoke.

Rotation of the rotor causes outward radial displacement due to centrifugal force on the assembly components. The magnitude of centrifugal force a body is directly proportional to its radial distance from the axis of rotation and the density of its material [1]. Temperature creates thermal stresses in the assembly that cause the components to expand outwards as all materials used in it have positive coefficient of thermal expansion and the radial displacement is directly proportional to coefficient of thermal expansion and radius of the component. Therefore, at operating state rotation and high temperature tend to separate the contact layers between the various components of the rotor assembly as the radial deformation of outer layers will be greater than that of inner layers assuming uniform mass density and coefficient of thermal expansion across all layers [2]. In order to compensate for this, the assembly has to be held together by interference fit and/or the mass density and coefficient of thermal expansion of outer layers should be kept to a minimum [3]. The aim of this project is to analyse the shaft assembly with CFRP sleeve and Inconel sleeve separately for strength and contact separation to determine which one offers least contact separation and highest strength.

Methods: This paper uses finite element methods to determine the radial displacement and radial stress at the interfaces between the components to check for contact separation, and the equivalent stresses throughout the assembly to determine strength which is expressed in terms factor of safety and von-Mises criterion of failure.
Results and discussion: The results of the analyses as shown in Fig 1 (a) and Fig 1 (b) were studied and the following conclusions were drawn.

- There is zero contact separation in the case of either CFRP or Inconel 718 sleeve: Fig 1(a)
- PM rotor with CFRP sleeve showed 22.3 % higher factor of safety than that with Inconel 718 sleeve and is hence the more optimum choice: Fig 1 (b)

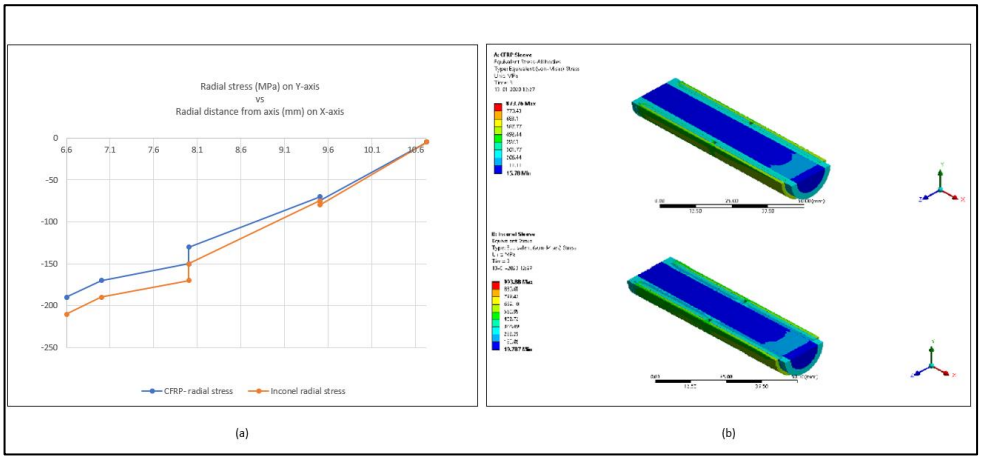

Fig 1: Results of FEA analysis

References

[1] W. Cheng, Z. Deng, L. Xiao, B. Zhong, and B. Zhang, “Strength analytical solution to ultra-high-speed permanent magnet rotor considering temperature gradient and segmental permanent magnet effect,” Adv. Mech. Eng., vol. 11, no. 4, Apr. 2019.
[2] T. Zhang, X. Ye, H. Zhang, and H. Jia, “Strength Design on Permanent Magnet Rotor in High Speed Motor Using Finite Element Method,” TELKOMNIKA Indones. J. Electr. Eng., vol. 12, no. 3, Mar. 2014.
[3] N. A. Noda, D. Suryadi, S. Kumasaki, Y. Sano, and Y. Takase, “Failure analysis for coming out of shaft from shrink-fitted ceramic sleeve,” Eng. Fail. Anal., vol. 57, pp. 219–235, Nov. 2015.

University of Hertfordshire UH

Comparing PCG metrics with Human Evaluation in Minecraft Settlement Generation

Jean-Baptiste Hervé[1], Dr. Christoph Salge[2]

[1]University of Hertfordshire; [2]University of Hertfordshire

Keywords: Competition, Experience Survey, Minecraft, Procedural Content Generation, Computational Creativity, Artificial Intelligence

There are a range of metrics that can be applied to the artifacts produced by procedural content generation, and several of them come with qualitative claims. In this paper [1], we adapt a range of existing PCG metrics to generated Minecraft settlements, develop a few new metrics inspired by PCG literature, and compare the resulting measurements to existing human evaluations.

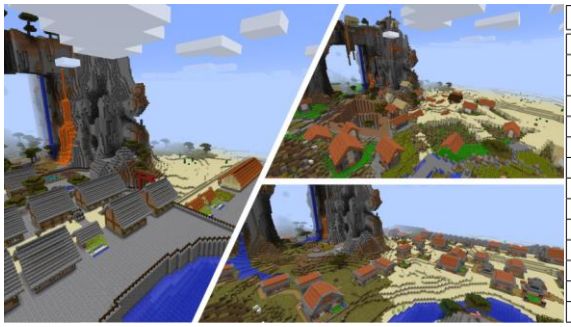

Metrics	Jury Score	Adaptability	Functionality	Narrative	Aesthetic
Level Entropy	-0.26	-0.26	-0.37	0.02	-0.16
Settlement Entropy	0.22	-0.14	0.32	0.2	0.32
Light	0.77	0.49	0.63	0.72	0.73
Defense	0.42	0.07	0.55	0.28	0.47
Functional metric	**0.84**	0.75	**0.85**	0.43	0.65
Aesthetic metric	0.31	0.10	0.39	0.12	0.32
Food	**0.82**	0.54	**0.81**	0.58	0.71
Relation to Environment	0.73	0.42	0.65	0.61	0.61
Block Type Count	0.67	0.28	0.55	**0.81**	0.70
Density	-0.24	-0.33	-0.33	-0.04	-0.18
Platform Size	-0.33	-0.18	-0.41	-0.27	-0.29
Linearity X	-0.19	-0.14	-0.03	-0.37	-0.24
Linearity Z	0.15	-0.27	0.41	0.24	0.30
Filling Ratio	-0.14	-0.03	0.03	-0.13	-0.14

Fig. 1 – On the left, a sample of generated Minecraft Settlements. On the right, Spearman's Rank Correlations between metrics and GDMC scoring. Bold correlation have a p-value below 0.01. Due

to fixed sample size p-values directly depend on correlation value.

We test our metrics on a sample of entries from the Generative Design in Minecraft Competition (GDMC)[2], which are settlements generators submitted by the participants and rated by a human jury.

The aim is to analyse how those metrics capture human evaluation scores in different categories, how the metrics generalize to another game domain, and how metrics deal with more complex artifacts. We provide an exploratory look at a variety of metrics and provide an information gain[3] and several correlation analyses. We found some relationships between human scores and metrics counting specific elements, measuring the diversity of blocks, and measuring the presence of crafting materials for the present complex blocks. Metrics focusing on the layout of the level and aiming at capturing it structures are overall less performing.

These results encourage us to keep investigating the topic of automated metrics, and to pursue our search for embodied metrics, targeting in particular procedurally generated virtual space.

References

[1] Jean-Baptiste Hervé, Christoph Salge (2021). Comparing PCG metrics with Human Evaluation in Minecraft.

[2] Christoph Salge, Michael Cerny Green, Rodgrigo Canaan, and Julian Togelius (2018). Generative design in Minecraft (GDMC) settlement generation competition.

[3] Matthew Stephenson, Damien Anderson, Ahmed Khalifa, John Levine, Jochen Renz, Julian Togelius, and Christoph Salge (2020). A continuous information gain measure to find the most discriminatory problems for ai benchmarking.

University of Hertfordshire UH

Study of the Effect of Stacking Sequence on the Bending Resistance of Composites using Finite Element Analysis

Fiona Mercy Jepleting[1], Opukuro David-West[2]

[1]School of Aerospace and Vehicle Engineering, Technical University of Kenya, Nairobi, Kenya.
[2]School of Physics, Engineering & Computer Science, University of Hertfordshire, Hatfield, United Kingdom

Fiona Mercy Jepleting: fionamj@tukenya.ac.ke

Abstract

In this study carbon fibre reinforced composites of various stacking configuration were modelled using the orthotropic material model and simulated for three-point bending using ANSYS finite element software. The composites were modelled using the shell element. The results showed that the stacking sequence influence on the laminate bending resistance and stress distribution within the plies.

Keywords: composite laminate; finite element analysis; three-point bending; ply stress.

1. Introduction

Advanced composite materials have become an alternative to metals in certain applications due to their desirable characteristics such as higher stiffness, higher strength, low density, better fatigue, and corrosion resistance [1]. These attributes make them acceptable in the aerospace, automotive and medical industries. Static analysis involves three-point flexure tests in bending of composites. Nunes et al [2] used three-point bending flexural test to predict the stiffness of anisotropic composite plates in bending and found out that the flexural behaviour of the composite plate depended on factors such as fibre orientation, laminate stacking and the temperature. In another report, Cantwell et al [3] mentioned that the change in the thickness of composite laminates affect the mode of fracture and Moura and Goncalves [4] conducted three-point beam impact tests on carbon fibre composites structures and concluded that the values were elastic deflection to failure exceeding the peak force and the initiation of fibre failure at the back face.

In some other investigations, Caminero et al [5] discussed about the damages in CFRP composites due to flexure and impact and concluded that stacking sequence has significant effect on the bending response. Dylewski and Login [6] used the solid and shell elements available in HyperWorks finite element code to model 3-point bending in composite beams and compared the results with experiment and analytical results; while Azzam and Li [7] subjected $[0/90/-45/45]_{2s}$ and $[45/45/90/0]_{2s}$ composite laminates to three-point bending and observed that the former to be brittle in behaviour while the latter revealing non-linear characteristics. It has been established by researchers that the ply orientation of composite laminates is dependent on the application and the desired mechanical properties. Also, composites are susceptible to transverse damage such as matrix cracking and delamination as a result of loading in the out of plane direction. In this study three-point bending simulation of composite laminates modelled as a shell were conducted and the results due the effect of the ply directions compared.

2. Description of Finite Element model

Composite laminates made of 16 plies laid up at different orientation with each ply having a thickness of 0.25 mm, were modelled with orthotropic material properties and shell element 181 in ANSYS finite element code. The laminate configurations were $[0/90/45/-45]_{2s}$, $[0]_{16}$, $[90/45/-45/0]_{2s}$, $[0/90/0/90]_{2s}$, $[-30/60/-60/30]_{2s}$ with the dimensions of 197 mm as length and 25.26 mm as the width. Material strength limits as well as damage initiation criteria to define the type of criterion for determining material damage onset and damage evolution law which defined how the material degraded following damage initiation were modelled into the composite. The models were simply supported by constraining the translational degrees of freedoms at locations of 36 mm from the edges of the width and a total load of 470 N applied along to the nodes of the centre in the z-direction. The solution was controlled in steps of the loading to obtain the deformation as the loading progressed.

3. Discussion of Results

The displacement results of the composites laminates in the steps of load increase are shown in Fig. 1(a) and representative result of the contour distribution in Fig. 1(b). The unidirectional composite laminate $[0]_{16}$ had the smallest displacement followed by the cross-ply laminate $[0/90/0/90]_{2s}$, then quasi-isotropic laminate $[0/90/45/-45]_{2s}$, but the displacements of the composites $[-30/60/-60/30]_{2s}$ and $[90/45/-45/0]_{2s}$ being identical.

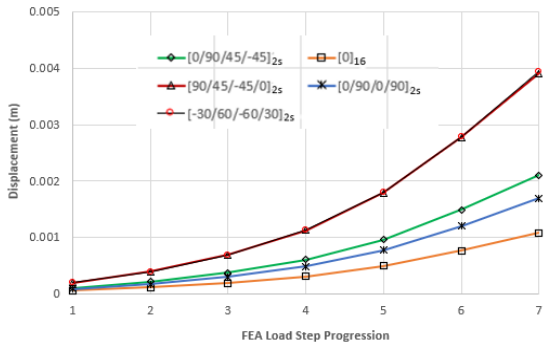

Fig. 1(a): Comparison of the laminate displacement

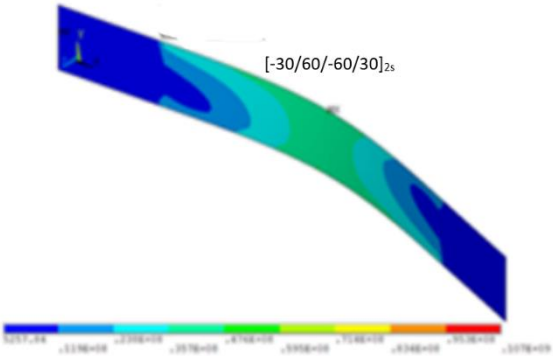

Fig. 1(b): Representative image of the laminate displacement

It could be seen that laminates with 0° ply orientation on the surface had a smaller displacement compared to the others indicating a higher stiffness, this is collaborated by the study from Ribero et al [8]. This shows that the ply orientation affects the flexural strength of the composite laminate.

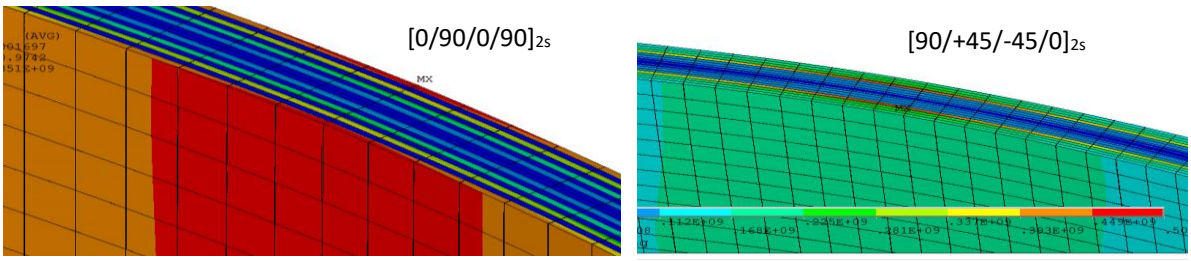

Fig. 2: Stress distribution due to ply orientation.

The stress distribution on each layer of the composite laminate was different due to the difference in ply orientation and the orthotropic nature of the composites. Laminates with 0^0 ply on either surface, experienced a higher stress on the outer most layer due to the high stiffness of the 0^0 ply compared to laminates with 90^0 ply on the outer most layers. On the hand, laminates with 90^0 ply on the top and bottom surface experienced a higher stress on the fourth ply on either side which corresponded to the 0^0 ply as shown in Fig. 2.

4. Conclusion

Three-point bending finite element simulation was used to predict the influence of fibre orientation and laminate stacking sequence on the flexural stiffness of composites. From the analysis it was seen that the unidirectional laminate had the smallest displacement followed by the cross-ply laminate then the quasi-isotropic laminates. Small displacement indicated that the unidirectional laminate was the stiffest, because of the direction of the reinforcement and loading being perpendicular.

5. References

[1] Abrate, S. (1991) Appl Mech Rev, no. 44, pp. 55-187.

[2] Nunes, J. P et al (2002) Polymer testing, vol. 21, pp. 27-33.

[3] Cantwell, W. J. & Morton, J. (1991) Composites, no. 22, pp. 347-372, 1991.

[4] Moura M. F & and Goncalves, J. M.(2002) Composite Part A, vol. 33, p. 361.

[5] Caminero, M. A. et al Composite Structures 136 (2016) 345–357

[6] Dylewski A & Łogin, W. AIP Conference Proceedings 2078, 020085 (2019); https://doi.org/10.1063/1.5092088

[7] A. Azzam A. & Li, W. IOP Conf. Series: Materials Science and Engineering 62 (2014) 012016.

[8] Ribeiro, M. L et al, (2013) IV International Symposium on Solid Mechanics - MecSol Brazil

University of Hertfordshire UH

The spatially resolved radio continuum – star formation rate relation in a sample of nearby spiral galaxies

James C. McGarry[1]

[1]Centre for Astrophysics Research

Keywords: Radio Continuum, Non-Thermal, Star Formation Rate

Star formation can be revealed by radio observations through two types of emission: thermal - which is emitted by electrons in the plasma surrounding young massive stars (HII regions), and non-thermal – which is emitted by high energy electrons as they encounter magnetic fields, accelerated in the shockwaves created by supernovae of these same stars when they reach the end of their short lives. This project aims to see to what extent the non-thermal radio continuum emission can be calibrated as an extinction-free star formation rate (SFR) indicator. This will be performed by mapping four nearby spiral galaxies at multiple radio wavelengths (6 cm, 13 cm, 20 cm) using combined single-dish (Green Bank Telescope) and interferometric (Very Large Array) radio observations. The thermal and non-thermal emission can be separated using a Bayesian separation process outlined in Westcott et al. (2018) [1]. High resolution means the resulting non-thermal maps can be used to investigate the SFR on a spatially resolved basis, e.g., looking at SFR density, or the effect of the local morphology (core, arm, inter-arm spacing). As radio frequency astronomical surveys move to higher sensitivities and resolutions, they will begin to uncover fainter populations of galaxies. For 'normal' star forming galaxies, a calibrated radio continuum – star formation rate (RC-SFR) relation, or Condon relation [2], would allow these surveys to directly uncover SFRs of these galaxies through an extinction-free method.

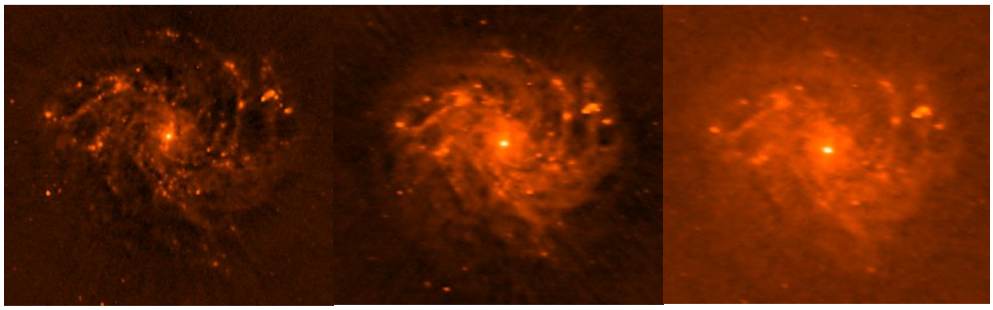

Fig. 1 – Interferometric radio continuum images of the 'fireworks galaxy' NGC6946 at (Left) 6 cm, (Centre) 13 cm, and (Right) 20 cm wavelengths.

References

[1] Westcott, J., et al. (2018) MNRAS **475** 5116

[2] Condon, J. J., (1992) ARA&A **30** 575

Computer Simulation of a Poly Nanofiber Patch Under a Mechanical Loading

Mohammad Najeeb Moraby[1]*, Elif Sensoy[2] and Mahmoud Chizari[3]

[1] Department of Engineering, SPECS, University of Hertfordshire, Hatfield AL10 9AB, UK
** najeeb.moraby@gmail.com*

Abstract: The strength of nanofiber patches need to be evaluated and validated using a reliable testing machine. This study introduces the design of a testing machine which has been prototyped, to evaluate the mechanical strength of nanofiber patches in biaxial plane mode. In parallel a finite element model was created to simulate the experiment and the model was validated by the experimental data obtained from the machine.

Keywords: Poly Nanofiber Patch, Mechanical Testing Machine, Bi-Axial Tensile Test, Numerical Simulation

Introduction

This paper will investigate the performance of nanofibers under bi-axial tensile loading. With the increasing demand for nanofibers, it is crucial for accurate testing methods and machinery to be developed. This paper will test nanofiber specimen using a numerical and experimental method. This facilitates for the comparison of both sets of data and the validation of the prototype built. Nanofibers require extreme precision when being tested, therefore it is important for these machines to be developed and further improved. This project tests the performance of a prototype developed at the University of Hertfordshire by Elif Sensoy [1]. The data obtained from the experimental procedure is to be compared with data yielded from the numerical experiment, this gives insight into the behaviour of nanofiber and their behaviour under biaxial tensile loading and how failure occurs. This data will also allow for a deeper understanding of the mechanical properties of nanofibers. This project will compare two sets of data to obtain an understanding of the behaviour of nanofibers with different ply numbers and dimensions under biaxial tensile loading and will also allow for the validation of the prototype used throughout the project.

Methods

The material selected for testing was Polyvinylidene fluoride (PVDF) nanofiber, but due to procurement problems an alternative material was selected, tissue paper from Andrex. Two testing methods were performed to test the specimens, numerical and experimental testing. In both methods the specimens were tested biaxially and the dimensions of the specimens tested were 90x90mm 1 ply, 90x90mm 2 plies, 100x100mm 1 ply and 100x100 mm 2 plies, respectively.

Numerical method: For the numerical method the first step was to obtain the mechanical properties of the material, due to the company Andrex, Kimberly Clark not willing to provide the mechanical properties, they were acquired from research papers online where; Tensile strength 74N/m, Density 0.9 g/cm^3, Thickness 0.19 mm [2], Tensile Index 1.6 Nm/g, Youngs Modulus 2.8 MPa [3], and Poisson ratio 0.169 [4]. For 1 ply specimens the thickness was assumed to be 0.095mm. After obtaining the properties, the four-square shaped specimens were then modelled on CAD software Solidworks and saved as SLDPRT files to be able to use them as geometry. Following this on ANSYS, explicit analysis is selected as the analysis, as it is suitable for capturing the physics of short-duration experiences for models undergoing highly non-linear transient dynamic forces. A new custom material is then created using the mechanical properties from the research papers and the geometry created on Solidworks is then imported to ANSYS. The material is assigned to the model geometry and then meshed with an element size of 1 mm. An end time of 0.005 s is set in the analysis settings for the duration of the analysis. The boundary conditions are then set according to how the prototype works, where the models will be experiencing biaxial forces of 10 N in four different directions as shown in Figure 1. Finally, solution outputs total deformation, equivalent stress and maximum principal elastic strain are selected, and the simulation is solved.

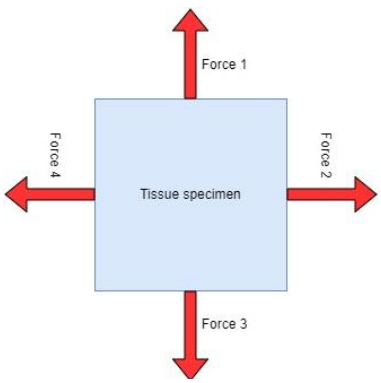

Figure 14 Force set up

The post processor tool is then used to evaluate and interpret the results, where contours, graphs and animations can be generated.

Experimental method: For the experimental testing procedure, specimens of the dimensions listed above were prepared, 10 of each dimension, 40 specimens in total. During preparation, the samples should be carefully prepared to ensure than the samples do not sustain damage which would affect the test results. After preparing the specimens, the prototype is powered up and set up ready for testing, the specimens are then carefully secured within the grippers of the prototype as shown in Figure 2 and tested. The step-by-step procedure for testing of the specimens are as indicated by Sensoy et al. [1].

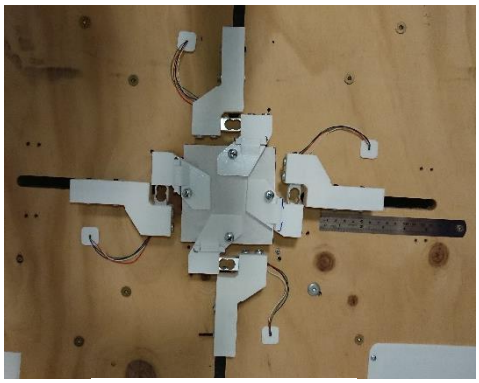

Figure 15 Prototype layout

Results and discussion

Figure 3 shows the behaviour of 100x100mm 1 ply specimen under bi-axial loading where, (a) total deformation, (b) equivalent stress, (c) elastic strain, and (d) the tested specimen can be seen. It can be observed that the experimentally tested specimen in picture (d) fractures in a similar pattern to the numerically tested specimens. From (a), (b), (c), and (d) it can be seen that the specimen experiences more stress, strain and deformation near the corners, and near the centre.

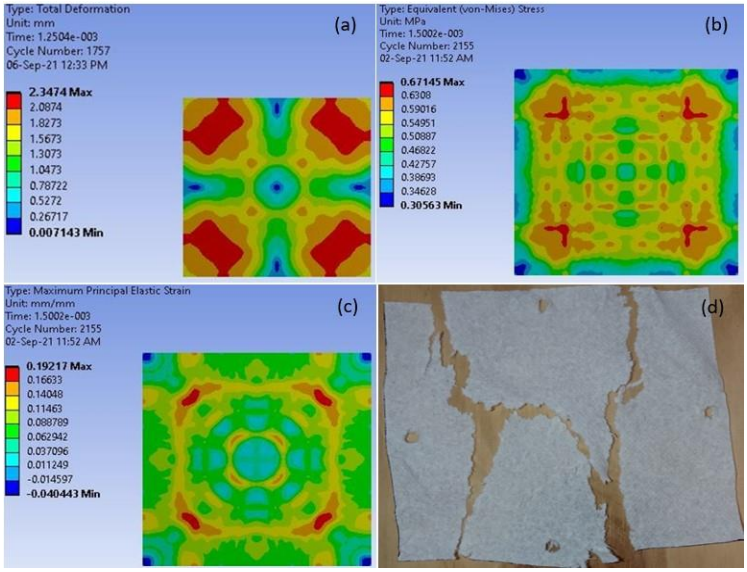

Figure 16 Behaviour of 100x100mm 1 ply specimen

90x90mm 1 ply results			90X90mm 2 plies results		
Specimen	Force/N	Displacement/mm	Specimen	Force/N	Displacement/mm
1	14.299	2	1	36.471	2
2	14.801	2	2	33.218	2
3	16	2	3	36.642	3
4	15.226	2	4	32.489	3
5	14.194	1	5	37.091	2
6	16.024	2	6	36.832	3
7	17.31	2	7	35.562	3
8	18.728	2	8	36.954	2
9	18.097	2	9	38.869	2
10	15.107	3	10	35.39	3
Average	15.979	2	Average	35.952	2.5
100x100mm 1 ply results			100x100mm 2 plies results		
Specimen	Force/N	Displacement/mm	Specimen	Force/N	Displacement/mm
1	16.027	2	1	40.536	2
2	19.551	2	2	39.985	2
3	18.599	2	3	40.77	2
4	20.048	1	4	40.761	2
5	19.437	2	5	42.36	2
6	17.19	2	6	39.355	2
7	16.149	2	7	39.807	2
8	15.764	2	8	38.176	2
9	16.849	2	9	39.132	2
10	15.733	2	10	36.236	3
Average	17.535	1.9	Average	39.712	2.1

Table 1 Experimental results

Table 1 shows the experimental results obtained for the 40 specimens tested on the prototype, where the results are quite consistent. The results for the 2 plies specimens are more consistent compared to the 1 ply specimens since the 1 ply specimens were obtained by separating 2 ply sheets, during this process some of the 1 ply specimens might have sustained some damage such as micro tears in the specimens, causing larger fluctuations in the results. The fluctuations could also be due to the embossing in the material.

	Experimental(Average)		Numerical		
Specimens	Force	T.Displacement	E.Stress	T.Deformation	E.Strain
90x90 1ply	15.979 N	2 mm	2.3028 MPa	18.51 mm	0.74034 mm/mm
90x90 2plies	35.952 N	2.5 mm	2.3147 MPa	11.982 mm	0.89635 mm/mm
100x100 1ply	17.535 N	1.9 mm	1.9979 MPa	16.293 mm	0.63716 mm/mm
100x100 2plies	39.712 N	2.1 mm	0.7041 MPa	10.215 mm	0.19336 mm/mm

Table 2 Experimental and Numerical results

Table 2 shows the test results from the experimental and numerical testing, where the experimental results are an average for each specimen. The experimental results show that 2 plies specimens experienced a greater average force to fracture than the 1 ply specimens, which is due to the thickness of the specimens. It can also be seen that the 100x100 1 ply specimens experience more force to fracture compared to the 90x90mm 1 ply specimens, this is similar for the 2 plies specimens, it is due to the size of the specimens. The 2 plies specimens also fracture at a greater displacement compared to the 1 ply specimens; this is due to higher strength. From the numerical results, it can be observed that the 1 ply specimens, 90x90mm and 100x100mm, experience more deformation compared to the 2 plies specimens, this demonstrates that the 2 plies specimens have higher mechanical strength than the 1 ply specimens, as they are being tested with the same load, the 1 ply will have a greater deformation. Thus, the 1 ply will fracture under smaller forces, this is due mainly to the thickness and size for the specimens. The variations in stress can also be observed where 90x90mm 2 plies experience more stress and strain than the 1 ply. The 100x100mm specimens experience less stress, deformation, and strain than 90x90mm specimens. A difference is also seen between the 100x100mm 1 ply and 2 plies, this is due to the size of the specimen, larger specimens under the same force will experience less stress, deformation, and strain. When comparing the 2 sets of results, it can be observed that a difference in thickness or size of the specimens will affect the test results. Thinner or smaller specimen fracture under smaller forces. Throughout the experimental testing, the prototype provided consistent results except for the 1 ply specimens which have some larger discrepancies, this is due to micro tears or the embossing in the specimen's microstructure. However, due to procurement problems for the selected nanomaterial and data limitations causing the unavailability of the exact mechanical properties of the test specimens, mechanical properties from research literature were used for testing, rendering data to data comparison not possible. However, the results obtained from simulations gave an insight into what to expect in the experimental results.

Conclusion

To conclude, both experiment methods demonstrated that the thickness and size of the specimens has a major impact on the behaviour of the material under stress and how defects in the specimens affect results. The data from the two experiments showed some similarity but were not able to be fully compared. The prototype was able to provide accurate and repeatable results, validating the reliability of the results obtained through the experimental test procedure, this could be observed from the consistency of the test results generated.

References

[1] Sensoy, E. & Chizari, M., 2021. Mechanical Strength of Poly Nanofiber Patch Under a Biaxial Tensile Loading. Energy and Sustainable Futures, pp. 269-274.

[2] Park, Y. N., Ko, C. Y., Melani, L. & Kim, J. H., 2020. Mechanical properties of low-density paper. Nordic Pulp & Paper, Volume 35.

[3] Vieira, C. J. et al., 2020. Impact of 5-Ply toilet paper configuration on its mechanical and absorption properties. BioRes, 15(4), pp. 7475-7486.

[4] Hua, G., Maoteng, Y., Fei, W. & Lu, F., 2020. Poisson's ratios of molded pulp materials by digital image correlation method and uniaxial tensile test. Journal of Engineered Fibers and Fabrics, Volume 15, p. 1–10.

University of Hertfordshire UH

Design a bionic tendon clip for triple graft suspensory fixation

Seyed Amir Hossein Sajedi[1], Amir Nourani[1], Mahmoud Chizari[2]

Department of Mechanical Engineering, Sharif University of Technology, IR
School of Engineering and Computer Sciences, University of Hertfordshire, UK

Abstract: ACL rupture affects lives of many athletes every year. The injury results a severe knee pain and limit the patient's mobility. There are various surgical methods to treat such injuries, among them, Suspensory Fixation is considered as a non-invasive effective method. This study presents a design for an in vivo bionic tendon clip to assist the surgeon to fix the third limb of tendon graft tightly to other limbs while preventing any inner fibers slippage and increasing graft strength.

Keywords: Knee; Anterior cruciate ligament; Bionic clip, suspensory fixation; double and triple tendon grafts

Introduction: Double-bundle ACL reconstruction tries to recreate the anatomy of native ACL, by reconstructing two bundles. Some recent studies have shown there is significant anteroposterior and rotational stability with this technique. Double-bundle ACL reconstruction requires grafts with an approximate diameter of 7 mm, using autografts is preferred as it is much easier to access and in the case of athletes under 30, is the gold standard. The downside of autografts is the limited quantity of tissue available. One potential way to provide grafts with the required diameter and mechanical strength is to triple the graft. Some controlled studies including [1] have shown that there is no significant difference between doubled tendons and tripled whip-stitched ones, although it was observed that there was a notable displacement of third tendon limb, so it was then concluded that whipstitching third limb not only didn't have a noticeable effect on graft stiffness but also increased the chance of failure. This study aims to develop a method of tightening the end of the third limb without whipstitches to increase stiffness and eliminate possible elongation. Such a clip must be capable of withstanding regular forces applied to the ACL tendon during daily activities. Attempts made to design such bionic tendon clips resulted in the development of six prototypes. Four of them are shown in (Fig. 1). These prototypes will be developed and tested in the future.

Methodology: Eleven prototypes will be developed which six of them were chosen to be developed due to concerns regarding size and simplicity of use. Designs of these six prototypes will be developed and completed and some of them will be manufactured. The use of a bionic sync sheath between clip and tendons has been proven to increase tendon stiffness [2] thus some designs will be sync sheath compatible. The tests will be done on pieces of silk rope in the preliminary stages and the later tests will be done on bovine flexor tendon grafts.

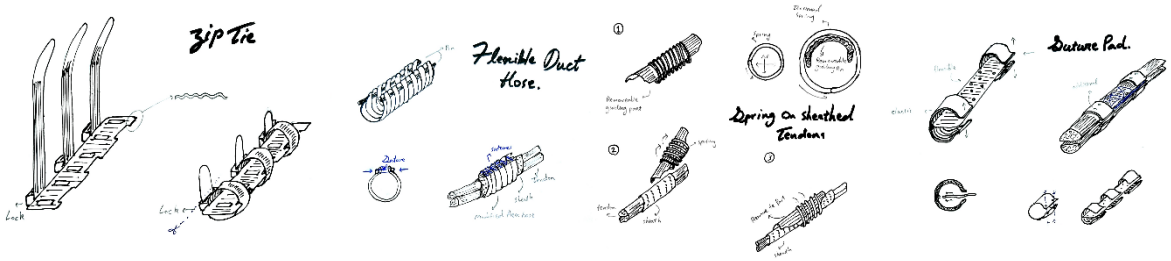

Fig. 1 – Schematics of 4 tendon clip designs including, Zip Tie, Flex Hose, Spring Sheath and Suture Pad

Results: Prototypes of the clips are due to be manufactured, and the samples will be tested on dummy and bovine flexor tendon grafts. Following testing process, the design will be optimized.

Conclusion: The outcome of this research may help to improve the double-bundle suspensory ACL fixation surgical method and shorten the process of rehabilitation. The outcome can also be used in the development of tendon clips suitable for other tendon injuries.

References:

[1] Martyn Snow, William Cheung, Jamaluddin Mahmud, Sam Evans, Catherine Holt, Bin Wang, Mahmoud Chizari, Mechanical assessment of 2 different methods of tripling hamstring tendons when using Suspensory fixation, Knee Surg Sports Traumatol Arthrosc. 2011, doi: 10.1007/s00167-011-1619-5

[2] Adnan Saithna, Mahmoud Chizari, Guy Morris, Cameron Anley, Bin Wang, Martyn Snow, An Analysis of the Biomechanics of Interference Screw Fixation and Sheathed Devices for Biceps Tenodesis, Clinical Biomechanics, Vol 30, Issue 6, 2015, pp 551-557, doi: 10.1016/j.clinbiomech.2015.04.006

Moving from fossil energy to renewable energy; a business perspective

Yasser Sorouraddin*, Vahid Hosseini, Mahmoud Chizari

Department of Engineering, SPECS, University of Hertfordshire, Hatfield AL10 9AB, UK
** ys21aat@herts.ac.uk*

Abstract: The urgent need to address climate change and its adverse effects is felt worldwide. Burning fossil resources is primarily human responsibility and potential for emission of greenhouse gases. In other words, climate change is not only affecting the environment but also hurting the economy. The UK government has been decided to launch legislation to achieve net zero emissions by 2050. This places the UK as the first major economy to make such a commitment and follows the recommendations of the Committee on Climate Change's recently published 'Net Zero' report, which showed that eliminating emissions by 2050 is technologically feasible. However, the consumers' negative attitudes to renewable energy are significant barriers to developing the hydrogen economy as green energy in the UK. The public view has concentrated on the impacts of renewable energy on their everyday lives. Meanwhile, the future of the UK's green economy still appears uncertain, caused by additional risks to the future of renewable energy developments. For instance, for the technology to become part of the UK green energy market, the cost of production must come down. This study aims to evaluate the prospective migration of the current hydrocarbon fossil fuel paradigm to renewable energy feedstock and infrastructure.

Keywords: Natural Gas System, Decarbonization, Hydrogen Production and Cost, UK's Hydrogen Roadmap, PESTEL analysis

Introduction

The urgent need to address climate change and its adverse effects is felt worldwide. Burning fossil resources is primarily human responsibility and potential for emission of greenhouse gases. In other words, climate change is not only affecting the environment but also hurting the economy. The UK has commenced being pioneer by implementing policies in economics and society to tackle carbon emissions while reducing carbon dependence and emissions. However, it is among the largest consumers of natural gas globally and remains dependent on fossil fuel to meet their demands. A PESTLE analysis will examine the important external elements that influence an organisation (Political, Economic, Sociological, Technological, Environment and legal). It can be applied to a variety of settings and can assist people professionals and senior managers in making strategic decisions [4]. This analysis will identify the present state of the UK's respective PESTLE factors, and interrogate these factors based upon published academic literature and current industry practice and emergent developments.

Method

This study explores the PESTLE (Political, Economic, Social, Technological, Environmental & Legal) model analysis for moving from fossil energy to renewable energy in the UK. In this regard, following PESTLE factors has been considered for further analysis.

Political and Legal: The UK government has stated that it will pass laws to attain net zero emissions by 2050. This makes the United Kingdom the first major economy to make such a pledge, and it follows the recommendations of the Committee on Climate Change's recently released 'Net Zero' study [1,] which stated that eradicating emissions by 2050 is technologically achievable. However, it must be considered that the political view has a dramatic effect on the future of renewable energy by presenting many opportunities next to many risks to the existing and future renewable energy developments. One of the significant risks that can identify is the competing interests of governmental parties on an ever-increasingly tight budget which can affect the process of developing the renewable energy roadmap [3].

Economy: The future of the UK's green economy still appears uncertain, caused by additional risks to the future of renewable energy developments. For instance, for the technology to become part of the UK green energy market, the cost of production must come down. Economists believe that if the public sector investment has pledged first into renewable energy technology, they can encourage private investors to invest in the sustainable energy development process [3]. However, because renewable energy production is still in its infancy, it poses a considerable risk to investors and insurers, as seen by the "small number" of insurers now active in the field. Financial institutions have been limited in the amount of financing they can provide as a result of the global economic crisis, according to Vivid Economics, and "lending is becoming increasingly selective and examining

investment ideas much more thoroughly" [3]. In this regard, the UK government announced the Green Finance Strategy on July 2, 2019, in order to support the UK's economic policy of robust, sustainable, and balanced growth, as well as the delivery of our contemporary Industrial Strategy and our domestic and international obligations on climate change, the environment, and sustainable development.

Social: The consumers' negative attitudes to renewable energy are significant barriers to developing the hydrogen economy as green energy in the UK. The public view has concentrated on the impacts of renewable energy on their everyday lives [2]. In this aspect, using green energy, consumer adaptation, and non-convinced of safety of using sustainable energy such as Hydrogen is very low, which can directly affect the green energy market. According to the study made by Starostka-Patyk et al., enhancing the transparency of social and environmental factors can increase social responsibility by utilising renewable energy. Meanwhile, residents' awareness can be raised by education and cognitive initiatives, which can help to remove the aforesaid hurdles [5].

Technology: Technological risks of sustainable energy can mitigate by using cooperating design steps, knowledge from other industries' development plans, and monitoring. The present risks include installation, commissioning, network connection, maintenance, removal, and recycling.

Environmental: To reduce greenhouse gas emissions, air pollution, and acid rain damage, the UK government has committed to meeting EU climate change targets, as well as providing and transferring FOCIL Fuel using renewable energy. The Department for Environment, Food and Rural Affairs (DEFRA) which oversees environmental policy and regulations, particularly those relating to renewable energy and its contribution to economic growth. DEFRA is aided in its work by a variety of governmental bodies, many of which are interested in sustainable energy Fuel and Technology, allowing them to tap into a wider spectrum of knowledge [6].

Result and conclusion

The findings show that changes to legislation and government policies, such as establishing a market for low-carbon gases, consumer adaptability and motivation programmes, carbon taxes, energy security and supply, and renewable energy generation, are all economically viable. However, the outcomes of this study show that there are various stakeholders who are involved in multiple areas of the PESTLE analysis and could influence the market's development on their own. With involvement in finance, regulation, the environment, legislation, and a social commitment to the public, the UK government is possibly the most important of these stakeholders. At the very least, the near-term future will be positive if they continue to invest in the renewable energy sector. The ideal strategy for developers to manage risk, according to this literature review, is to analyse each development stage separately, considering all risks and stakeholders present at that time. The developers should move on to the next level after all hazards at that stage have been addressed to a sufficient degree.

References

[1] GOV.UK. 2022. UK government launches plan for a world-leading hydrogen economy. [online] Available at: <https://www.gov.uk/government/news/uk-government-launches-plan-for-a-world-leading-hydrogen-economy> [Accessed 15 January 2022].

[2] Ingaldi, M. and Klimecka-Tatar, D., 2020. People's Attitude to Energy from Hydrogen—From the Point of View of Modern Energy Technologies and Social Responsibility. Energies, 13(24), p.6495.

[3] Kolios, A. and Read, G., 2013. A Political, Economic, Social, Technology, Legal and Environmental (PESTLE) Approach for Risk Identification of the Tidal Industry in the United Kingdom. Energies, 6(10), pp.5023-5045.

[4] Oxford College of Marketing. 2022. Oxford College of Marketing. [online] Available at: <https://www.oxfordcollegeofmarketing.com/> [Accessed 26 March 2022].

[5] Starostka-Patyk, M.; Tomski, P.; Zawada, M. Diversity Management as a Part of Corporate Social Responsibility Policy. Procedia Comput. Sci. 2015, 65, 1038–1045.

[6] www.gov.uk/government/publications/accelerating-green-finance-green-finance-taskforce-report [Accessed 15 April 2022].

Reinforcement of Soil Support Cells Using Super Laminate Technique

Atena Susanabadi Farahani[1], Hossein Saidpour[2], Mahmoud Chizari[3]

[1] Department of Chemical Engineering, Islamic Azad Shiraz University, Shiraz Branch, IR

[2] Research department, Materials Technology Centre Ltd, Hertford, SG13 8NL, UK

[3] Department of Engineering, SPECS, University of Hertfordshire, Hatfield AL10 9AB, UK

Atena.soosanabadi@gmail.com

Abstract: **Designing a tree root protection or sidewalk support cell with sufficient strength is a challenging problem. Super Laminate Fiber Reinforced Plastic (SLFRP), with a customized pattern of fabrics and layer can improve the structure loading ability. The current study is intended to develop a new type of sustainable and cost-effective soil cells support system using a super laminate method. Therefore, a Finite Element Model was created, and a typical soil cell structure was reinforced using Carbon Super Laminate (CSL). Furthermore, a parametric optimization approach was used to improve the design parameter. The result of the current study shows that the CSL Fiber Reinforced Plastic process is an effective method to improve the strength of urban tree root protection system.**

Keywords: Tree root protection, Soil support cell, Carbon super laminate, Numerical simulation

Introduction

Tree roots are opportunistic, seeking out favorable growing conditions in urban green spaces whereas tree root systems can damage sidewalk, street and parking lot [1]. While having maximum empty space for root growth, they must have sufficient strength [2]. Market research indicates there is growing demand for planting mature trees in urban areas worldwide. This research is intended to develop a new type of sustainable and cost-effective soil support system by reinforcement of columns with Carbon Super Laminate (CSL). 'Super laminates' are a new generation of Fiber reinforced polymer (FRP) products. Sheets of carbon fabric up to 60 inches (1.5m) wide are saturated with resin and passed through a press that applies uniform heat and pressure to produce the laminate [3]. The FRP composites have attracted significant attention in repairing existing and deteriorating structures since the traditional rehabilitation techniques have several limitations in terms of durability, self-weight and complex installation process [4-5]. The aim of this research is to review and compare the Soil Support Cells (SSC) in two simple models and reinforced with CSL, under pressure test load.

Material Properties:

The SCC main material is polypropylene. The mechanical properties of this material are listed in the table 1. The super laminate that will be used to reinforce the column is QuakeWrap® B20C. QuakeWrap® B20C is a high-strength biaxial carbon fabric with equal strength in 0° and 90° directions. The fabric is black and is impregnated in the field using epoxy QuakeBond™ 300SR Saturating Resin to form a carbon fiber reinforced polymer (CFRP) used to strengthen structural elements. The fabric weighs 20oz/yd2 (678 g/m2). The mechanical properties of this super laminate are listed in the table 2.

Table 4: Polypropylene mechanical properties [6]

Properties (Unit)	Yang Modulus (MPa)	Poisson ratio	Yield Strength (MPa)
Value	1461	0.4087	34.6

Table 2: Super Laminate mechanical properties [7]

$G_{z\theta}$ (MPa)	$G_{r\theta} = G_{rz}$ (MPa)	$\nu_{\theta z}$	$\nu_{r\theta} = \nu_{rz}$	E_{zz} (MPa)	$E_{\theta\theta}$ (MPa)	E_{rr} (MPa)
18000	13320	0.04	0.25	53500	63600	8500

FEM Modeling

The Soil Support Cells (SSC) Model is shown in (Fig. 1.a). This model has four columns that are designed to withstand axial load. The desired load for each column is 100 KN, which according to the surface area of the sheet, a pressure of 1.112 MPa is applied to the sheet surface. The fix support boundary condition is also applied on the surface of the sheet on the other side of the column. Also, the symmetry boundary condition is used to apply the symmetry boundary conditions, which are located in the X and Y directions on both sides.

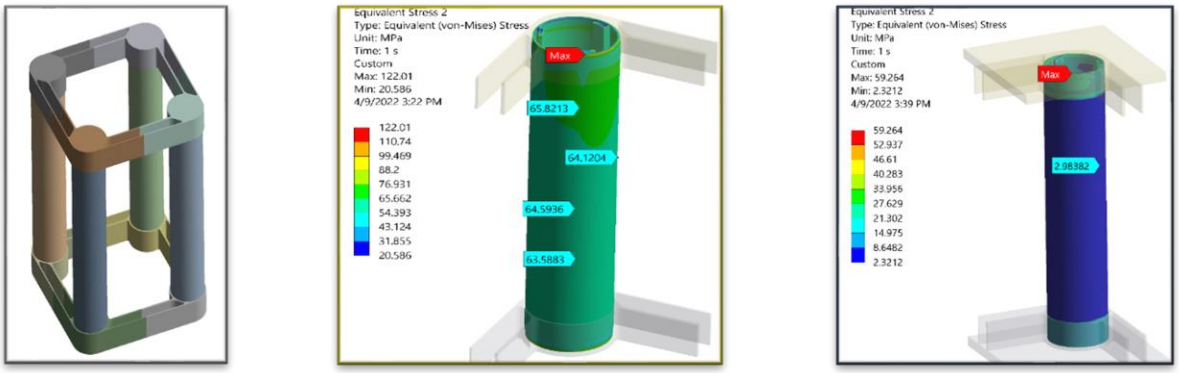

Figure1. Soil Support Cells (SSC) Model(a), Von Mises stress distribution in The SSC model without reinforcement(b), Von Mises Stress distribution in the reinforced SSC model with CSL(c)

The (figure 1.b) illustrates the Von Mises stresses of the SSC model under pressure. As can be seen, the maximum stress at the edge of the column is about 122 MPa. The stress level in the middle of the column is about 64 MPa. To reinforce the column of SSC model, a Carbon super-laminate with a thickness of 1.92 mm has been used. The (figure1.c) shows the Von Mises stresses of the SSC model with reinforcement; therefore, the maximum stress at the upper edge of the column (location of stress concentration) has reached about 59 MPa and demonstrates a 50% reduction in stress compared to the previous model. Von Mises stress values in the middle of the column have also been reduced from about 65 MPa in the previous model to about 3 MPa.

Conclusions

Results of the analyses of Von Mises stress in the Soil Support Cells modeling for two cases of polypropylene cell and the cell reinforcing with Carbon super laminate are presented in this paper. The use of super laminate to reinforce the column of the SSC model results in a 50% reduction in von Mises stress (at the stress concentration point of the column edge stress) and a reduction from 64 MPa to about 3 MPa in the middle column area. As observed in the results, the value of stress in the model without reinforcement is much higher than the strength of polypropylene. The stress values in the frame model with the reinforced columns at the stress concentration points are invalid. But with a small distance from the stress concentration points of the column edges, the stress values are drastically reduced to much less than the strength of polypropylene. This indicates that the goal of the reinforcement of the SSC model has been maintained successfully.

References

[1] F Giuliani, F Autelitano, E Degiovanni and A Montepara (2017), International Journal of Pavement Engineering Vol. **18**, No. 1 (DEM modelling analysis of tree root growth in street pavements), pp. 1–10.
[2] Leda Marritz. (2013), Five Recent UK Silva Cell Installations, https://www.deeproot.com/blog/blog-entries/5-recent-uk-silva-cell-installations.
[3] Mo. Ehsani. (2009), Elsevier Vol. **53** (6) (FRP super laminates present unparalleled solutions to old problems), pp. 40-45.
[4] E Willis (2016), Reducing Tree Root and Sidewalk Conflicts: Analysis and Strategies for the City of Palo Alto, pp. 1-57.
[5] Mary Lou Jay (2020), Composites Manufacturing, (Innovations in Infrastructure), pp. 10-14.
[6] Material library in Ansys 2021R2.
[7] https://quakewrap.com/ [Accessed 8 April].

University of Hertfordshire UH

Authors Index

University of Hertfordshire UH

Coudron, L. (2022). Proceedings of Abstracts, School of Physics, Engineering and Computer Science Research Conference 2022. University of Hertfordshire. https://doi.org/10.18745/pb.25867